Title
High Resolution High Field Quantitative Parallel Magnetic Resonance Imaging for Osteoporosis and other Clinical Applications

Author
Banerjee, Suchandrima

Publication Date
2007-09-07

Peer reviewed|Thesis/dissertation

High Resolution High Field Quantitative Parallel Magnetic Resonance Imaging for Osteoporosis and other Clinical Applications

by

Suchandrima Banerjee

DISSERTATION

Submitted in partial satisfaction of the requirements for the degree of

DOCTOR OF PHILOSOPHY

in

Bioengineering

in the

GRADUATE DIVISION

of the UNIVERSITY OF CALIFORNIA, SAN

FRANCISCO

AND

UNIVERSITY OF CALIFORNIA, BERKELEY

[redacted]

Dedicated to

My beloved parents, Soma and Siddhartha Banerjee, who taught me to have fun with whatever I do and to not take myself too seriously

My sister, Suranjana Bhowmick, my greatest ally from the day I was born

and

Sayantan, the wave and the anchor in my life (to steer clear of clichés), without whom I could not have pursued this degree

Acknowledgements

Firstly, I would like to thank my research advisor, Prof. Sharmila Majumdar for bringing me to this Bioengineering program, for being my mentor and my role model, for being so supportive of my research, career and priorities in life, for making sure that I did not lose sight of the big picture in the field of medical imaging and for inducting to her research lab, people who are so fun to work with.

I would like to thank my predecessors in this lab, Tim Dunn and Julio Carballido - Gamio for helping me settle down in the early days of my Phd. I would like to thank Roland Krug, Andrew Burghardt and Julio for being such great friends and amazing colleagues. How boring would life at the lab be without Roland's anecdotes, the occasional three course lunches at the South Beach café we went out to as a group and the animated brain storming sessions in the studygroup on Tuesdays! I would like to thank Jan, Dana, Gelaetia, Xiaojuan, Gabby, Janet, Ben, Miki, Markus, Karl, Jin, Alex, Radu and everyone else in the MQIR group for being so much fun to work with and David Newitt for lending a patient ear to my research problems and for offering helpful suggestions.

I would like to thank Esin Ozturk-Isik and Janine Lupo for being my dearest friends. Whether it was parallel imaging or Pilates, we partnered in crime.

I would like to thank Prof. Sarah Nelson for teaching me so much about parallel imaging, for chairing my qualifying committee and for improving my thesis with her comments

Dr. Thomas Link for appraising the clinical applicability of the MR methods I developed, for teaching me the basics of clinically interpreting MR images, for being on my qualifying committee and reading my thesis

Prof. Dan Vigneron for being a great faculty advisor and a supportive mentor, for teaching me basics of MR hardware and for being benign in my qualifying exam

Prof. Michael Gastpar and Prof. Avideh Zakhor for being such outstanding teachers on the subject of signal and image processing

Eric Han, for his creative research ideas that greatly benefited my projects, for being such an involved collaborator on behalf of GE Healthcare and for being a good friend

Doug Kelley, for sharing his profound knowledge on high field MRI and electrodynamics

Duan Xu for teaching me the nuts and bolts of the scanner and helping me conduct experiments on the 7 T magnet

Cornelius Von Morze for building the phased array coil that I ended up using for most of my experiments

Meridith Metcalf, Mark Albers, Azcuscena Rodriguez, Joseph Osorio for being a fun bunch of fellow Bioes

Jason Crane for helping me with the parallel computation of my software

Niles Bruce for helping me with the first MR scans

Finally, I would like to thank my parents who have always encouraged me to follow my dream, my sister for having great confidence in my abilities and Sayantan for being there for me, for pointing me to the right direction ever so often when I got stuck with a research problem and for being my model non-MR audience

I would like to acknowledge the funding support provided by UC Discovery grants LSIT01-10107 and ITL-BIO04-10148 funded in conjunction with GE Healthcare, NIH grant Vertebral Fractures: R01 AR49701, the Surbeck Foundation and the UCSF Chancellor's office for awarding me the Krevans fellowship.

Abstract

High Resolution High Field Quantitative Parallel Magnetic Resonance Imaging for Osteoporosis and other Clinical Applications

by

Suchandrima Banerjee

This thesis developed high signal-to-noise ratio (SNR) yielding magnetic resonance imaging (MRI) methods that require relatively short measurement times. The methods were primarily aimed at addressing existing technical limitations of low SNR and long scan times (~ 20 minutes) in the field of *in vivo* high resolution (HR) imaging of trabecular bone micro-architecture. HR-MRI of trabecular bone provides a non-invasive way of monitoring trabecular bone structural integrity for assessment of the disease condition, osteoporosis. Osteoporosis is a debilitating skeletal disorder affecting 1 in 3 women and 1 in 12 men over the age of 50 worldwide and is characterized by loss of bone mass and structure leading to atraumatic fractures at the vertebrae, hip, wrists and other sites. SNR limitations in trabecular bone MRI were overcome by incorporating a high magnetization yielding pulse sequence and translating the imaging protocol to the higher field strength of 3 Tesla (T) from the clinical standard of 1.5 T. A simulation model was developed to estimate SNR in bone tissue. The feasibility of imaging trabecular bone structure *in vivo* at the proximal femur (hip), until then an SNR impeded application, was demonstrated. Next, an autocalibrating parallel imaging (PI) method was implemented to accelerate data acquisition. Using an eight channel coil array, scan time was reduced 2-4 fold without any significant impact on image resolution or edge sharpness; although bone structural measures derived from the accelerated images showed overestimation. Consequently, parallel reconstruction and image processing algorithms were developed to address the causes of overestimation. With the availability

of whole body 7 T magnets and the motivation for further improvement in SNR, the PI methods were adapted to the even higher field strength and its performance was found to improve relative to 3 T. To summarize, this thesis developed SNR efficient MR methods that facilitate quantitative HR-MRI of trabecular bone within 2-10 minutes, thus increasing the clinical feasibility of this application. Additionally, the PI methods were applied to diverse applications such as cartilage imaging for osteoarthritis; and susceptibility weighted imaging of brain vasculature and 3D spectroscopic imaging of brain metabolites in brain tumor patients.

Table of Contents

List of Tables

List of Figures

Chapter 1

Introduction

1.1 Motivation

The broad goal of medical imaging is to be able to a) record images that are indicative of the internal structures/functions of the body and b) extract image features that correlate with biomarkers of diseases. Ideally, *in vivo* imaging methods should be minimally invasive, and should involve measurement times that do not cause the subjects discomfort. Of the different medical imaging modalities such as X-ray computed tomography (CT), positron emission tomography (PET) and magnetic resonance imaging (MRI), MRI is particularly attractive because it provides excellent contrast between hard and soft tissues and does not use non-ionizing radiation.

Although skeletal imaging was the earliest application of medical imaging, it remains a relevant and highly evolving field in the context of the increasing socioeconomic impact of skeletal disorders. Osteoporosis is a metabolic skeletal disease characterized by low bone mass and structural deterioration of bone tissue. It is a major public health threat for 55 percent of the people 50 years of age and older, of which eighty percent are women. Osteoporosis is responsible for more than 1.5 million fractures annually including over 300,000 hip fractures; and approximately 700,000 vertebral fractures; 250,000 wrist fractures; and 300,000 fractures at other sites. Many of these lead to morbidity and staggering health expenses (1). Although the skeleton is composed of about 80% cortical bone, trabecular bone has a eight times higher turnover

rate and is highly responsive to metabolic stimuli (2) thus making it a prime site for detecting early bone loss and monitoring response to therapeutic interventions.

The most clinically prevalent diagnostic imaging techniques used to measure bone properties and assess osteoporotic status are x-ray or ultrasound based. Image contrast in x-ray–based techniques arises from differences in tissue density. In ultrasound images, the image intensity is a depiction of the attenuation and speed alteration of sound waves. Both these methodologies reflect the density of bone mineral, and often it is difficult to distinguish the signal contribution from cortical and trabecular bone in the image. These methods are incomplete since in most cases they do not provide assessment of the three-dimensional (3D) architecture of the bone (3,4). This is a serious drawback in view of the fact that bone mass can account for only ~ 60% of the bone strength while an understanding of the spatial distribution of the mass, bone matrix composition and bone turnover is needed to account for the rest (3,5). Previously the diagnostic method for *in vivo* evaluation of bone structure involved bone biopsies. Magnetic resonance imaging provides 3D non-invasive imaging capabilities for evaluating bone structure *in vivo* and monitoring osteoporosis. Recently, cone beam scanning technology has been incorporated into dedicated peripheral quantitative computed tomography (PQCT) systems designed for *in vivo* high-resolution imaging of trabecular bone at the distal extremities (6). The absence of ionizing radiation and the innately higher contrast between bone and marrow gives MR distinct advantages over CT.

The ability to distinguish between osteoporotic and non-fracture population based on MR image derived bone parameters have been reported in literature for a large number of studies (7,8). Figure 1.1 shows MR images of the trabecular bone micro-architecture in

the distal radius in a healthy and an osteoporotic subject. The dark streaks represent the trabecular bone network and the bright regions in between represent the bone marrow. The image from the osteoporotic patient shows loss of bone structure and loss of network connectivity while that from the healthy subject depicts a dense well-connected bone network. While MRI has established itself as an extremely promising monitoring tool for osteoporosis, several difficulties in its implementation remain. Magnetic and chemical heterogeneity in the tissue composition of trabecular bone presents unique technical challenges for MRI. Additionally, the structural elements comprising the trabecular bone network have nearly microscopic dimensions (100-200 μm), so very high spatial resolution is necessary to depict the bone structure in an MR image (4).

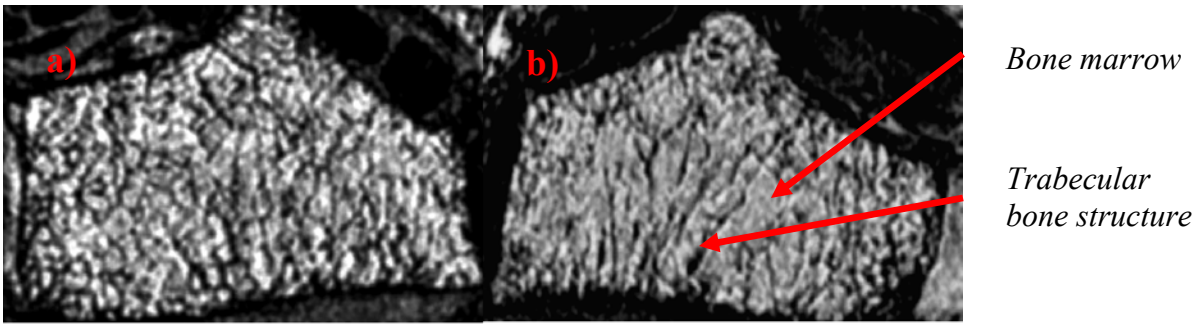

Figure 1. 1 Representative MR image of the trabecular bone structure in the distal radius of a: a healthy subject and b: an osteoporotic patient. The bone structural organization in b is much sparser and less connected compared to a. These images were Majumdar S, et al, Journal of Bone Mineral Research Vol (12), 1997

The three competing factors to be considered in high-resolution (HR) MRI are signal-to-noise ratio, spatial resolution and imaging time. Spatial resolution and signal-to-noise ratio (SNR) are both directly related to imaging time but are inversely related to each other. A minimum SNR is required to be able to analyze the images. Acquisition times longer than 15-20 minutes cause discomfort in patients and result in motion

induced artifacts. The technique developments in the domains of MR image acquisition, reconstruction and analysis to be presented in this work are based on all these considerations and are aimed at increasing SNR and accelerating measurement time while still ensuring accurate quantification of disease biomarkers from the images. Recent developments in MR magnet, gradient and RF hardware technology have also influenced our research approach. In recent years, whole body high field magnets (3 Tesla, 7 Tesla) have become available for human MRI. With improvements in gradient hardware, rapid imaging sequences with high duty cycle have become more feasible. Developments of phased array RF transmitters and receivers have ushered an era of rapid MR imaging using massively parallel excitation and signal detection strategies (9,10). These technological resources have been incorporated in our MR developments.

Besides osteoporosis, our technique was applied to another debilitating musculoskeletal disease, osteoarthritis. Osteoarthritis affects joints such as the knee and hip and is characterized by progressive loss of articular cartilage. MRI of articular cartilage is emerging as a diagnostic tool for assessing cartilage morphology, biochemistry and function (11). Our rapid MR technique was extended to quantitative imaging of cartilage morphology at the knee. Additionally it was extended to neurological applications such as spectroscopic imaging (SI) of brain metabolites and susceptibility weighted imaging (SWI) of brain vasculature for monitoring brain tumors. Each of these application areas not only have a different disease focus but also pose different technical challenges. Trabecular bone MRI requires accurate quantification of image features in the order of pixels where as cartilage MRI requires accurate quantification of image features in the macroscopic scale. Spectroscopic imaging

involves processing of four dimensional acquisition data and both SI and SWI require accurate reconstruction of image phase. By applying our MR method to these diverse application areas, we not only increased its utility but were able to test the robustness and flexibility as well.

1.2 Chapter Organization

The thesis consists of eight chapters. The organization of material in Chapters 2-8 is as follows:

Chapter 2 provides background on magnetic resonance imaging principles and the assessment of osteoporosis from MR images.

Chapter 3 presents optimization of an imaging protocol employing the SNR efficient pulse sequence, balanced steady state free precession (bSSFP) for high resolution bone imaging at 1.5 Tesla (T) and its translation to the higher field of 3 T. The SNR gained at the higher field with the bSSFP protocol was estimated from simulation and experimental studies (12).

Chapter 4 presents the development of a parallel imaging technique for accelerating HR-MRI of trabecular bone and an in-depth qualitative and quantitative evaluation of images obtained by this rapid imaging method (13).

Chapter 5 presents translation of the parallel imaging method presented in Chapter 4 to the higher field strength of 7 Tesla. Potential of parallel imaging at the high field is evaluated quantitatively and assessed in the context of electro-magnetic properties of skeletal tissues. (14)

Chapter 6 proposes regularized parallel image reconstruction and histogram based post-processing methods to improve the accuracy of measurement of trabecular bone structural parameters from images obtained by highly accelerated parallel imaging techniques (15).

Chapter 7 examines the robustness and flexibility of our parallel imaging technique by extending it to two neurological applications-spectroscopic imaging of brain metabolites and susceptibility weighted imaging of brain vasculature (16,17). This work was done in collaboration with the members of Professor Sarah Nelson's research group.

Chapter 8 summarizes the work presented in Chapters 3-7 and discusses its advantages, limitations and scope of future improvement.

Chapter 2

Background

2.1 Magnetic Resonance Imaging

Magnetic resonance imaging (MRI) originated from the nuclear magnetic resonance (NMR) method that has been used by physicists and chemists since the 1940s for studying molecular structure and diffusion. In 1973 Paul Lauterbur acquired a magnetic resonance image for the first time by employing spatial localization of the NMR signal. Magnetic resonance is based on the interaction between an atom and the external magnetic field. Atoms with odd atomic number i.e. atoms having net nuclear spin angular momentums are visible to the MR phenomenon. As the most biologically abundant nucleus with odd atomic number, hydrogen (^{1}H) has the greatest sensitivity to MR, and so naturally most MR experiments are tuned to the resonant frequency of protons. MRI is used to look at other nuclei such as carbon (C^{13}) and phosphorus (P_{31}) as well, but the scope of this dissertation is limited to proton MRI only.

2.1.1 Quantum and classical description MR

MR imaging involves interaction of atoms with three external magnetic fields:

1) the main static magnetic field (B_0) 2) radiofrequency field (B_1) 3) gradient fields G.

In the presence of the external magnetic field the nucleus can attain discrete energy levels that are related to the discreteness of the nuclear angular momentum, also known as spin angular momentum or spin.

$$\boldsymbol{\mu} = \gamma \mathbf{S} = \gamma \hbar \mathbf{I} \qquad [2.1a]$$

where μ , S, $\hbar$, I and γ are the magnetic dipole moment, spin angular momentum, Planck's constant, spin operator and gyromagnetic ratio respectively. Gyromagnetic ratio is a constant unique for each type of atom. For protons, γ=42.58 MHz/ Tesla. The potential energy E of the magnetic moment μ in presence of the magnetic field B is

$$E = -\boldsymbol{\mu}.\mathbf{B} \qquad [2.1b]$$

For proton, the two possible eigenstates of the spin are $\pm\frac{1}{2}$. So difference between the two energy states is

$$\Delta E = \gamma\hbar B0 \qquad [2.1c]$$

Ratio between spin population occupying the higher (antiparallel to B0) and lower (parallel to B0) energy states is given by the Boltzman distribution

$$\frac{n_{upper}}{n_{lower}} = e^{-\frac{\Delta E}{kT}} \qquad [2.2a]$$

where k is the Boltzman's constant and T is the absolute temperature.

In the absence of an external magnetic field, there in equal occupancy of both energy levels leading to a degenerate state. In the presence of Bo, the n_{lower} population slightly outnumbers the n_{upper} (7 out of a million) resulting in a weak polarization of the imaging sample. This is known as the Zeeman effect and it underlies the MR phenomenon. The equilibrium nuclear magnetization M_0 in the sample is given by

$$M_0 = \frac{N\gamma^2\hbar^2 I_z(I_z+1)B_0}{3kT} \qquad [2.2b]$$

where N is the total number of nuclear spins per unit volume. At equilibrium, net exchange of energy between the spin system and the outside world is zero. If the sample is then irradiated by an electromagnetic irradiation of frequency f_0 such that

$$\Delta E = hf_0 = \gamma \frac{h}{2\pi} B_0 \qquad [2.3a]$$

transitions will be induced between energy levels. This is known as the on resonance condition. The resonant frequency expressed in radians/sec can be written by the Larmor equation as

$$\omega = \gamma B_0 \qquad [2.3b]$$

where ω is known as the Larmor frequency. This equation (2.3b) lays the foundation of spatial localization for MRI by connecting resonant frequency to the magnetic field strength. After the RF is turned off, spins return to equilibrium emitting energy that is detected as the MR signal. This is in brief, the quantum mechanical description of spin interactions with B_0 and the radiofrequency field B_1.

Fortunately, most of the MR phenomenon can be explained accurately using classical physics. In the classical description, the nuclear angular moments are described by magnetization vectors and polarization is represented by a net magnetization vector aligned with B_0. At equilibrium, the nuclear moments experience precession about the B_0 axis in random fashion such that the transverse component of the magnetization (M_{xy}) cancels to zero and there is a net magnetization vector only along the z axis (M_z), aligned with B_0. On the application of a radiofrequency (RF) field B_1 perpendicular to B_0 at the resonant frequency, M_z experiences a torque resulting in a non-zero transverse component M_{xy}. The degree of rotation depends on amplitude and duration of the RF excitation. After the RF excitation is turned off, the M_{xy} component experiences free induction decay (FID) and the longitudinal component M_z eventually returns to equilibrium. By Faraday's induction law, the varying magnetic field associated with the

FID generates a voltage in MR detector coils that are tuned to the resonant frequency leading to detection of the MR signal.

The longitudinal relaxation is described by the Bloch equation

$$\frac{dM_z}{dt} = -\frac{M_z - M_o}{T_1} \qquad [2.4a]$$

where T_1 is known as the longitudinal/spin lattice time constant. Physically it involves energy exchange between the nucleus and surrounding spin lattice. From the quantum point of view, it involves energy transition between n_{upper} and n_{lower} spin populations. Since the energy gap between the two populations is proportional to B_0, it is obvious that T_1 lengthens with increase in field strength. The transverse or T_2 relaxation behavior can be described by the Bloch equation:

$$\frac{dM_{xy}}{dt} = -\frac{M_{xy}}{T_2} \qquad [2.4b]$$

For 90° excitation, the longitudinal and transverse magnetization components can be written as

$$M_z(t) = M_0(1 - e^{-t/T1}); \quad M_{xy}(t) = M_0 e^{-t/T2} \qquad [2.4c]$$

The T_2 relaxation, also known as spin-spin relaxation arises from spread of resonant frequencies and the subsequent loss of phase coherence of the transverse magnetization. It must be noted that T_1 and T_2 relaxation processes are closely related. Since the magnetization M eventually returns to equilibrium Mo, $T_2 \leq T_1$. Unlike T_1, T_2 is largely independent of field strength. T_1 and T_2 relaxation constants are characteristics of the molecular environment of a tissue. In solids, slowly varying field fluctuations create a large broadening of the resonant frequencies and very short T_2. When magnetic heterogeneity in the tissue environment imposes additional spatial magnetic gradients,

there is more broadening of resonant frequencies and more rapid loss of phase coherence. This is known as T_2* decay. However, unlike T_2 decay, T_2* decay is reversible for some imaging sequences as will be described in Section 2.1.3 (18,19).

2.1.2 Spatial localization of MR signal

To acquire an MR image it is essential to spatially localize the source of NMR signal. Since the Larmor frequency is proportional to the magnetic field experienced by a spin, the underlying principle of spatial localization in MR is to employ spatially varying magnetic fields known as gradients so that the Larmor frequency of a spin encodes its spatial position. Gradients consist of three orthogonal magnetic fields G_z, G_x and G_y which are commonly known as the slice selection, frequency encoding (FE) and phase encoding (PE) gradients respectively based on their functionalities. Gz gradient imposes a variation in frequency with z so that only a particular z (slice) location is on resonance with the RF excitation. The slice thickness can be controlled by the G_z amplitude. The remaining two dimensions are spatially encoded with the help of the frequency encode and phase encoding gradients. In one dimension the spatial locations of spins can be encoded by their frequencies. Encoding in the other dimension is achieved by applying phase offsets proportional to the spatial position of the spins. Mathematically, the spatial encoding by gradients is equivalent to a Fourier Transformation of the spatial distribution of magnetizations in a selected volume in the subject being imaged. The Fourier space is known as k-space in the MR formalism. Since only discrete positions in k-space are encoded by the gradients, the Fourier space is discretely sampled in this process. The image is recovered from the measured MR signal by an inverse Fourier transformation. In more sophisticated imaging techniques such as spiral and echoplanar imaging, the

gradient waveforms vary in space as well as time and the k-space can be sampled in any arbitrary trajectory (20,21).

MR signal detected at time t can be written as

$$S(t) = i\omega_0 B_1(\mathbf{r}) \int_{vol} m(\mathbf{r}) e^{-i\omega_0 t} \exp(-i\gamma \int_0^t \mathbf{G}(\tau).\mathbf{r} d\mathbf{r} \quad [2.5a]$$

$$= i\omega_0 B_1(\mathbf{r}) e^{-i\omega_0 t} \left[\int_{vol} m(\mathbf{r}) \exp(-2\pi i \mathbf{k}.\mathbf{r}) d\mathbf{r} \right]; \quad k = \frac{\gamma}{2\pi} \int \mathbf{G}(\tau) d\tau$$

$$\propto M(\mathbf{k}) \quad [2.5b]$$

where m(**r**) is the magnetization at spatial position (**r**), M(**k**) is the Fourier Transform of the spatial distribution of magnetization at spatial frequency (**k**) and **G** is the superposition of all gradient fields at position **r.** B_1**(r)** is the magnetic field produced at the position **r** per unit current in the coil and by the principle of reciprocity it is also indicative of the receiver coil sensitivity at that position. It can be seen from Eq. [2.5b] that measurement of MR signal at any time instant t also corresponds to measurement of the spatial frequency component of the magnetization distribution at a frequency **k**. This spatial frequency is equal to the time integral of the gradient at the instant of measurement (18).

2.1.3 Gradient echo and spin echo imaging

Imaging sequences can be classified based on type and timing of RF excitation and gradient waveforms. Spin-echo and gradient echo, the two main classes of MR sequences will be described in this section.

A basic gradient echo sequence consists of 90° excitation applied in conjunction with a slice selection gradient. Following the 90° RF excitation, a phase encoding gradient and a negative FE gradient that dephases transverse magnetic component, are

applied. The direction of the FE gradient is then reversed so that the spins precess in opposite direction and regain phase coherence lost due to the dephasing effect of the negative FE gradient-this is also known as echo formation. The measurement window is so positioned that signal from the center of k-space is measured at the center of the echo. In gradient echo sequences the coherence loss due to T2* decay is not recovered during the echo. The signal equation for GE imaging is given by

$$S = k\rho \frac{(1 - e^{-\frac{TR}{T_1}})e^{-\frac{TE}{T_2^*}} Sin\alpha}{1 - Cos\alpha e^{-\frac{TR}{T_1}}} \qquad [2.6]$$

where ρ and α are the proton density and flip angle respectively, and k is a proportionality constant that accounts for gains in the instrumentation system. The timing diagram of the basic gradient echo sequence is shown in Figure 2.1. The interval between the two RF exciations is denoted by repetition time (TR) and the time interval between the RF excitation and echo formation is denoted by echo time (TE) (18).

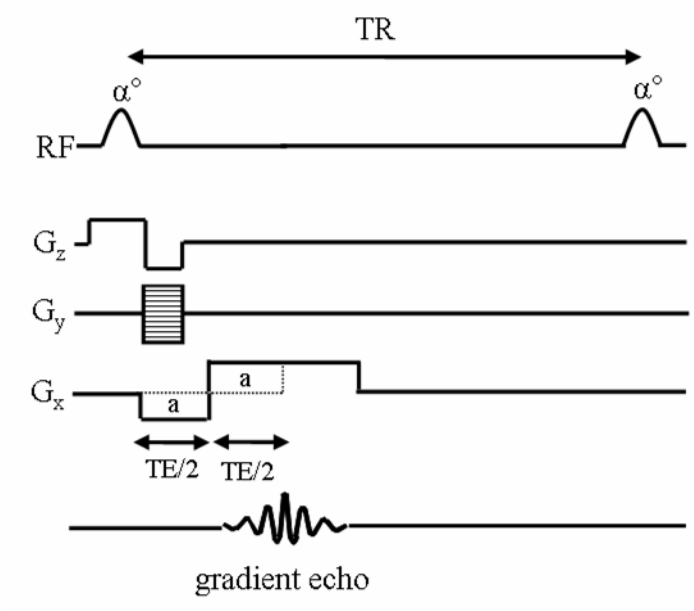

Figure 2.1 shows the timing diagram of a basic gradient echo sequence

A basic spin echo (SE) sequence consists of a 90° excitation, applied in conjunction with a slice selection gradient and a slice selective 180° pulse applied after a time TE/2. After the 90° RF pulse is turned off, spins precessing in the transverse magnetic plane about the B0 axis gradually lose coherence due to broadening of the resonant frequency. The 180° RF pulse is applied about the transverse axis at a time TE/2 after the 90° excitation to refocus the spins in the transverse plane. A period of TE/2 after the 180° excitation, the spins rephase producing a strong "spin-echo". The MR data is acquired at this time. Figure 2.2 shows the timing diagram for a spin echo sequence. The echo time (TE), which is the time of the echo formation, and the repetition time (TR), which is the time between two consecutive 90° pulses, are also shown in Fig. 2.2. The signal equation for SE imaging is given by (18)

$$S = k\rho\left(1 - e^{-\frac{TR}{T_1}}\right)e^{-\frac{TE}{T_2}} \qquad [2.7]$$

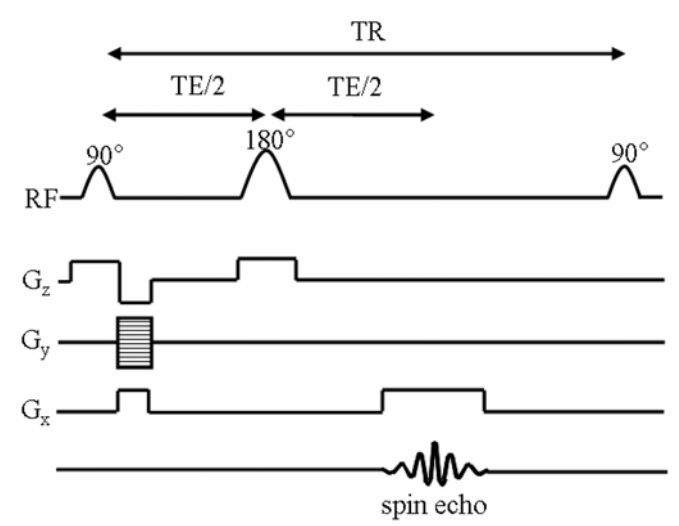

Figure 2.2 shows the timing diagram of basic spin-echo sequence

2.1.4 MR Image contrast

Since relaxation constants such as T_1, T_2 and T_2^* are tissue characteristics, they provide image contrast between different tissue types and are also considered to be biomarkers in many disease conditions. Depending on the imaging application, imaging parameters such as TR, TE and flip can be adjusted to accentuate a desired contrast or weighting in the MR image. From Eq. [2.7], long TR and short TE in a spin-echo sequence will reduce T_1 and T_2 weighting respectively, yielding a primarily proton density weighted image. Short TE and short TR will yield a T_1 weighted image while long TE will accentuate the T_2 contrast. For gradient echo imaging, the contrasts can be further manipulated by choice of flip angle. From Eq. [2.6], it can be seen that a low flip angle diminishes the T1 weighting. As the flip angle increases it results in a significant T1 contribution in the signal. The T1 weighting can be further adjusted by varying the TR. Employment of a long TE emphasizes the T_2^* contrast (18).

2.1.5 SNR in an MR image

Signal in a voxel in the MR image can be written as (22):

$$S \propto \omega_0 B_0 . B_1(x,y,z).M(x,y,z)N_{samples}\Delta x\Delta y\Delta z$$

[2.8a]

where Δx, Δy and Δz are the voxel dimensions, $N_{samples}$ are the total k-space samples acquired and M(x,y,z) is the magnetization at (x,y,z).

The noise power can be written as:

$$N(f) = 4kTR_{eff}\Delta f N_{samples} \qquad [2.8b]$$

where k, T, R and Δf are the Boltzmann's constant, absolute temperature, effective coil resistance and receiver bandwidth respectively. In most cases the effective resistance is

dominated by resistance of the imaging sample. The resistance which a coil sees from a sample is proportional to the volume of the sample from which the coil receives signal, $V_{sensitive}$. So R_{eff} is proportional to $V_{sensitive.}$ Due to the differentiation related to Faraday's induction law, the noise power is also weighted by the Larmor frequency.

So, the SNR in a voxel in an MR image can be written as:

$$SNR \propto \frac{B_0 B_1 M(x,y,z)\Delta x \Delta y \Delta z \sqrt{N_{samples}}}{\sqrt{\Delta f V_{sensitive}}} \qquad [2.8c]$$

From equation [2.8c] it can be inferred that the SNR in an MR image can be increased by increasing the field strength B_0, the voxel dimensions, the number of k-space samples and by employing pulse sequences that will increase the magnetization. From equation [2.8c], it is also obvious that employing coils which have a smaller volume of sensitivity, such as surface coils, reduces effective coil resistance and consequently improves the SNR.

2.2 Assessment of trabecular micro-architecture from MR images for monitoring osteoporosis

Osteoporosis is a metabolic skeletal disorder characterized by a loss of bone mineral density and characterized by the occurrence of atraumatic vertebral fractures, fall-related hip fractures, and Colles fractures of the distal radius. It is now widely accepted that "bone quality" depends on several factors pertaining to cortical and trabecular bone such as shape and geometry of the bones in the macro-architectural level, cortical shell thickness and spacing, connectedness of the 3D trabecular bone network at the micro-

architectural level, composition of the bone-matrix, mineralization among other things (3,4). This has motivated the development of MR imaging techniques for assessment of 3D trabecular network. It permits not only the depiction but also the quantification of trabecular bone structure, and hence its biomechanical properties.

The trabecular bone network comprises of a network of interconnected plates and struts encased by a thick cortex. Trabecular structural elements in the human skeleton are typically 100-150 μm thick. Interstitial spaces in the trabecular network are occupied by bone marrow which mainly consists of fat and water. Since bone has low water content that is mostly bound to collagen, it has a very short T2 relaxation time. So in an MR image, trabecular bone appears dark in stark contrast to the bright marrow. MR can be used to assess the properties of trabecular bone in two different ways. The first is an indirect measure, often termed relaxometry or quantitative magnetic resonance (QMR). Trabecular bone, being composed of heavy elements such as Calcium and Phosphorus is substantially more diamagnetic than bone marrow. As a result local field inhomogeneities arise, and the T2 and T2* relaxation properties of bone-marrow are impacted. The local field gradients depend on the field strength as well as on number of bone-bone marrow interfaces, size and orientation of the trabecular structures etc (23). So the basic principle of the QMR technique is to indirectly assess the density and structure of trabecular bone network from the altered relaxation properties of the bone marrow.

The second and direct method of MR assessment involves direct visualization of the dark, trabecular bone, in contrast to the bright marrow fat from high resolution (HR) MR images. A representative HR image of the trabecular bone micro-architecture at the ankle (calcanues) is shown in Figure 2.3. The best spatial resolution that can be achieved

in vivo even with the most advanced MR techniques is in the order of the average trabecular thickness of 100-200 μm. This gives rise to partial volume effects in the image. As a result, the imaging method might be less sensitive to detection of very thin trabeculae or may represent an average or a projection of a few trabeculae (3). However, since the inter-trabecular spacing is typically much larger than that and is increased in osteoporosis, it is still possible to derive some structural measures from MR images reproducibly. Recognizing the limited spatial resolution regime, a major focus in the field of MR derived bone structural analysis has been to investigate the resolution dependence of MR-based measures and to calibrate MR-derived measures against a gold standard (24,25)

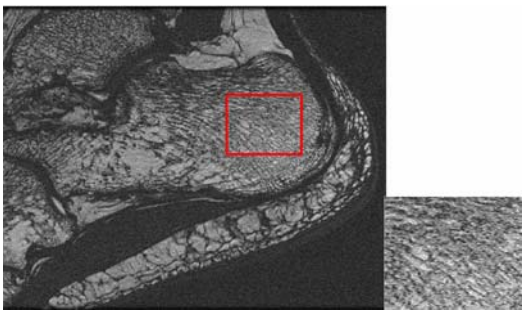

Figure 2.3 shows a typical HR-MRI image of trabecular bone structure at the ankle. The bright streaks represent the bone marrow while the intermediate dark streaks depict trabecular bone.

MR image analysis techniques probing several properties of the trabecular structural organization such as inter-element spacing, anisotropy, connectivity, texture and lacunarity have been developed over the last two decades to identify all aspects of structural deterioration in trabecular bone associated with osteoporosis. Many of the measures such as trabecular bone volume fraction (BV/TV), trabecular thickness (Tb.Th), trabecular spacing (Tb.Sp), and trabecular number (Tb.N) are inspired by thin-section

microscopy-based bone histomorphometry techniques (26,27). Others include topological measures such as Euler's number and surface-to-curve ratio, fractal dimension, cocurrence, maximum entropy measure etc (28,29). Image intensity variations caused by inhomogeneities in receiver sensitivity usually need to be removed before extraction of the structural measurements (30). Most structural parameters are derived from a processed image that has been binarized into bone and non-bone phases, which is typically done by thresholding. The choice of threshold is complicated by partial voluming because in an MR image, voxels typically are partly occupied by bone and partly by bone marrow. Majumdar et al proposed a dual-threshold technique in which the bone reference intensity I_B is chosen by sampling regions of the cortical shell from the image, and the marrow intensity I_M is empirically chosen as the upper value at which the histogram has half of the maximum peak height (31).

The fractional bone area $f = \frac{N_B}{N}$ where N_B is the number of trabecular bone pixels and N is the total number of pixels in the region of interest (ROI) can be determined based on the two reference intensity levels.

$$f = \frac{I_M - I_{avg}}{I_M - I_B}$$

where I_{avg} is the average intensity in the ROI. After determination of the bone fraction f, the threshold for binarizing the image into bone and marrow can be chosen such that the resulting bone fraction matches f. Structural measures analogous to histomorphometry are generally analyzed by a two-dimensional plate like model using the Mean Intercept Length (MIL) method (32). In the MIL method, a set of parallel rays is passed through the ROI over different angles. The number of mean intercepts over all the angles gives a

measure of the trabecular number whereas the mean intercept length gives a measure of the inter-trabecular spacing. Since the MR images are not acquired at true microscopic resolutions, Majumdar et al described these measures derived from MR images as "apparent" measurements. However, the authors also noted that the apparent structure reflected by the limited-resolution MR images is highly correlated to the "true" structure (33). To obviate the need for binarization of the MR image, methods such as Distance Transform, fuzzy transform, spatial autocorrelation analyses, texture and wavelet based structural analysis have also been proposed in the literature (29,34-36). Among the MR-derived bone structural measures analogous to histomorphometry, apparent trabecular number (App. TbN) and apparent trabecular spacing (App. TbSp) which is a reciprocal of App. TbN, have been found to distinguish between non-fracture and osteoporotic population (37,38).

Chapter 3

Application of high magnetization yielding pulse sequence and higher magnetic field strength (3 Tesla) to improve SNR of *in vivo* trabecular bone MRI-simulations and experiments

3.1 Introduction

In vivo MRI has evolved over the past two decades as a promising diagnostic tool for monitoring the structural organization of bone in response to therapy or with disease progression in osteoporosis patients. Since a minimum spatial resolution of 150-200 μm is necessary to depict the trabecular architecture and scan time should be no longer than 15-20 minutes to avoid patient discomfort, this imaging application demand high SNR efficiency. Imaging of trabecular bone at non-peripheral anatomic sites is even more SNR limited as the sensitivity of surface coils diminishes approximately proportional to cube of the depth from the surface (22). So while micro-structural parameters of trabecular bone at extremal sites such as the calcaneus (heel bone), distal radius (wrist bone), and distal tibia have been quantified from MR images (39) and analyzed for correlation with hip fracture risk (40) extensively over the last decade, *in vivo* MRI of trabecular bone at non-peripheral sites such as the vertebrae and the proximal femur (hip) had not been conducted. In this work we investigated the use of a SNR efficient pulse sequence and

higher static magnetic field strength to facilitate SNR deficient imaging applications such as trabecular bone MRI of the proximal femur.

3.2 Background

3.2.1 Magnetic Susceptibility

Spins in an imaging subject/ object experience internal magnetic fields in addition to the external magnetic fields in the MR magnet. The internal field is dominated by neighboring atomic electrons whose individual contributions can be well approximated by magnetic dipole fields. All materials have induced dipole moments in the presence of time-dependent external magnetic fields. The induced atomic currents produce a weak magnetic field opposing the external magnetic field. This omnipresent phenomenon is known as diamagnetism. Atoms with unpaired electrons have a non-zero magnetic moment with an associated non-zero dipole magnetic field that aligns with the external field and reinforces it. These are known as paramagnetic materials. In cases where the electrons pair up to cancel their spin magnetic moments, diamagnetism is more predominant than paramgnetism. Materials such as iron, gadolinium have permanent domains of electron spin magnetic moments that produce strong self-magnetic fields irrespective of external fields. Most biological tissues are diamagnetic. Local susceptibility gradients arise when neighboring atoms in an imaging volume have different magnetic susceptibilities. Since the precession frequency of a spin is proportional to the magnetic field strength, differences in local magnetic fields experienced by spins lead to off-resonance, causing dephasing of the MR signal, and T2* relaxation for gradient echo sequences (41).

3.2.2 MR pulse sequences for imaging trabecular bone micro-architecture

The tissue composition of trabecular bone provides unique technical challenges to MR imaging of its micro-architecture. Firstly, bone is generally invisible in MR due to its ultra-short T2 relaxation time. In contrast, bone marrow has high signal intensity, so the trabecular network is depicted indirectly in an MR image by depiction of the marrow (4). Trabecular bone consists of a network of interconnected plates and columns with bone marrow dispersed in the interstitial spaces between the structures (42). Bone being composed of elements with high atomic number (Calcium and Phosphorus) is more diamagnetic than bone marrow which mainly consists of water and fat. This gives rise to magnetic field inhomogeneity in bone-bone marrow interfaces. Consequently, dephasing and signal cancellation occurs in voxels at the bone-marrow interfaces (23,42). In spin-echo sequences the signal decay due to static dephasing over and above T2 decay, also known as T2* decay, is recovered at the time of the echo, whereas in gradient echo sequences it is not. As a result the T2* effect is manifested by variations in image intensity in the bone marrow and a broadening/ blooming of trabecular structures in an MR image acquired by GE sequence. Additional signal modulation is also caused by different chemical components of the fatty marrow (31). So ideally, 3D spin echo (SE) sequences are better suited for imaging of trabecular bone micro-architecture by virtue of robustness to static dephasing and off-resonance effects. However, GE sequences can be employed with short repetition time (TR) because of their higher SNR efficiency and can thus acquire a 3D volume in shorter scan time and avoid patient motion artifacts. As a result, 3D GE sequences such as 3D Fast Gradient Recalled Echo (FGRE) sequences are widely employed for HR-MRI of trabecular bone (30,31,33). Generally, scan time in SE imaging can be reduced by employing multiple RF spin echoes to sample multiple phase-

encoding lines in one repetition time. But the long echo train length causes T2 blurring broadens the point spread function (PSF), and consequently decreases effective image resolution (43). This type of sequence is not suitable for HR-MRI of small structures. Although a three-dimensional (3D) SE pulse sequence employing only one echo per excitation would be optimal long imaging time and low SNR efficiency limit its clinical use. To address these problems 3D-SE type pulse sequences with variable flip angle like rapid SE excitation (RASEE) (44), large-angle spin-echo imaging (45) and subsequently fast 3D large-angle spin-echo imaging (FLASE) were introduced The general idea of all these approaches was to apply composite RF pulses (RASEE) or only one large-angle RF pulse (FLASE) (46) so that the longitudinal magnetization is partly tipped to the negative axis. The subsequent 180° phase reversal pulse, while generating an echo, restores the longitudinal magnetization. Even with this scheme, the TR has to be sufficiently long, on the order of 80 ms (46), to avoid saturation.

3.2.3 Steady State Free Precession (SSFP) Sequence

In recent years, with advances in gradient hardware, fully refocused steady state free-precession (SSFP) sequences such as three dimensional fast imaging employing steady state acquisition (FIESTA), true fast imaging with steady state free precession (trueFISP) and balanced fast field echo (bFFE), which employ very short repetition times (TR << T2) have become popular because of their high SNR (47). The timing diagram of fully refocused SSFP sequence is shown in Figure 3.1. Though these sequences are rapid gradient-echo techniques, their spin-echo-like refocusing behavior for a limited range of off-resonant frequencies has been shown in the literature (48). However, refocused SSFP imaging is limited by its sensitivity to field inhomogeneity. The attenuated response from

regions of off-resonance may cause dark bands ("banding artifact") to appear in an SSFP image with a periodicity inversely proportional to the repetition time (47) . To overcome this limitation, especially in applications that employ long TRs or image heterogeneous tissues, multiple-acquisition SSFP techniques such as the phase-cycled FIESTA (FIESTA-c), which acquire data from *n* independent SSFP acquisitions (49,50), evolved. Each of these acquisitions employs a different phase increment between excitation radiofrequency (RF) pulses, so that the signal notches in each of their response profiles are shifted in position with respect to the others. Combining these datasets yields a flatter response profile. Generally, the final image is computed by assigning to each pixel the maximum magnitude of the *n* corresponding reconstructed pixel values (also known as the maximum intensity [MI] technique).Other combination techniques, such as sum-of squares, complex sum, etc. have also been discussed and evaluated (49). The larger the value of *n*, the better the removal of banding artifacts, but the scan time for an *n*-acquisition SSFP is *n* times longer compared to single-acquisition SSFP and thus, the SNR efficiency is poorer.

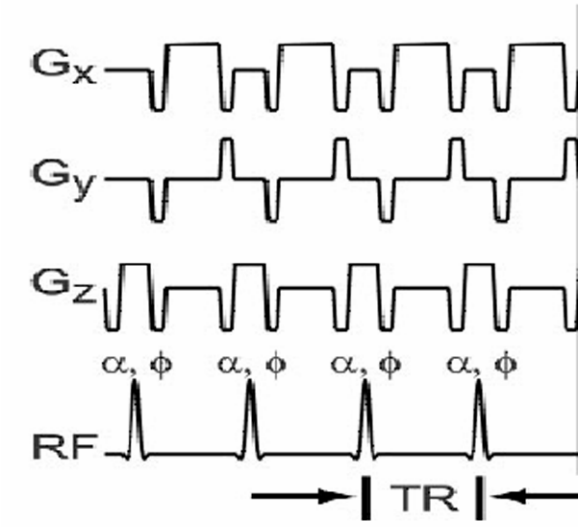

Figure 3.1 shows the timing diagram of b-SSFP sequence

3.3 Methods

3.3.1 Simulation Studies

Magnetization Response and Optimization

We developed a simulation (Matlab 6.1; MathWorks Inc., USA) of the steady-state transverse magnetization response to fully-refocused SSFP by linear system analysis similar to that described by Hargreaves et al (51). From the analysis, Mss, the steady state magnetization vector, is a function of T1, T2, TR, TE, and flip (α) and precession (β) angles.

$$Mss = f(T1, T2, TR, TE, \alpha, \beta) \qquad [3.1]$$

The shape of the steady-state transverse magnetization response (Mxy) is primarily influenced by T1, T2 and α while bandwidth of the "passband" is determined by TR (47,52). T1 and T2 values used as inputs to the simulation correspond to that of marrow

fat: T1 =288 msec and T2 = 165 msec at 1.5 T and T1 = 371 msec and T2 = 133 msec at 3 T (53). In refocused SSFP sequences such as FIESTA and trueFISP, the phase of the RF pulse is incremented by 180° from one excitation to another (47,54). So a spin on resonance effectively undergoes an angle of precession of 180° over one TR. For simulation of the composite response to the FIESTA-c sequence, we computed two sets of steady state values; one for an SSFP acquisition with no phase increment between excitations and one for a standard SSFP acquisition with phase increments of 180° from one excitation to another. Number of acquisitions (N) was limited to two, keeping in mind practical issues with long scan times.

$$\mathrm{Mxy}_i = \mathrm{f}(\mathrm{T1}, \mathrm{T2}, \mathrm{TR}, \mathrm{TE}, \alpha, \beta, \phi_i) \qquad [3.2a]$$

$$\phi \in \{0, \pi\}, \mathrm{i} \in \{1,2\} \qquad [3.2b]$$

The resultant response to the FIESTA-c sequence was computed as the maximum magnitude across the datasets. In MR images, trabecular bone structures appear as dark streaks in a bright region that represents the bone marrow so, essentially, SNR is synonymous with contrast-to-noise ratio (CNR). Hence, the imaging parameters were optimized with a focus on SNR, SNR efficiency, and sensitivity to off-resonance.

Intravoxel Inhomogeneity

To estimate the intravoxel inhomogeneity arising from the susceptibility difference between bone and marrow, we simulated a simplified bone-model consisting of a uniform random distribution of spherical inclusions (to mimic trabecular microstructures) in a medium of fatty marrow. The input parameters for this model were the main magnetic field strength (B_0), pixel dimensions, fractional area occupied by bone (area belonging to

bone/total area), diameter and orientation of a trabeculae, and minimum intertrabecular spacing. Assuming a susceptibility difference of 0.3 parts per million (ppm) between the bone and the marrow (55) we generated a map of the static inhomogeneity within the pixel using standard magnetostatics (41,42). Inhomogeneity at a point (xo, yo) was calculated as the summation of the contributions from each of the inclusions at (xi, yi):

$$\Delta B = \sum_i \frac{4\pi}{3} \frac{\Delta\chi B_0 R^3 (3\mathrm{Cos}^2\theta_i - 1)}{r_i^3} \qquad [3.3a]$$

$$\Delta\chi = \mu_0 - \mu_i \qquad [3.3b]$$

where R is the radius and μ_i is the susceptibility of the microspherical inclusion. r_i and θ_i are the magnitude and orientation with respect to the main magnetic axis of the position vector of the i^{th} inclusion and μ_0 is the susceptibility of the medium. The magnetic susceptibilities are in the cgs system of units.

Consequently, the off-resonance $\Delta\omega(xo, yo)$ is given as:

$$\Delta\omega = \gamma\Delta B \qquad [3.4]$$

where γ, the gyromagnetic ratio, is 2.675×10^8 rad/second/T

Signal Estimation

We binned the off resonances within a voxel into a histogram. For a particular set of imaging parameters (TR, TE, and flip angle) and static field strength (B_0), $M(\beta)$, the magnetization response to the FIESTA sequence for each binned frequency β, was computed using the sequence simulation described above. As shown in Eqs. [3.2a] and [3.2b], for estimating the signal response to the FIESTA-c sequence, we computed two

sets of values Mxy (β,φ) where $\phi \in \{0, \pi\}$. The magnitude of the signal from the voxel (S) was estimated as the magnitude of the weighted complex sum of the steady state transverse magnetization of all the spins in the voxel, for the single SSFP technique, and as the maximum of the magnitudes of the weighted complex sum of the steady-state transverse magnetization of all the spins in the voxel from each independent SSFP acquisition, for the multiple-acquisition SSFP.

So, for the FIESTA sequence:

$$S = \text{Magnitude}\left(\sum_{\beta} x_{\beta} Mxy(\beta)\right) \qquad [3.5a]$$

For the FIESTA-c sequence with N = 2:

$$S = \max\left(\text{Magnitude}\left(\sum_{\beta} x_{\beta} Mxy(\beta,0)\right), \text{Magnitude}\left(\sum_{\beta} x_{\beta} Mxy(\beta,\pi)\right)\right) \qquad [3.5b]$$

$$x_{\beta} = \frac{A(\beta)}{\sum_{\beta} A(\beta)} \qquad [3.6]$$

where A (β) represents total number of spins in the frequency bin β.

A total of 25 voxels were sampled from the bone marrow model. Estimate of the mean signal was computed as the mean of the signal from the 25 voxels. Assuming a bone fraction of 0.2 in the femoral trochanter (37) and 0.35 in the anterior part of the distal tibia and the calcaneus (56), we used this model to estimate the relative SNR performance of FIESTA and FIESTA-c sequences at the above anatomical sites at 1.5 and 3 T.

3.3.2 MR Experiments

Subjects

We studied eight normal healthy volunteers (age range 24–45 years, two female, six male) with their informed consent in accordance with the regulations of the Committee of Human Research at the University of California, San Francisco (UCSF). Three were imaged at the site of the proximal femur, two each at the sites of calcaneus and distal tibia, and one at both the sites of calcaneus and distal tibia, at field strengths of 1.5 and 3 T.

Image Acquisition

We acquired images on a 1.5-T Signa Scanner (General Electric, Milwaukee, WI, USA) using a U.S.A Instruments (Cleveland, Ohio, USA) four-coil surface phased array receiver coil and on a 3-T scanner (GE Signa) using a similar coil from Nova Medical (Wilmington, MA, USA). At both field strengths, the receiver consisted of two paddles, each housing two coil elements. For acquisitions at the sites of calcaneus and tibia, one paddle of the receiver was placed laterally and the other medially. For acquisitions at the site of the proximal femur, one paddle of the receiver was positioned anteriorly and the other laterally to the thigh. The gradient system had maximum amplitude of 40 mT/m and maximum slew rate of 150 mT/m/msec. The image acquisition matrix was 512 x 384 in all the scans. The calcaneus and tibia images, acquired in the sagittal and axial planes, respectively, have an in-plane resolution of 190 μm and a slice thickness of 500 μm. Coronal images of hip were acquired with an in-plane resolution of 234 μm. For FIESTA and FIESTA-c acquisitions, our imaging protocol was based on the optimization studies

presented above. The readout bandwidth (RBW) was adjusted to reduce the TR. However, choice of optimal parameters was constrained by gradient-induced heating and specific absorption rate (SAR) limits, especially at 3 T. For FGRE acquisitions, we used the existing optimized protocol (37).

Image Analysis

A total of 10 out of 28 slices of each image were used for the analysis. SNR was measured as the ratio of the mean signal, measured in the region of interest (ROI) and the standard deviation (SD) of the background noise, measured in a region of almost no signal. For consistency, ROIs were placed at identical position on each image. Although the sensitivity profiles of the surface coils have a spatial variation, we did not process the images with coil correction routines before taking SNR measurements so that the SNR metrics are not biased by the choice of coil-correction filters.

SNR efficiency was calculated as: $\frac{\text{SNR}}{\sqrt{\text{Scan time}}}$

3.4 Results

3.4.1 Characteristics of Simulated Magnetization Response

The shape of the magnetization profile depends mostly on tissue T1, T2, flip angle, and negligibly on TR. For T1 and T2 of marrow fat, magnitude of the transverse magnetization response is maximum around 60° (Fig. 3.2a and 3.2b) and the profile has a nearly flat-topped passband (Fig. 3.3a). The width of the flat top of the passband is

approximately $\frac{4\pi}{5}$ at both 1.5 and 3 T (Fig. 3.3 a, b). For the FIESTA-c sequence, using N =2 and the MI combination technique, greatest uniformity of profile was obtained at an optimal angle of 60° (Fig.3.3b). The ripple factor $\left(\frac{\max(Mxy) - \min(Mxy)}{avg(Mxy)}\right)$ of the FIESTA-c profile is 2.9 %.

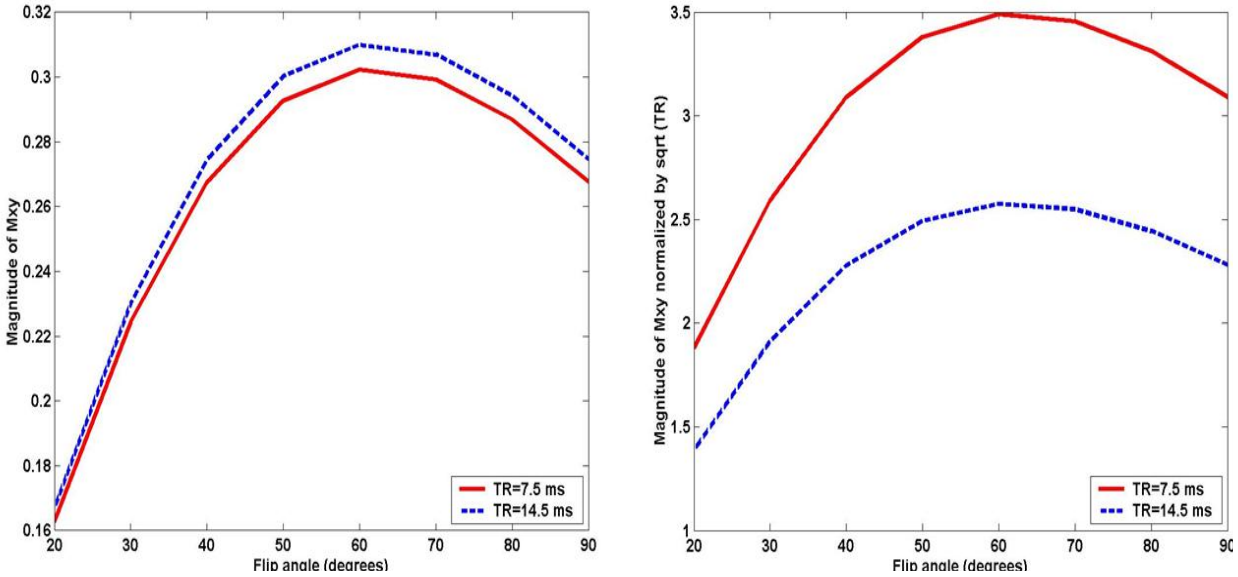

Figure 3.2a shows plots of the magnitude of Mxy with flip angle for two repetition times, TR=7.5 secs and 14.5 secs. Figure 3.2b show magnitude plots of Mxy normalized by square root of TR for the two above-mentioned TRs. TE = 3.4 ms for both cases and T1, T2 correspond to that of marrow fat at 3 T. From Fig. 3.2a, it can be seen that Mxy magnitude, which is proportional to SNR, is very similar for the two TRs. It is also seen that the maximum SNR yield is at a flip of 60°. From Fig. 3.2b, it can be seen that the magnitude of Mxy per unit square root of TR, which is proportional to SNR efficiency, is higher for the shorter TR.

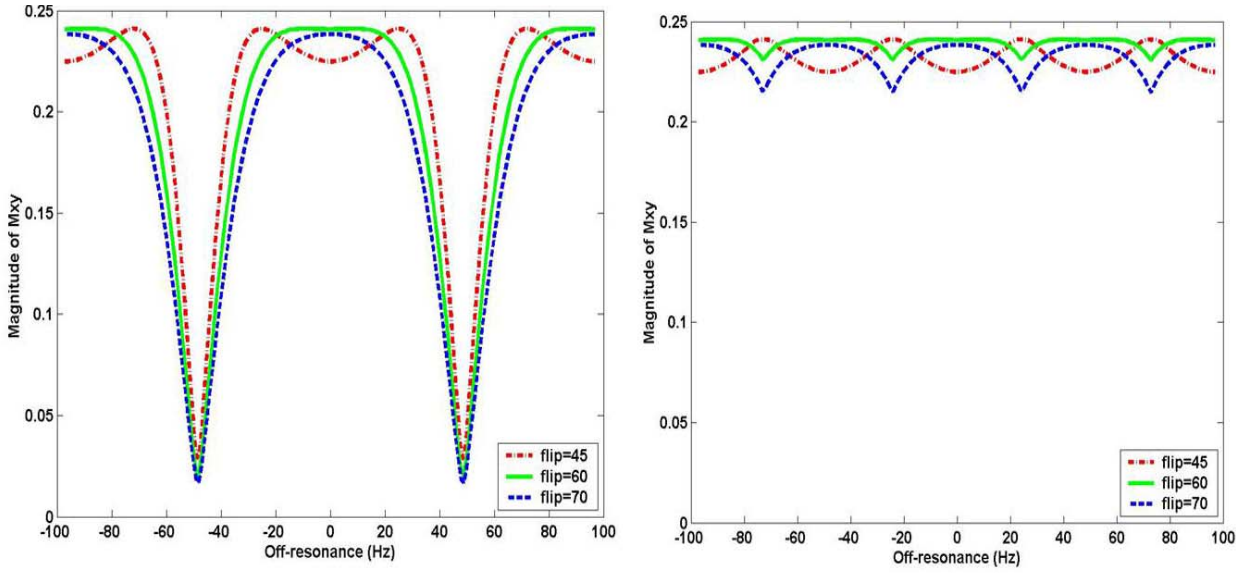

Figure 3.3 shows Mxy magnitude profiles over a range of off-resonances for flip angles of 45°, 60° and 70°. Figure 3.3a shows simulated Mxy magnitude profiles in response to single acquisition SSFP over a ± 2π variation in off-resonance. The profile has most uniformity in the passband for a flip angle = 60° with a passband width of $\frac{4\pi}{5}$*. Figure 3.3b shows Mxy magnitude profiles in response to multiple acquisition SSFP (N=2, MI) over a ± π variation in off-resonance frequencies. As in Fig a, a flip of 60° provides the most uniform profile and the ripple factor is only 2.9%. TR/TE=10.3/4 ms and T1, T2 correspond to that of marrow fat at 3 T.*

3.4.2 Intravoxel Frequency Dispersion

The range of frequency dispersion within a voxel sampled from the bone-model depends on the partial voluming of trabecular bone structures in the voxel and the voxel's proximity to neighboring trabeculae. Larger partial voluming gave rise to higher off-resonance frequency but smaller frequency dispersion within a voxel. Typical range of off-resonances observed in our simulation in a voxel with some partial voluming was around 30–35 Hz at 1.5 T and around 60–70 Hz at 3 T. The maximum off-resonance was observed to be around 62 Hz/124 Hz (1.5 T/3 T).For a TR =14 msec, a dephasing angle of π over TR corresponds to 35 Hz. Representative frequency histograms computed for

two voxels sampled from the bone-model at a bone-fractions of 0.37 and B0 = 3 T are shown in Fig. 3.4.

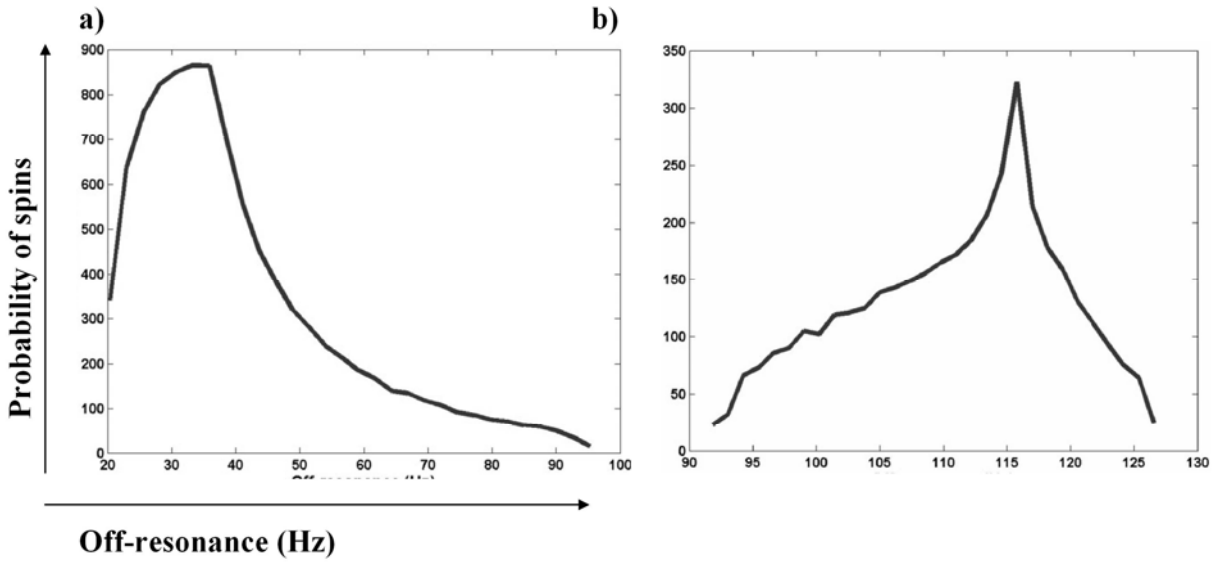

Figure 3.4 shows simulated distribution of off-resonant frequencies in two bone-marrow voxels; a: Frequency histogram in a voxel with some partial voluming. b: Frequency histogram of a voxel comprising mostly of bone. The distribution shows high off-resonance frequencies but a small range. These voxels were sampled from a bone model having bone fraction of 0.37 and at 3 T.

3.4.3 Optimization

Since the signal magnitude is almost independent of TR for TR<< T2 (20) as is shown in (Fig. 3.2a), theoretically, maximum SNR efficiency can be gained by using the shortest possible TR (Fig. 3.2b). However in the imaging experiment, for small FOV (≤10 cm), increasing the RBW degraded the sequence efficiency $\sqrt{\frac{\text{Readout Time}}{\text{TR}}}$ and at 3 T, TR increased with RBW (RBW > 32 kHz) because of gradient induced heating issues. The passband of the magnetization profile at the experimentally achievable minimum TR was approximately ± 40 Hz. While this bandwidth was sufficient to accommodate most of the

off-resonances at 1.5 T, it was not adequate in the case of the larger frequency dispersion at 3 T. At 3 T, optimal TR of the order of 7–8 msec could not be experimentally achieved. So multiple-acquisition SSFP (FIESTA-c) with N = 2 was employed to provide more uniformity to the response profile. Refocusing of static inhomogeneity induced phase dispersion at the time of echo is the basis of spin echo. A spin-echo-like refocusing of the transverse magnetization response to refocused SSFP at TE = TR/2 has been shown in the literature for dephasing between ±0.8π (13). However, larger range of off-resonances was observed in our simulation, especially at 3 T. Optimal TE with respect to refocusing of off-resonances depends on the distribution of off-resonant frequencies. Since this frequency distribution is different for each voxel (Fig. 3.4a and b), optimum value of TE is different for each voxel as well, complicating the optimization of TE. So TE was decided on the basis of whether it gave an acceptable TR.

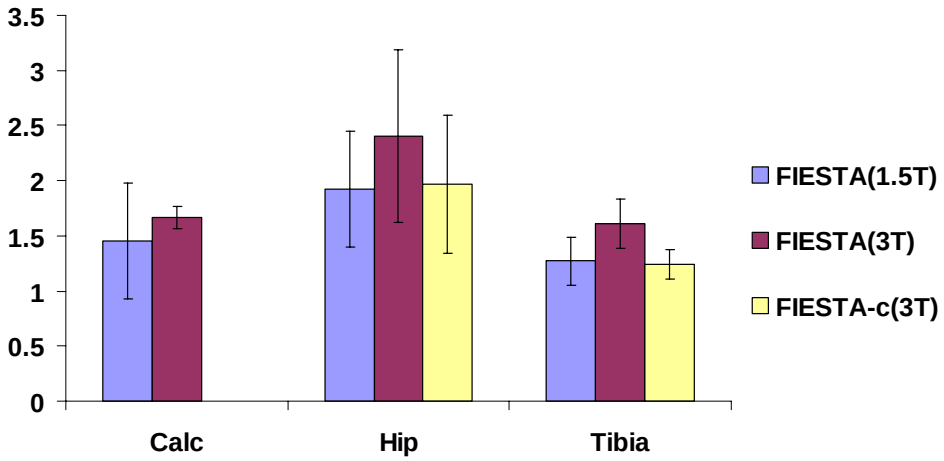

Figure 3.5 shows a plot of the mean SNR efficiencies obtained with the FIESTA and FIESTA-c acquisitions compared to FGRE at the anatomical sites of calcaneus, hip and tibia and at field strengths of 1.5 T and 3 T. The SNR efficiency of refocused SSFP acquisitions is higher than that of FGRE at both field strengths.

3.4.4 SNR and SNR Efficiency

The simulation predicted an increase in SNR efficiency by 1.4 times from 1.5 to 3 T at the site of the femoral trochanter and around 1.6 times at the tibia and calcaneus for the FIESTA sequence. At 3 T the SNR efficiency achieved with the FIESTA-c sequence (N = 2) was predicted to be around 0.85–0.9 times of that achieved with the FIESTA sequence.

With respect to SNR and SNR efficiency, the refocused SSFP sequences (FIESTA and FIESTA-c) outperformed the FGRE sequence in all the MR experiments. The mean SNR efficiencies obtained with each imaging sequence (FIESTA, FIESTA-c) compared to that obtained with the FGRE sequence at both field strengths are shown in Fig. 3.5. At 3 T, FIESTA-c acquisitions had the highest SNR, while their SNR efficiency was around 0.85 times that of the FIESTA acquisitions, which agrees with our theoretical estimate. As expected, 3 T afforded a boost in SNR from 1.5 T. The SNR efficiency improvement at the femoral trochanter with the FIESTA sequence was 1.3 times. The experimentally measured values of SNR efficiency improvements in FIESTA acquisitions from 1.5 to 3 T match fairly well with the theoretically predictions (Table 3.1). Representative images of the hip, and tibia and calcaneus acquired with FIESTA, FIESTA-c, and FGRE sequences are shown in Figs. 3.6 and 3.7 respectively. Scan times for the FIESTA acquisitions were six to eight minutes (two to three signal averages) and nine to eleven minutes (two to three signal averages) for the FIESTA-c acquisitions.

3.4.5 Susceptibility Effects, Image Contrast, and Image Quality

Banding artifact was not apparent on FIESTA images at 1.5 T. However at 3 T, loss of signal in the marrow due to susceptibility effects was visible in both FGRE and FIESTA

images (Fig. 3.6). Images acquired with the FIESTA-c sequence showed considerably reduced susceptibility effects and also had better image quality. Refocused SSFP images showed excellent structural detail due to high SNR and hence high contrast.

Figure 3.6 shows representative images of the proximal femur. a: Three-dimensional-FIESTA acquisition (1.5 T). b: Three dimensional- FIESTA acquisition (3 T). c: Three-dimensional-FGRE(3 T).d:Three dimensional- FIESTA-c (3 T). FIESTA images have a higher signal compared to the FGRE image. Consequently, their image texture depicts the trabecular orientations more clearly than the FGRE image. However, b shows pronounced loss of signal around the bone structures and deterioration of image quality, while these effects are significantly reduced in d.

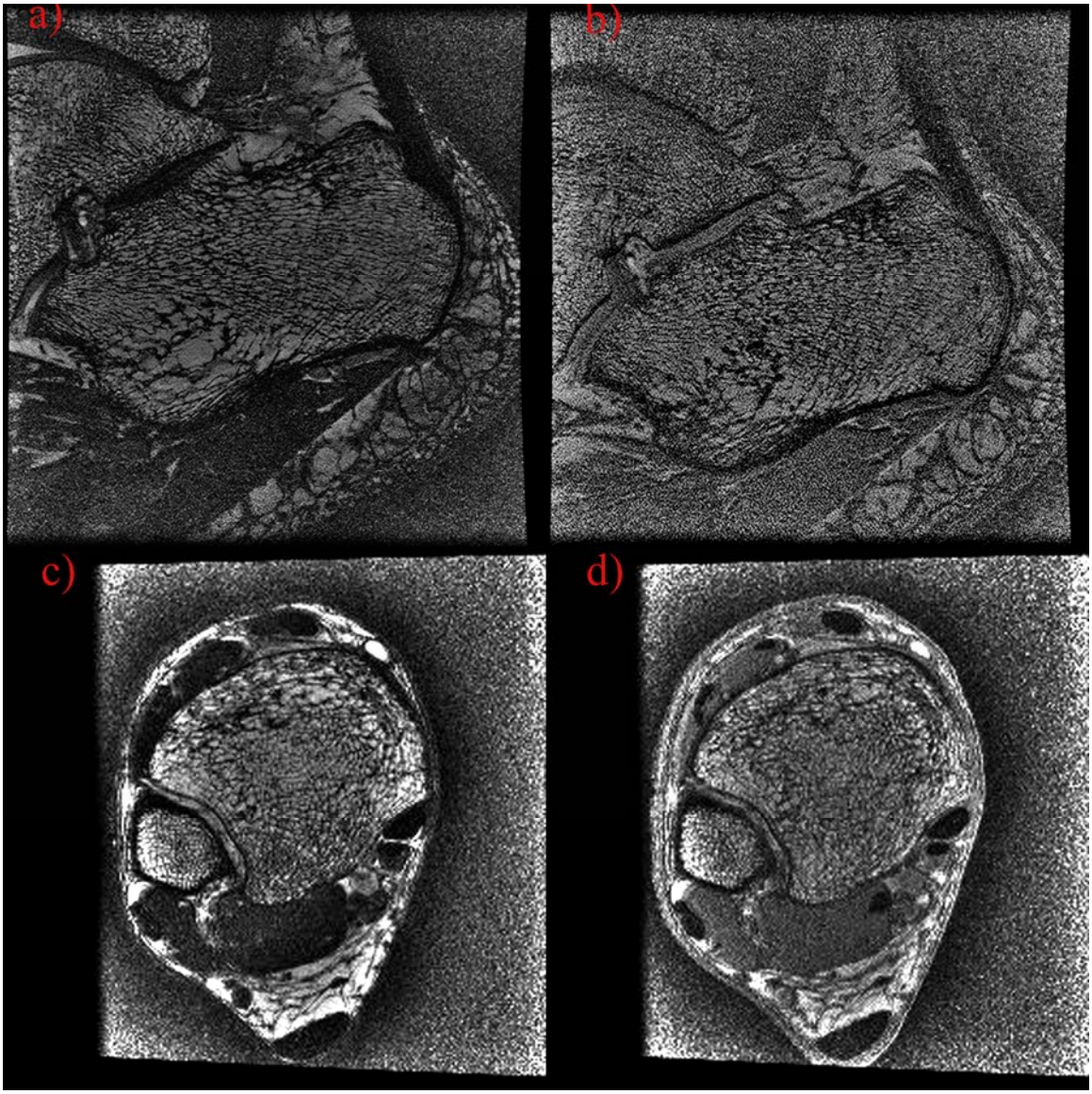

Figure 3.7 shows representative images of the calcaneus and distal tibia at 1.5 T.

a,b: FIESTA and FGRE images of the calcaneus from the same subject at 1.5 T. c,d: FIESTA and FGRE images of the tibia from the same subject at 1.5 T. These images show that even at 1.5 T it was possible to get a good depiction of trabecular micro-architecture with SSFP acquisitions.

Table 3.1 Theoretical Estimates and Experimental Results of 3T:1.5T SNR Efficiency Ratio for FIESTA acquisitions at each Anatomical Site

Anatomical Site	Theoretical SNRE ratio	Experimental SNRE ratio
Hip	1.4	1.35±0.36
Tibia	1.68	1.62±0.39
Calcaneus	1.65	1.75±0.05

3.5 Discussion

The magnetostatic model of bone was used solely to get an estimate of the intravoxel spread of frequencies and to predict the SNR performance for FIESTA and FIESTA-c sequences, and not to characterize magnetic and relaxation properties of trabecular bone tissue. Even though the model is not truly representative of the lattice structure of trabecular bone and does not consider differences in orientation of trabeculae relative to the magnetic field, and even though additional causes of inhomogeneity such as heterogeneity in the marrow were not considered, the theoretical predictions correlated well with the experimental results. We did not include any noise model in our simulation, but all our theoretical estimates are presented as ratios of signal efficiencies of sequence pairs, which we have treated equivalent to ratios of SNR efficiencies, the underlying simplifying assumption being that machine noise is similar for SSFP and FGRE sequences at the same field strength and that machine noise, being dominated by sample noise, scales linearly with B_0. Similarly, all the comparisons between theoretical and experimental results were made for ratios of SNR efficiencies, so SNR correction factor for magnitude operation (57) was not introduced. Differences in relative SNR efficiencies between the anatomical sites (Fig. 3.5; Table 3.1) can be attributed to several factors such as differences in experimental design (e.g., smaller FOV was used in scans of extremities

than in scans of the proximal femur) and differences in bone-volume fraction, to name a few. Theoretical and experimental results indicate that refocused SSFP techniques have great potential in the application area of trabecular micro-imaging. The FIESTA sequence performed well at 1.5 T (and hence FIESTA-c acquisitions were not performed in addition to these) but at 3 T, the FIESTA-c sequence seemed better-suited to the imaging application due to its robustness to susceptibility effects.

The SNR efficiency of FIESTA-c acquisition can be improved by using a customized reconstruction that employs MI technique in regions of banding and assigns an average of corresponding N pixel values to pixels in banding-free regions of the image. N = 2 seemed sufficient for removal of banding artifacts for our imaging application and a higher value of N would only prolong the scan time unnecessarily. Future improvements in gradient designs will also aid in employment of more optimal SSFP acquisitions. The ultimate goal of HR-MRI of trabecular bone is quantitative analysis of stereological measures such as App.TbTh and AppBV/TV for assessment of osteoporosis. Image analysis routines will be affected differently by different acquisition protocols (different sequences, different magnetic field strengths) due to differences in signal and noise characteristics of the images. Preliminary image analysis studies suggested higher values of AppBV/TV and App.TbTh for FGRE images compared to FIESTA images and higher AppBV/TV and App.TbTh values at 3 T compared to 1.5 T. Quantitative measures from FIESTA-c images at 3 T showed closest agreement with that obtained at 1.5 T. An exhaustive study on quantitative analysis of stereological measures derived from SSFP images at 1.5 and 3 T and their reproducibility is clearly warranted. However, this section focuses entirely on evaluating the SNR efficient refocused SSFP

methods for HR-MRI of trabecular bone, keeping in mind that low SNR yield impedes the imaging of trabecular micro-architecture at nonperipheral sites and necessitates long scan times, limiting clinical applicability. The *in vivo* images of the calcaneus, distal tibia, and the proximal femur acquired with fully-refocused SSFP techniques in a clinically feasible time had high SNR and SNR efficiency, and showed excellent structural detail. Typical scan times for FIESTA acquisitions were around six minutes. The scan times for FIESTA-c acquisitions, though twice that of FIESTA acquisitions, were still shorter compared to previously published values (37,58).

3.6 Conclusion

To conclude, this work analyzed two approaches for improving the SNR yield of *in vivo* high resolution MRI of trabecular bone MRI-employment of SNR efficient balanced SSFP pulse sequence and translation to a higher static magnetic field strength. The magnetic environment in bone marrow simulated based on a simplified model was used to estimate the signal behavior in response to SSFP and the higher field strength. Simulation results agreed closely with experimental results. To the best of our knowledge this is the first time that *in vivo* HR-MR images of the trabecular micro-architecture at the proximal femur has been presented. Hence, this work has also shown the feasibility of a technique for *in vivo* assessment of hip fracture risk. We believe that fully-refocused SSFP sequences can play a significant role in furthering the contribution of HR-MRI to the evaluation of trabecular bone structural organization. Furthermore, with the SNR leverage at 3 T, we are in a position to aim for further improving spatial resolution or reducing the scan time by employing parallel acquisition techniques.

Chapter 4

Parallel imaging techniques for high resolution imaging of trabecular bone micro-architecture

---

4.1 Motivation

The currently achievable spatial resolution for *in vivo* trabecular bone imaging is around 130-200 μm in-plane and around 500 μm through-plane. To facilitate registration of image volumes across patients or between exams for the same patient in a longitudinal study a sufficiently large volume comprising of 48-64 slices needs to be acquired. As a result, scan time is as long as 15-20 minutes causing patient discomfort and motion artifacts. The additional SNR gained from the higher field strength of 3 Tesla and the high magnetization yielding pulse sequence (Chapter 3) can be partly traded for acquisition speed. Previously, specialized k-space sampling trajectories such as spiral (59) and echo-planar-imaging (EPI) (20) were devised to accelerate MR acquisition by covering more k-space area per excitation. Compared to these, a more generalized technique for scan time reduction, partially parallel imaging (PPI) has recently evolved, which does not interfere with the spin magnetization itself and hence can be adapted with any MR sequence (60). Since trabecular bone MRI involves long acquisition times, PPI has great potential in this application area. In this chapter, we will implement PPI technique for HR imaging of trabecular bone micro-architecture and investigate whether certain image quality characteristics are different in PPI compared to conventional

imaging and whether these differences might lead to dissimilar trabecular depiction between the two. Additionally, the potential of PPI to improve the signal-to-noise ratio (SNR) efficiency of multiple acquisition fully refocused/ balanced SSFP (b-SSFP) (49) imaging protocols will also be explored.

4.2 Background

4.2.1. Parallel Imaging Techniques

Over recent years the field of partially parallel imaging (PPI) has seen rapid progress in terms of phased array coil design, novel image reconstruction techniques and new applications (10,61,62). In conventional phased array applications, an array of coil elements is used to receive the MR signal, instead of a single coil with the same coverage as the array, because of signal-to-noise ratio (SNR) advantages. The final MR image is obtained by calculating the square root of the weighted sum-of-squares or optimal pixel-by-pixel combination of the MR images obtained from each array element (63). PPI exploits the over-determinedness of such a system to accelerate MR acquisition. It reduces imaging time by undersampling the signal space such that the maximum sampling extent is unchanged, in the phase-encoding/partition-encoding direction (64-66). To describe PPI in further details, sampling in MR context must first be reviewed.

In MRI, signal is acquired in the Fourier domain. Sampling/ discretization in the Fourier domain results in periodic repetition in the image (conjugate) domain (Fig. 4.1). If the imaging object is space-limited i.e. if it has a finite extent, the minimum sampling rate (*Nyquist* rate) for which unambiguous image reconstruction is possible is equal to the

total extent (width) of the imaging object. As can be seen from Figure 4.1, when the Nyquist rate of sampling is met, unambiguous image reconstruction is possible by recovering one period of the image.

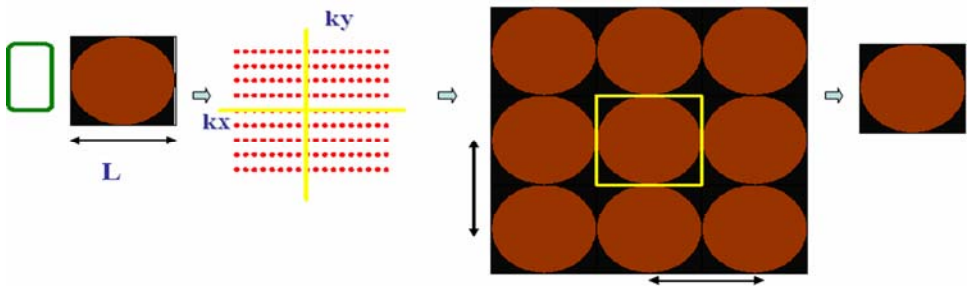

Figure 4.1 shows a schematic diagram of sampling of MR signal in the Fourier domain and the consequent periodic repetition in the image domain.

Undersampling the phase/partition-encoding axis by a factor of R reduces the field-of-view (FOV) of the image in that direction by the same factor, which gives rise to overlapping of the periodic repetitions or aliasing, as seen in Fig. 4.2. In PPI, the images are subsequently unaliased to their full FOV by using the spatial information in the elements of the receiver array. This "unaliasing" or "parallel reconstruction" can be performed either in the Fourier or the spatial domain.

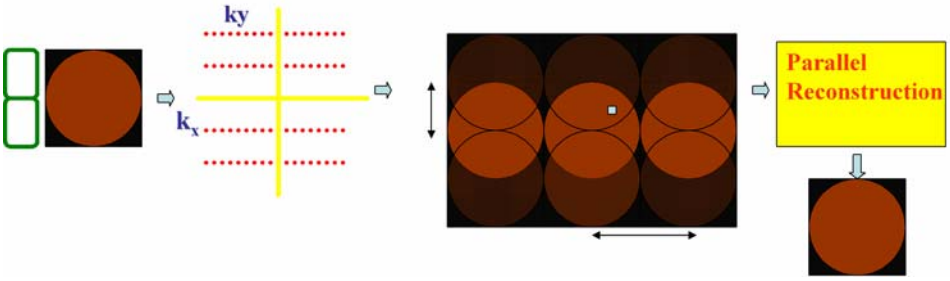

Figure 4.2 shows that undersampling in the ky direction results in reduction in field-of-view and aliasing artifact in the image and that unaliasing is performed by parallel reconstruction.

MRI signal measured by surface coils is modulated by coil sensitivity (63)

$$S(\mathbf{k}) = \int c(\mathbf{r})\rho(\mathbf{r})e_{\mathbf{k}_r,\mathbf{r}}\,d\mathbf{r}$$

$$m(\mathbf{r}) = \int \left[\int c(\mathbf{r})\,\rho(\mathbf{r})\,e_{\mathbf{k}_r,\mathbf{r}}\,d\mathbf{r}\right] e^{*}_{\mathbf{k}_r,\mathbf{r}}\,d\mathbf{k}_r \qquad [4.1]$$

where **r** represents 3D spatial coordinate, **k** represents 3D co-ordinate in k-space, c(**r**) represents coil sensitivity in position (**r**), ρ(**r**) is the magnetization in spatial position (**r**), S(**k**) is the signal measured at location **k** in k-space and m(**r**) is the measured image, after inverse Fourier transformation. The aliased pixel in a reduced FOV image obtained from a coil will have superposition of intensities of multiple pixels weighted by the coil sensitivity in those pixel positions (64). So the sensitivity weighting will be different in images obtained from different coils. The distinctness in measurements from different coil elements of a phased array arises from this, and allows unaliasing by "parallel reconstruction" (Figure 4.2).

Existing parallel reconstruction strategies can be broadly classified into direct inversion and indirect reconstruction techniques (67). The first class of methods employ direct estimation of the localized sensitivity of each coil element to unalias the reduced FOV image to full FOV (61,64,66,68,69). Sensitivity encoding (SENSE), the first and most widely practiced direct PPI technique (64) performs the unfolding in the image domain while techniques such as SPACE-RIP (61) perform the unaliasing in the frequency domain.

The intensity in a single aliased pixel in the reduced FOV image measured from different coils can be written as,

$$\mathbf{m} = \mathbf{C}\mathbf{v} + \mathbf{n} \qquad [4.2a]$$

where m: observation vector, C: coil sensitivity matrix, v: true image vector and n: Gaussian measurement noise vector

For an acceleration factor of R and K number of coils, dimensions of m, C and v are Kx1, KxR and Rx1 respectively.

$$C = \begin{bmatrix} c_{11} \ldots . c_{1R} \\ c_{21} \ldots . c_{2R} \\ . \\ . \\ c_{K1} \ldots . c_{KR} \end{bmatrix} \qquad [4.2b]$$

From 4.2,

$$\mathbf{v} = \mathbf{U}\mathbf{m} \qquad [4.3a]$$

$$\mathbf{U} = \left(\mathbf{C}^{\mathbf{H}} \boldsymbol{\psi}^{-1} \mathbf{C}\right)^{-1} \boldsymbol{\psi}^{-1} \mathbf{C}^{\mathbf{H}} \qquad [4.3b]$$

U is known as the unfolding matrix, [ψ] is the noise covariance matrix between the K channels and H denotes the Hermitian transpose operator (64).

The accuracy of direct parallel reconstruction depends on the accuracy of coil sensitivity estimation. In general, the sensitivity is estimated experimentally from a calibration scan. A calibration scan consists of a low resolution proton density-weighted scan. Individual coil profiles are computed by demodulating low resolution images from individual coils of intensity variations due to the object (64). Since coil sensitivity functions are spatially slowly varying, the rapidly varying intensities in the image are assumed to be due to the object. So the demodulation is accomplished by a combination of normalization and/or low pass and homomorphic filtering operations (64,70,71). However, estimation errors might arise from motion between calibration and actual scans and in regions of low signal such as air in the lungs (71).

Belonging to the second category, Autocalibrating-Simultaneous Acquisition of Spatial Harmonics (AUTO-SMASH) (72), Variable Density AUTO-SMASH (VD-AUTO-SMASH) (73) and Generalized Autocalibrating Partially Parallel Acquisitions (GRAPPA) (74) are methods that acquire a small set of additional phase-encoding lines at the Nyquist sampling frequency. These act as training lines for the estimation of the interpolation weights that are then used to synthesize the skipped phase-encoding lines from the acquired lines. Since the coil calibration is built into the actual acquisition in these methods, they are also known as autocalibrating (AC) techniques. GRAPPA has proved to be a particularly robust method since it reconstructs the full-FOV image of each individual coil element allowing a subsequent sum-of-squares or adaptive array combination (74). The sampling scheme for Cartesian autocalibrating acquisition is shown in Figure 4.3. GRAPPA employs a block-wise reconstruction in which 1 block consists of 1 acquired line and R-1 skipped lines for an acceleration factor of R. The interpolation weights for an individual coil j are obtained by least square fitting of the acquired lines from all the coils to the AC lines of the jth coil:

$$S_j(k_y - m\Delta k_y) = \sum_{l=1}^{K}\sum_{b=0}^{N_b-1} n(j,b,l,m) S_l(k_y - bR\Delta k_y) \qquad [4.4a]$$

where $S_j(k_y\text{-}m\Delta k_y)$ is the signal in the j^{th} coil at $m\Delta k_y$ offset from the $k_y{}^{th}$ PE position in k-space, N_b is the number of blocks used for the reconstruction, K is the number of coil elements and n(j,b,l,m) is the weighting of $S_l(k_y\text{-}bR\Delta k_y)$ for synthesis of Sj (k_y-$m\Delta k_y$) (74). The data-fitting for GRAPPA is schematically shown in Figure 4.4. By the assumption of spatial invariance of k-space data, the unacquired k-space data can be synthesized as a combination of acquired data weighted by the interpolation weights.

$$S_j(ky - m\Delta k_y - \delta) = \sum_{l=1}^{K} \sum_{b=0}^{N_b - 1} n(j,b,l,m) S_l(k_y - bR\Delta k_y - \delta) \qquad [4.4b]$$

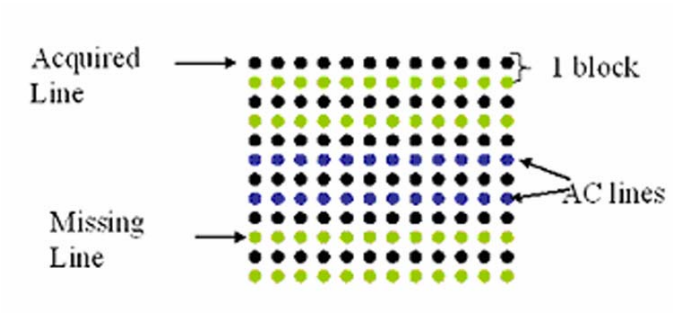

Figure 4.3 shows Cartesian variable density sampling for autocalibrating parallel acquisition with an acceleration factor, R=2 and 2 AC lines. Black, green and blue dotted lines indicate acquired PE lines, skipped PE lines and AC lines respectively. Several variations of the data fitting described above have been presented in the literature, such as performing the fitting piecewise for segments along the unaccelerated direction.

The disadvantage of parallel imaging is that the reduction in scan time comes at the price of SNR. The SNR in an image obtained by the PPI technique is at least $\frac{1}{\sqrt{R}}$ lower than that obtained with conventional fully gradient encoded acquisition (64,75).

$$SNR_{PPI} \propto \frac{SNR_{conv}}{\sqrt{R}} \qquad [4.5a]$$

SNR loss by a factor of $\sqrt{R}$ in an image obtained with parallel MRI (pMRI) is due to the fewer number of k-space samples acquired in the pMRI acquisition compared to fully sampled acquisition. In the process of synthesis of unaqcuired data samples from the acquired samples, additional noise correlations are introduced between them which amplifies noise variance by R and consequently degrades SNR by $\sqrt{R}$.

The relative noise enhancement factor over and above the $\sqrt{R}$ factor was introduced in the SENSE method as the geometry factor (g-factor).

$$SNR_{PPI} = \frac{SNR_{conv}}{g\sqrt{R}} \qquad [4.5b]$$

The geometry factor is so named because of its strong dependence on the coil geometry (10,64). The g-factor measure is different for every pixel in the image. For SENSE method (64), the g-factor in a pixel i can be computed as

$$g_{ii} = \sqrt{\left[\left(C^H \psi^{-1} C\right)^{-1}{}_{ii} \left(C^H \psi^{-1} C\right)_{ii}\right]} \qquad [4.6]$$

Analytical expression of geometry factor for GRAPPA method is less tractable. It is also not solely dependent on coil-geometry; there is some data dependence as well. From Eq. [4.4], GRAPPA reconstruction in k-space can be described as a convolution operation. Applying an inverse Fourier Transform on both sides of Eq. [4.4], we have:

$$I^{full}{}_j(i) = \sum_{l=1}^{K} I^{PPI}{}_j(i).N_j(i,l) \qquad [4.7]$$

From Eq [4.4] and Eq [4.7], the relative noise enhancement factor in a pixel i in the GRAPPA reconstructed image from coil j can be written as (76):

$$\sqrt{\sum_{l=1}^{K}\sum_{m=1}^{R}\left|N_j(i,m,l)\right|} \qquad [4.8]$$

and the composite g-factor for the coil combined image can be computed by a weighted sum-of-squares or any other type of array combination.

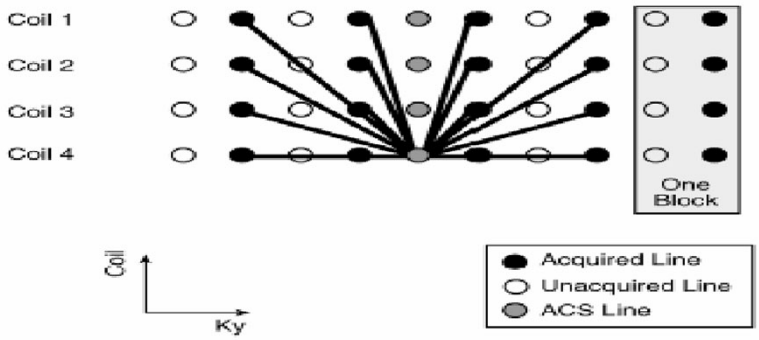

Figure 4.4 shows the data fitting in basic GRAPPA algorithm (Eq [4]) schematically. In GRAPPA several lines acquired in each coil of the array are fit to the autocalibration scan (ACS) line acquired in a single coil of the array.

While the initial applications of PPI were in the areas of cardiac and dynamic imaging (65,77-80), it is being adopted to newer MR fields every day due to the advantages of reduced patient discomfort, reduced motion artifacts, reduced distortion (81) and increased throughput provided by the accelerated acquisition. The relatively less explored application areas of PPI are those that involve very small FOV high resolution (HR) imaging. Griswold et al showed that unlike direct techniques, indirect reconstruction techniques such as GRAPPA can handle situations where the full-FOV is slightly smaller than the size of the object without any modification of the reconstruction code (67). This is also a common situation in small FOV trabecular bone imaging. However the effect of PPI on other aspects of small FOV HR-MRI such as visualization of small structures and their quantitative analysis, which is the focus of this work, has not been investigated. Because of the above mentioned advantages of GRAPPA reconstruction, our implementations of parallel imaging will be based on this method.

4.3 Methods

4.3.1 GRAPPA based reconstruction

To date, several variants of the GRAPPA reconstruction in terms of calibration strategy and reconstruction kernel been presented in the literature (82,83). Several modifications in the data fitting have been proposed , such as performing the data fit segment-wise in the k_x or frequency encode direction and excluding the central lines in the k_y or phase encode (PE) direction to avoid the dominance of high amplitude low frequency components in the calibration of coil weights (84). A cosine basis for spatial modeling of coil weights has also been presented (83). Wang et al proposed a floating node fitting (FNF) which allows any data point to be considered either as a source or a target node during the calibration as long as neighboring points are available for the data fitting (85). For a fixed number of AC lines, FNF provides more data fits compared to conventional GRAPPA and is particularly advantageous at higher reduction factors for getting sufficient number of fits without having to acquire a larger number of AC lines. The authors also proposed a multi-column multi-line interpolation (MCMLI) that uses the nearest neighboring points in the PE as well as the FE direction for reconstruction of missing lines (85). The synthesis of the missing lines in the MCMLI technique can be expressed as:

$$S_j(k_y - m\Delta k_y, k_x) = \sum_{l=1}^{L} \sum_{b_y=0}^{N_b-1} \sum_{b_x=-H_1}^{H_2} n(j, b_x, b_y, l, m) S_l(k_y - b_y R\Delta k_y, k_x - b_x \Delta k_x) \ldots \text{Eq [4.9]}$$

where b_x is the block index and $H_1 + H_2 + 1$ is the total number of blocks in the FE direction. Since the optimal GRAPPA reconstruction depends on the type of application and the coil configuration, multiple variations of the GRAPPA reconstruction (MCMLI,

FNF, segmented FE and different combinations of these) were programmed in MATLAB (Math Works, U.S.A) and tested on a simulated Shepp Logan phantom as well as acquired fully encoded data that were decimated to simulate several reduction factors, to determine an optimal GRAPPA based reconstruction for our experimental setup. In the phantom simulations, a B1 map of the receiver array was numerically computed by Biot Savart's Law (63). A multi column multi line interpolation with floating node fitting segment-wise along the FE axis was chosen as the optimal reconstruction based on minimum artifact power (AP).

$$AP = \sqrt{\frac{\sum_j \left(I_j^{Ref} - I_j^{PPI}\right)^2}{\sum_j \left(I_j^{Ref}\right)^2}} \qquad \text{Eq [4.10]}$$

where I_j^{PPI} represents the j^{th} pixel intensity in the accelerated image and I_j^{Ref} represents the j^{th} pixel intensity in the corresponding R=1 image. The chosen reconstruction algorithm consisted of a block-wise reconstruction using four blocks in the PE direction such that the source data from the blocks were placed symmetrically around the missing line, and two nearest neighboring columns in the FE direction.

Point spread function analysis

In a full FOV acquisition noise is assumed to be independent between different Fourier data points, since it is not spatially encoded. However in parallel reconstruction, since the missing data is acquired as a linear combination of the acquired data, noise correlations are introduced between Fourier data points, giving rise to spatially varying noise distribution in the reconstructed image. Because of this spatially varying characteristic of

the noise, SNR measured as the ratio of the average intensity in a region of interest (ROI) and the standard deviation of the background noise in parallel images have produced anomalous results, as reported in the literature (52) and customized measurement methods are warranted. As is obvious from Eq [4.7] and Eq [4.9] the noise correlations introduced will be different for each parallel reconstruction scheme, and hence the spatial noise variation in the image will also be different.

Generally, the effect of a filtering operation or reconstruction technique on the spatial resolution of an image is assessed by the point spread function (PSF). Here we will derive the PSF for the conventional GRAPPA reconstruction for the simplest case of R=2, number of blocks=1 and no sliding block operation and compare it to that of the standard reconstruction. A one dimensional image function will be assumed for the convenience of notation, and anti-Gibbs filtering will be neglected. The image intensity at a pixel j from the u^{th} coil in full FOV acquisition can be written as:

$$I_{ju} = \frac{1}{N}\sum_{k=0}^{N-1} S_{ku} W_{jk} \qquad \text{Eq. [4.11a]}$$

where S_{ku} is the k^{th} Fourier sample received by the u^{th} coil, N is the total number of samples and W_{jk} is the standard Fourier coefficient.

$$W_{jk} = \exp(\frac{i2\Pi jk}{N}) \qquad \text{Eq [4.11b]}$$

To derive the PSF, the true image function ρ_j is set to a delta function. Keeping in mind that the signal received by each coil is modulated by the coil sensitivity and denoting the coil sensitivity function of the u^{th} coil at the j^{th} pixel position by C_{ju}, S_{ku} can be expanded as:

$$S_{ku} = \sum_{j=0}^{N-1} C_{ju} \rho_j W_{jk} = C_{ju} \left| j = 0 \right. \qquad \text{Eq [4.11c]}$$

Separating even and odd lines, Eq [4.11a] can be rewritten as:

$$I_{ju} = \frac{1}{N} \left[\sum_{k=0:2:N-2} S_{ku} W_{jk} + \sum_{k=1:2:N-1} S_{ku} W_{jk} \right] \qquad \text{Eq [4.11d]}$$

Combining Eq [4.11c] and Eq [4.11d],

$$I_{ju} = \frac{C_{ju} \left| j = 0 \right.}{N} \left[\sum_{p=0}^{\frac{N}{2}-1} W_{j(2p)} \left(1 + \exp\left(\frac{i2\Pi j}{N} \right) \right) \right] \qquad \text{Eq [4.11e]}$$

Similarly, the image intensity at a pixel j in the GRAPPA reconstructed image from a coil u can be written as:

$$I_{ju}^{\text{GRAPPA}} = \frac{1}{N} \left[\sum_{k=0:2:N-2} S_{ku} W_{jk} + \sum_{k=1:2:N-1} \sum_{l=1}^{L} n_l S_{(k-1)l} W_{jk} \right]$$

$$= \frac{C_{ju} \left| j = 0 \right.}{N} \sum_{p=0}^{\frac{N}{2}-1} W_{j(2p)} \left[1 + \frac{\exp(\frac{i2\Pi j}{N})}{C_{ju} \left| j = 0 \right.} \sum_{l=1}^{L} n_l C_{jl} \left| j = 0 \right. \right] \qquad \text{Eq [4.11f]}$$

For both the full FOV and GRAPPA reconstruction, the final image is obtained by sum of squares combination of individual coil images. However, as can be seen from Eq [4.11e] and Eq [4.11f], the PSF of the conventional fully encoded reconstruction does not contain any data dependent terms, while the PSF of the GRAPPA based reconstruction carries data dependent terms, n. For the special case of $\frac{\sum_{l=1}^{L} n_l C_{jl} \left| j = 0 \right.}{C_{ju} \left| j = 0 \right.} \approx 1$, the expressions in Eq

[4.11e] and Eq [4.11f] are nearly identical. Because of this data dependence, a fixed relation between the PSF of the conventional reconstruction and the GRAPPA based reconstruction cannot be established- therefore empirical assessments need to be employed to asses the effects of GRAPPA reconstruction on the effective image resolution.

4.3.2 Simulation study of SNR efficiency increase in multiple b-SSFP with PPI

. When imaging magnetically heterogeneous tissue environments such as the trabecular bone-marrow with a b-SSFP sequence at relatively higher fields, multiple acquisition b-SSFP (m-bSSFP), which employs multiple phase-cycled acquisitions, is used to reduce the sensitivity of the sequence to off-resonance artifacts at the cost of scan time and SNR efficiency (50). The data from the N independent phase-cycled acquisitions can be combined by maximum intensity projection (MIP), sum-of squares (SOS) or complex sum (CS) (49). A simulation of the steady state transverse magnetization response to b-SSFP, based on linear systems analysis (51), was used to compute the multiple SSFP magnetization response for different values of N and different combination techniques. The ripple factor of the response is generally defined as the ratio of the difference between the maximum and minimum values of the response and the mean value of the response. For relaxation parameters corresponding to fatty bone marrow at 3 T and an optimal flip angle of 60°, the ripple factor for the SOS technique (29 %) is much poorer compared to MIP (4%) at N=2 (Fig 4.5), so in spite of the SNR advantages provided by the former, the latter technique is preferable for bone marrow imaging at N=2 because of better artifact reduction. However, if larger values of N (N>2) can be accommodated

within the same or shorter scan time, the SOS combination can be used for the SNR advantage without compromising much on artifact reduction. This can be seen from the plot of the magnetization profile from SOS and MIP combination for N=3 (Fig 5). A distribution of off-resonances was simulated by a simplified bone-marrow magnetostatic model (12) to estimate the SNR yield from an N=3 protocol with SOS combination method acquired with PPI (R=2) and from an N=2 protocol with MIP combination method acquired with conventional full gradient encoding. SNR efficiency was measured as the SNR divided by the square root of acquisition time.

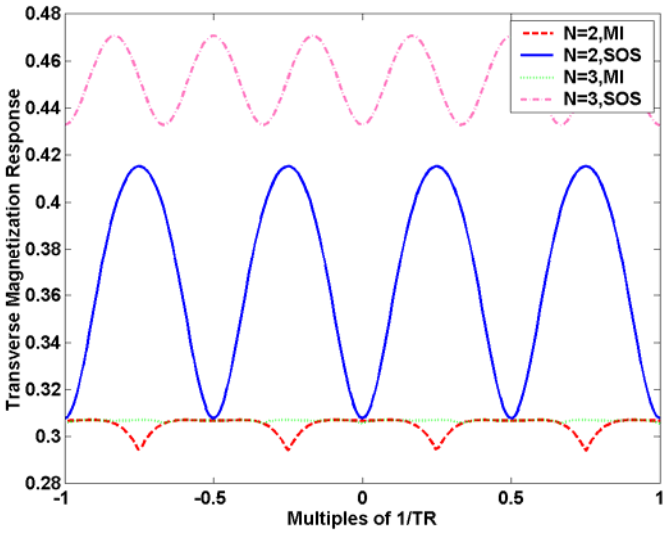

Figure 4.5: Plots of the simulated transverse magnetization response to multiple acquisition b-SSFP sequence for MIP and SOS combination methods in the cases of 2 and 3 phase- cycled acquisitions are shown. T1 /T2 values (365/133 milliseconds) corresponding to that of fatty marrow at 3T were used in the simulation. Flip angle was 60°. The plots show that the SOS combination yields higher signal than the MIP combination for both N=2 and 3, but at N=2, the magnetization profile for SOS has poor uniformity.

4.3.3 MR Materials and Methods

A 3D b-SSFP product sequence with multiple phase-cycling capabilities, 3D Cycled Fast Imaging Employing Steady State Acquisition (FIESTA-C) (13) was modified in Environment for Pulse Programming In C (EPIC) to incorporate autocalibrating Cartesian VD acquisition. MR experiments were conducted on eight healthy human subjects in accordance with the regulations of the Committee of Human Research (CHR). Two volunteers were imaged at the site of the ankle (calcaneus) with an eight channel phased array head coil (MRI Devices, WI, USA) and three volunteers each were imaged at the knee (distal femur) and at the hip (proximal femur) with a custom built eight channel dual phased array receiver (86) for reduction factors of R=1-4. For all parallel acquisitions a total of 12 AC lines were acquired. In each case the modified 3D FIESTA-C sequence was employed with 2 phase cycles, 60° flip angle and a partial echo sampling 0.61 fraction of the frequency encode axis. The acquisition matrix was 512x384. A 32 slice dataset of the ankle was acquired in the sagittal plane with an in-plane resolution of 190 μm and slice thickness of 500 μm with TR/TE/BW of 11.4/2.8/32 milliseconds (ms)/ms/KHz. The scan time for the fully gradient encoded acquisition (R=1) was around 9 minutes and 19 seconds. Scan times for R=2,3 and 4 were 4 minutes 48 seconds, 3 minutes and 10 seconds and 2 minutes and 20 seconds respectively. For the knee and the hip, we acquired two sets of short scans and one set of longer scan. The rationale behind this was to examine the importance of the baseline SNR (SNR of the R=1 acquisition) on the quality of the parallel imaging reconstruction. For the shorter (longer) acquisition at the knee, a 16 (42) slice dataset was acquired with the dual phased array coil in the axial plane with an in-plane resolution of 190 μm and slice thickness of 500 μm, TR/TE/BW of 10/2.7/32 ms/ms/KHz, for a fully gradient encoded acquisition time of 4 minutes (10

minutes 45 seconds). Scan times for R=2, 3 and 4 were 2 minutes and 4 seconds (5 minutes 33 seconds), 1 minute 28 seconds (3 minutes 46 seconds), and 1 minute (2 minutes 52 seconds) respectively. For the shorter (longer) acquisition at the hip, a 32 (48) slice dataset was acquired with the dual phased array coil in the coronal plane with an in-plane resolution of 234 μm and slice thickness of 1000 μm, with TR/TE/BW of 8.2/2.3/42 ms/ms/KHz, for a fully gradient encoded acquisition time of 7 minutes 26 seconds (11 minutes 10 seconds). Scan times for R=2, 3 and 4 were 3 minutes 46 seconds (5 minutes 47 seconds), 2 minutes 30 seconds (3 minutes 55 seconds) and 1 minute 53 seconds (2 minutes 59 seconds) respectively.

For the SNR efficiency improvement experiments with m-bSSFP protocol, an additional scan with N = 3 phase cycles and R=2 was conducted on two of the volunteers at the hip, one with the shorter acquisition and one with the longer acquisition. In the first case the scan time was 5 minutes 17 seconds and in the second case it was 8 minutes 40 seconds. As the full FOV was smaller than the size of the object in several cases, especially at the hip and the ankle, the No Phase Wrap (NPW) imaging option, which employs twice oversampling in the phase direction, was chosen in all the high resolution scans. Only one signal average was employed in all the high resolution scans. Also, a low resolution image was acquired with a 2D gradient echo sequence and 64x64 acquisition matrix for one volunteer at each anatomical site for experimental estimation of the maximum feasible acceleration factor in the encoding direction of the coils.

4.3.4 Image Reconstruction

The raw data from the acquisitions was moved to a Sun Workstation (Solaris, U.S.A.). All the images were reconstructed offline using reconstruction routines programmed in MATLAB. As the size of the imaging object was in some cases too small for the eight channel receiver array in the ankle setup, an automatic coil selection routine was employed to discard data from coils that mainly contributed noise. The algorithm decided whether to select a coil, based on the ratio of the normalized signal and noise energies in the dataset received by the coil. A threshold value for this ratio was chosen empirically. In the case when number of coils chosen was fewer than five, the threshold was adjusted iteratively till the criterion for minimum number of selected coils was met. Based on the assumption that peripheral k-space is dominated by noise, signal energy was estimated from the normalized energy of the central k-space with radius = 0.8 of the maximum length in the x and y dimensions, and the noise energy was estimated from the normalized energy in the peripheral k-space. The coil selection routine was also used with the PPI datasets. For the parallel acquisitions, the above mentioned GRAPPA reconstruction with MCMLI-FNF segmented in the FE direction was applied. Since all the high resolution images were acquired with a partial echo, a homodyne reconstruction was applied in the FE direction. The reconstructed full-FOV images from all the N phase-cycled acquisitions from each individual coil were combined by the MIP method for N=2 and by the SOS method for N=3 phase-cycles. For both the conventional (R=1) and accelerated images the final image was computed by the weighted sum of squares combination of the individual coil images.

GRAPPA-based reconstruction of large image volumes from data acquired from 8 or more channels is computationally intensive, taking several hours on a single desktop

Sun (Solaris, USA) workstation. To expedite reconstruction, a parallel computational strategy was devised to distribute the reconstruction of individual image slices to separate CPUs on a Linux cluster. This has been described in more detail in Appendix A.

4.3.4 Image Analysis

Evaluation of encoding capability of array coil

Since coil sensitivity modulations have a low spatial frequency, coil sensitivity functions are usually assessed from low resolution images of the object. The acquired low resolution images were used to estimate the maximum feasible acceleration factor allowed by a receiver array in the PE direction for each of our experimental setup. Individual coil images were projected onto the PE axis and principal component analysis (PCA) was performed on the covariance matrix of the projected images (87). Principal Component Analysis is performed by Karhunen–Loeve transform to reduce data dimension (88). Given a complex vector x of dimension nx1, the KL Transform of x can be described by a square matrix T_{KL} of maximum rank m ($\leq$n) that minimizes

$$J_{KL}(T) = E\{\|x - Tx\|^2\} \qquad \text{Eq [4.12a]}$$

where E denotes the expectation and || || denotes the Frobenius norm. The matrix T is a projection matrix onto principal subspace of rank m of the covariance matrix

$$R_x = E\{xx^H\} \qquad \text{Eq [4.12b]}$$

If the eigen decomposition of R_x is given by

$$R_x = \sum_{i=1}^{n} \lambda_i \mathbf{e_i} \mathbf{e_i}^H \quad \lambda_1 \geq \lambda_2 \geq \lambda_n \qquad \text{Eq [4.12c]}$$

$$\text{then, } \mathbf{T} = \mathbf{P}\mathbf{P}^H \quad \mathbf{P} = [\mathbf{e}_1 ... \mathbf{e}_m] \qquad \text{Eq [4.12d]}$$

where $\mathbf{e}_i$, the eigen vectors are also called principal components. In our case, each column in the covariance matrix corresponded to observation from an individual coil element. So, the data projected onto the principal component corresponding to the largest eigenvalue would explain largest percentage of the variance in the observation datasets. So, if for an K coil dataset, K-C principal components contributed negligibly to the variability in the observations, we could infer that the approximate rank of the observation dataset was C, and the encoding capability of the coil array might be exceeded for acceleration factors R>C.

Histogram and periodogram analysis

GRAPPA based reconstruction introduces correlations between data points in k-space. This can affect the pixel intensity distribution, correlation between pixels intensities and consequently the spatial resolution. To investigate this, the pixel intensity distribution and autocorrelation were analyzed in the high resolution images. The pixel intensity distribution of images was examined from their histogram plots. Peak height and peak position of the histograms were compared between R=1 and accelerated images. Power spectrum of the images was estimated to examine the pixel intensity autocorrelations (PIA) of conventional and accelerated images. Through the Wiener Khintchine theorem, the power spectrum of a well behaved stationary random process is equal to the Fourier Transform of its autocorrelation sequence (89).

$$P_x(e^{j\omega}) = \sum_{k=-\infty}^{\infty} r_x(k)e^{-jk\omega} \qquad r_x(k) = E\{x(n+k)x^*(n)\} \qquad [4.13]$$

Here $P_x(e^{j\omega})$ and r_x represent the power spectrum and autocorrelation of x and E is the expectation operator. Power spectrum of the image was estimated from periodogram

which was computed by Barlett's method of periodogram averaging (90). This involves computing periodogram $P_{per}(e^{j\omega})$ for K partitions of length L of the image and computing the power spectrum estimate $P_x(e^{j\omega}\tilde{)}$ as the mean of these periodograms (90).

$$P_{per}^{(i)}(e^{j\omega}) = \frac{1}{L}\left|\sum_{n=o}^{L-1} x_i(n)e^{-jn\omega}\right|^2 ; i = 1,2..K$$
$$P_x(e^{j\omega}\tilde{)} = \frac{1}{K}\sum_{i=1}^{K} P_{per}^{(i)}(e^{j\omega}) \qquad [4.14]$$

Here for convenience of notation, the image has been represented by a 1D sequence. The periodogram was used to assess if the PIA was similar between R=1 and accelerated image. More energy in the inner Fourier space of the periodogram for accelerated datasets would imply more slower decaying PIA components. This might also indicate a broadening of the PSF. On the other hand, more high spatial frequency components in the autocorrelation might arise from reconstruction noise and manifest as higher energy in outer Fourier space in the periodogram.

SNR Measurements

Experimentally, SNR is often measured as the ratio of the average intensity in a region of interest (ROI) and the standard deviation of the background noise. But due to the spatially varying distribution of image noise, this measurement technique has produced anomalous results in PPI and preferably more rigorous measurement from repeated acquisitions should be used (52). In this work we used two successive acquisitions for the SNR measurements. A region of interest (ROI) was placed in the identical location on each of the two images and the average SNR in the ROI was determined as the ratio of

average signal in the ROI in the mean image and the standard deviation of the signal in the difference image (52) .

$$\mathrm{SNR} = \frac{\sqrt{2}\,\mathrm{mean}((\mathrm{I(r,1)} + \mathrm{I(r,2)})/2)}{\mathrm{stdev}(\mathrm{I(r,1)} - \mathrm{I(r,2)})} \qquad \text{Eq [4.15a]}$$

SNR Efficiency was calculated as:

$$\mathrm{SNREff} = \frac{\mathrm{SNR}}{\sqrt{\mathrm{Scan\ Time}}} \qquad \text{Eq [4.15b]}$$

Measurement of trabecular bone structural parameters

Since structural parameters of trabecular bone micro-architecture are morphology metrics, ideally, all acquisitions obtained from the same subject should yield identical measurements of these parameters, irrespective of the imaging technique. However the quantitative analysis is sensitive to imaging parameters. Consequently measurement values can differ from one acquisition to another. For this reason, we derived structural measures from the images and investigated the deviations in the measurement values between PPI and R=1 datasets. Five slices were used from each image-set for the quantitative analysis. A low-pass filter (LPF)-based coil sensitivity correction was first applied to the images so that structural measurements would not be biased by spatial variations in the coil sensitivity. ROIs were manually placed in the identical location on all corresponding images in an acquisition dataset. In the calcaneus images, the ROI was placed in the trabecular bone of the posterior calcaneus. In hip images ROIs were placed in the femoral trochanter and in the knee images ROIs were placed in the anterior part of the distal femur. Image analysis software (32) developed in our lab was used to quantify the structural parameter, apparent trabecular number (App. TbN on the binarized images

by previously described techniques (30,32). In this work we computed only one structural measure; App. TbN.

.4.4 Results

4.4.1 Simulations

GRAPPA based reconstruction

In simulation studies the GRAPPA based reconstruction seemed to preserve the visualization of small structures in the image. Line profiles, derived from a full dataset of the knee from which PE lines were selectively removed to simulate various reduction factors, show an excellent matching of edges and comparable edge sharpness between R=1 and the accelerated images (Fig 4.6). However the line profile from R=4 shows slight smoothing of edges and some exaggerated edges because of enhanced noise (Fig 4.6).

Using the magnetostatic bone model and the simulation of the SSFP magnetization response, the SNR efficiency with N=3 phase-cycles, SOS combination acquired with PPI, R=2 was estimated to improve by 20 % from that obtained with full FOV acquisition, N=2 phase- cycles and MIP combination.

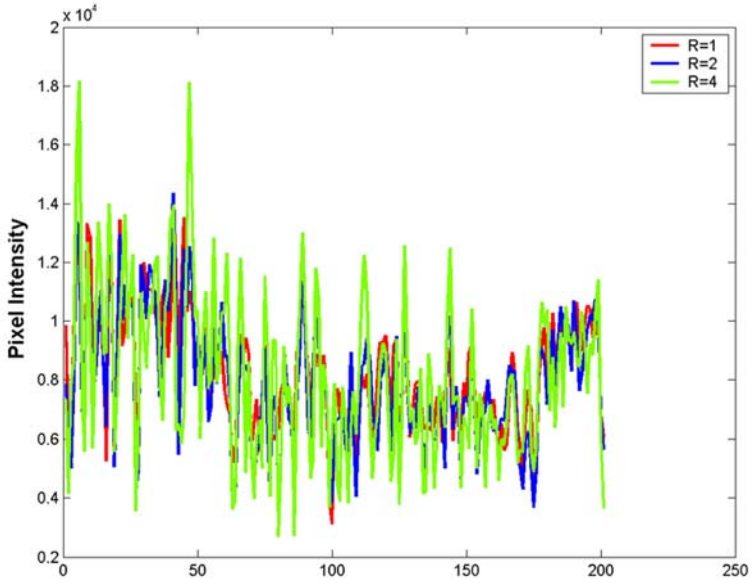

Figure 4.6: Line profiles from a full FOV knee image and from simulated PPI images for R=2, 3 and 4 that were reconstructed by the GRAPPA based algorithm are shown. The plots show good coincidence of edges between the line profiles from the full FOV and the simulated PPI images. But at R=4, some exaggeration of edges due to enhanced noise and slight edge smoothing is observed.

4.4.2 Experiments

Evaluation of encoding capabilities of coils

The eigenvalues (normalized to 1) obtained by PCA of the coil sensitivity covariance matrix of the head array and the dual phased array for the three experimental setups used in our work are plotted in Fig 4.7. For the calcaneus imaging setup, the eigenvalues decrease linearly between the first and third principal coil component and the eigenvalues corresponding to the fifth principal component onwards are much lower in value. So only 3-4 of the eight principal coil components contribute significantly to the spatial encoding capabilities of the system. This implies that even though theoretically we can achieve acceleration equal to the number of coils used, the maximum feasible acceleration for this setup is around 3-4. Employment of higher reduction factors will result in poor

reconstruction associated with large noise amplification. Although both the knee and the hip setup employed phase–encoding in the left-right direction, the former, which was acquired in an axial plane has a higher maximum feasible acceleration compared to the latter which was acquired in the coronal plane. The maximum allowable reduction/acceleration with the knee setup is around 5-6

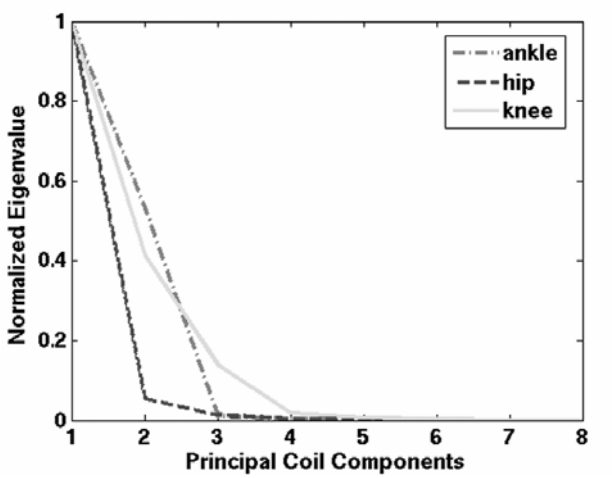

Figure 4.7: Plot of the eigenvalues obtained by PCA of the covariance matrix formed from the projection of coil sensitivities along the phase encoding direction for the ankle, hip and knee imaging setup are shown. The maximum allowable acceleration, indicated by the number of principal components with non-negligible eigenvalues, is 3-4 for the calcaneus and hip experimental setups and 5-6 for the knee experimental setup, in the employed phase-encoding direction.

Assessment of image quality

At the calcaneus, the image quality was preserved in terms of trabecular depiction till R=3 but was degraded at R= 4, which is expected from the PCA plot (Fig 4.8). As can be seen from Fig. 4.8, the visualization of trabecular micro-structure in Fig. 4.8a (FIESTA-C

image with N=2, R=1) is very similar to that in Fig. 4.8b (FIESTA-C image with N=2, R=2) and Fig. 4.8c (FIESTA-C image with N=2, R=3).

At the knee, good reconstruction was obtained till R=3 (Fig 4.9b), but deteriorated at R=4 because of low SNR in the shorter acquisition. The R=3 image (Fig 4.9b), acquired in scan time of merely ninety seconds, shows very good depiction of trabecular micro-structure. For the longer acquisition, a high quality reconstruction was achieved even at R=4 (Fig 9d), as expected from the results of the PCA analysis. It is to be remembered that the SNR loss in images acquired with PPI compared to the R=1 case is mostly due to enhancement in noise. Signal intensities are very similar between the images. This fact might explain why visually, Fig 4.9b and 4.9d are very similar to Fig. 4.9a and 4.9b respectively. At the hip, images retained their visual quality till R=3 (Fig 4.10b) for the shorter acquisitions. In the longer scan the image quality was preserved to some extent at R=4. (Fig. 4.10d).

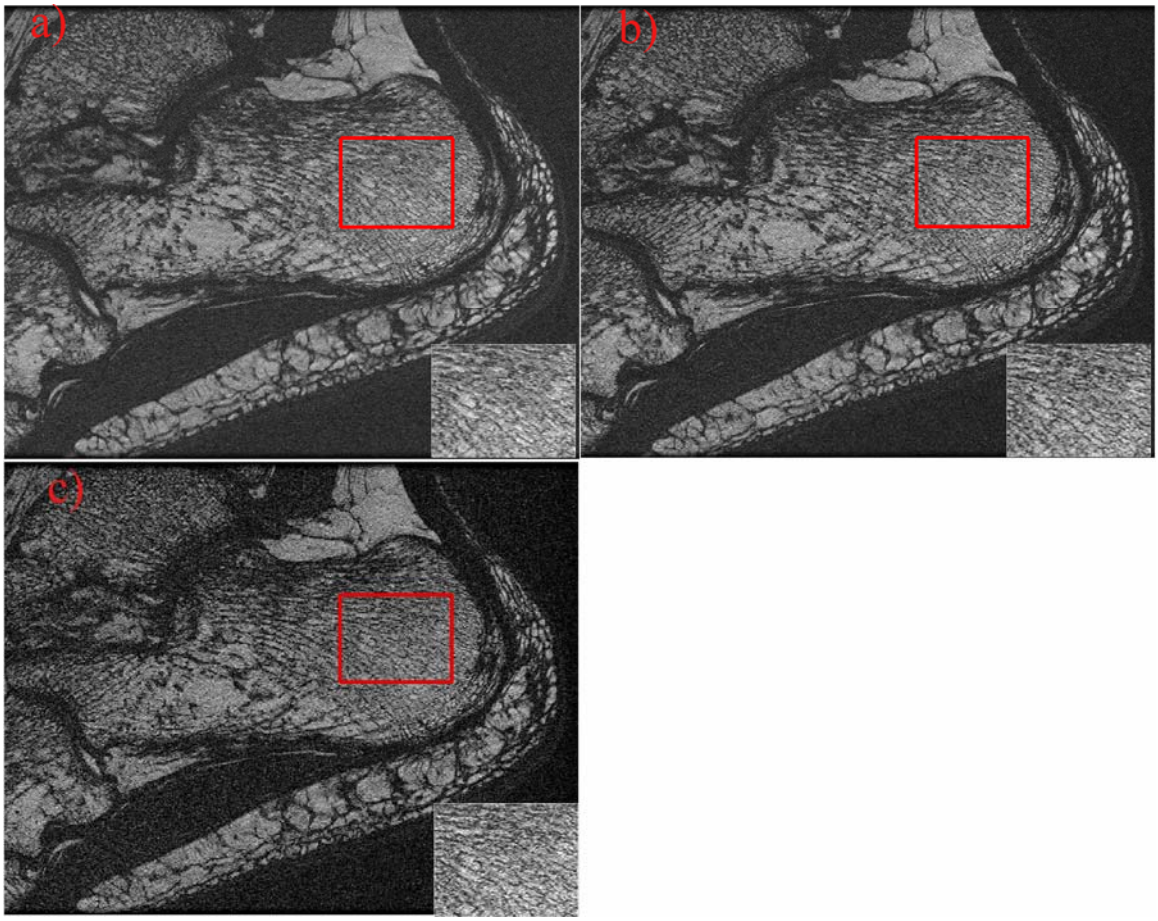

Figure 4.8 shows the trabecular bone structure at the calcaneus acquired with the FIESTA-C (N=2) with A: no acceleration B: two fold acceleration C: three fold acceleration. A magnified view of the trabecular micro-structure in each image has been provided in zoomed inset. Scan time for the conventional, R=2 and R=3 FIESTA-C acquisitions was 9 minutes 19 seconds, 4 minutes 48 seconds and 3 minutes 10 seconds respectively.

.

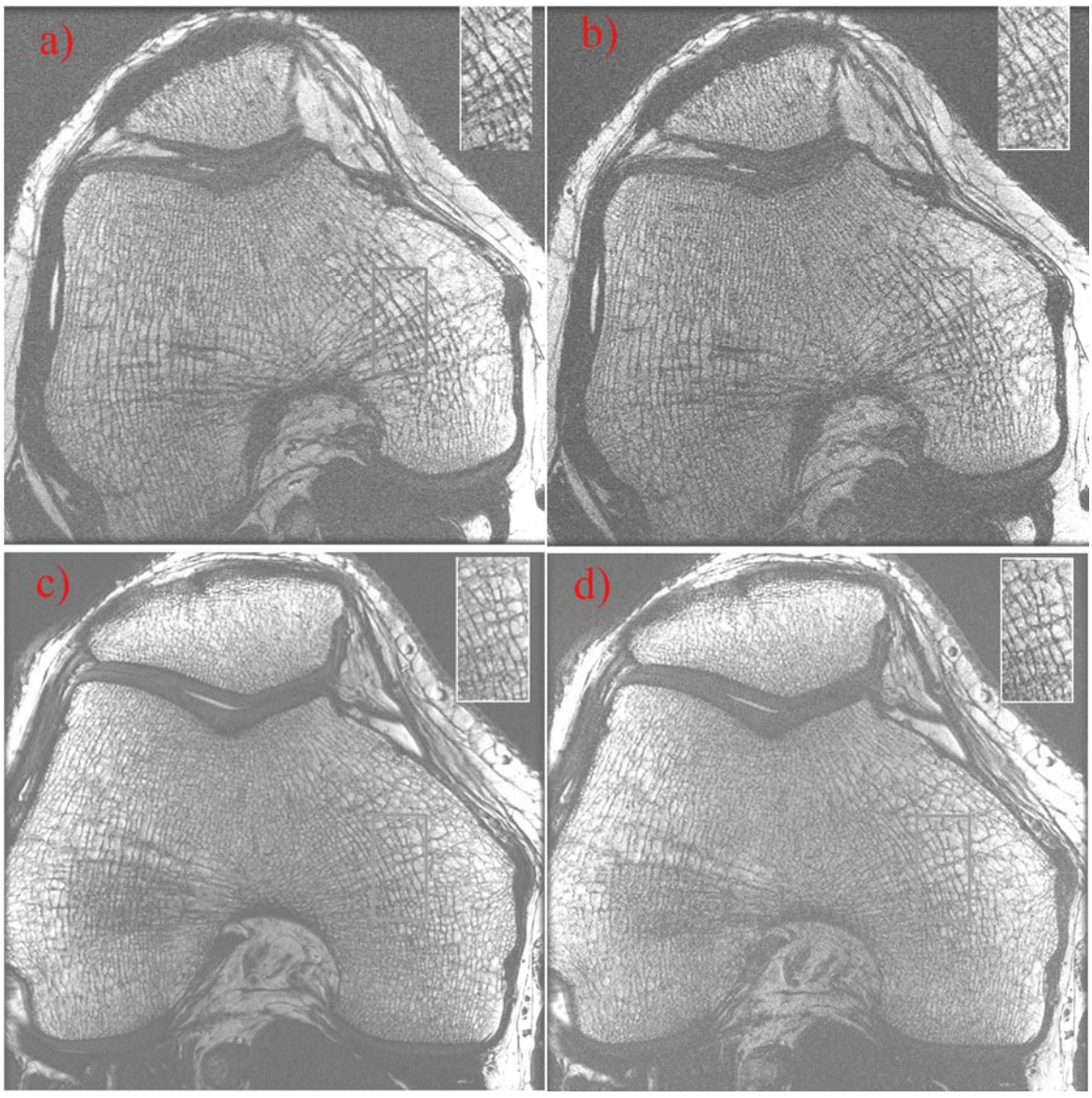

Fig. 4.9a and b show representative conventional (R=1) and R=3 images of the knee for the shorter acquisition. Acquisition times were 4 minutes and 1 minute 28 seconds respectively. Fig 4.9 c and d show R=1 and R=4 images of the knee from the longer acquisition. Acquisition times were 10 minutes 45 seconds and 2 minutes 45 seconds respectively. The visualization of structures has been very well preserved in both the accelerated images (Fig 4.9 b and d), as can be observed from the magnified views of trabecular micro-structure provided with the images.

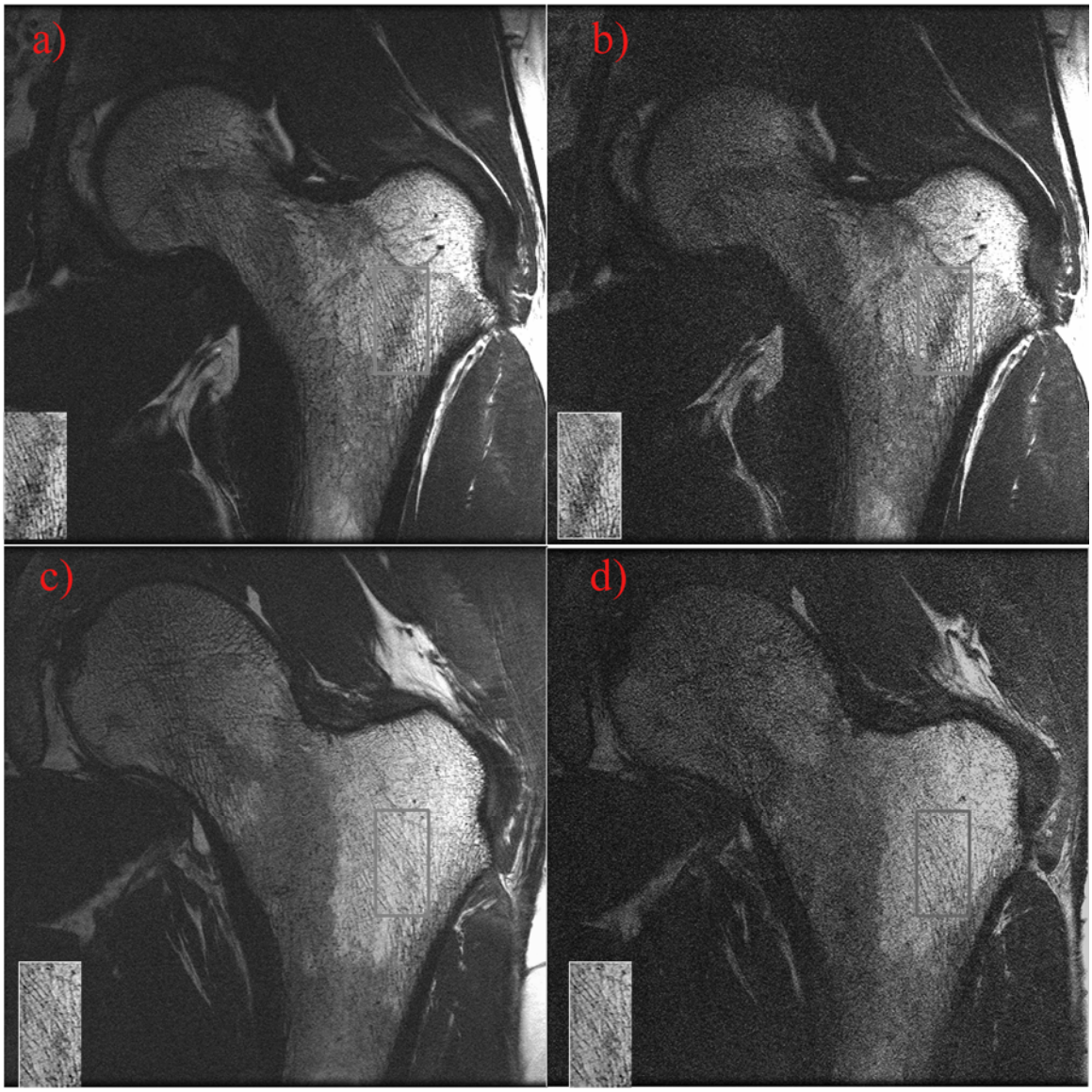

Fig. 4.10 a and b show representative R=1 and R=3 images of the hip for the shorter acquisition. Acquisition times were 7 minutes 26 seconds and 2 minutes 30 seconds respectively. Fig. 4.10 c and d show the R=1 and R=4 images of the hip for the longer acquisition. Acquisition times were 11 minutes 10 seconds and 2 minutes 52 seconds respectively. In both the accelerated images, trabecular depiction is better preserved in the trochanter, which is a high SNR region in the conventional image, than in the femoral head which is a low SNR region. A magnified view of the trabecular micro-structure in the femoral trochanter has been shown for each image.

Histogram plot of the pixel intensity distributions showed a decrease in peak height and broadening of the histogram with higher reduction factors that can be attributed to increased noise (Fig 4.11a). In some cases a leftward shift of the peak position was also noticed. The periodograms, projected along the PE axis showed very similar patterns for the regular and accelerated images. But at higher reductions, an increased energy was marked at higher frequencies, probably due to increased noise and at R=4 a slightly slower decay envelope was observed indicating a slight increase in the pixel intensity autocorrelation (Fig 4.11b). The plots in Figure 4.11 correspond to the same hip acquisition dataset as Figure 4.10c and 4.10d.

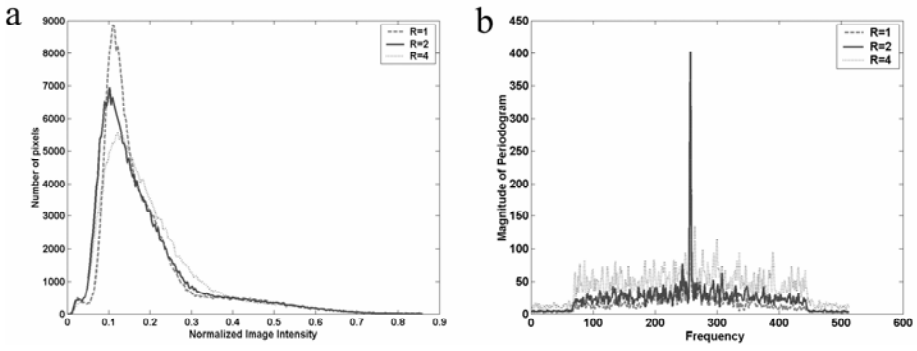

Fig. 4.11 a and b show the plot of the pixel intensity distribution and the 1D periodogram along the phase encoding direction respectively, of the R=1, R=2 and R=4 images from the longer acquisition at the hip. Reduction in peak height and broadening of the histogram with reduction factor is observed from Fig. 4.11 a. The periodogram plot shows similar patterns across reduction factors, but considerably increased energy at higher frequencies and slightly slower decay envelope is observed from the R=4 plot.

SNR Measurement

SNR measurements, using the two-repetition method for the two long acquisitions showed a 1.1-1.2 times decrease in SNR at R=2, 1.6-1.75 times SNR loss at R=3 and 2.1-2.4 times SNR loss at R=4 compared to R=1. In the SNR efficiency improvement experiment, SNR efficiency with R=2, N=3 and SOS combination increased by 21 %,

compared to N=2 R=1 acquisition for the shorter scan, and by 18% for the longer scan. This is in close agreement with the SNR efficiency improvement estimated on the basis of simulations.

Measurement of Trabecular Bone structural parameters

Measurements of the morphological metric showed an increasing trend in apparent trabecular number and bone fraction with reduction factor in the images acquired with PPI compared to the regular image. The apparent trabecular number measured from all the conventional and PPI acquisitions obtained with the FIESTA-C sequence is plotted in Figure 4.8. The least percentage change in the measure of App. TbN with increasing acceleration was found at the calcaneus. The mean increase was $2 \pm .05\%$ at R=2, $5 \pm 1\%$ at R=3 and $8 \pm 4\%$ at R=4. At the knee the shorter scans had a larger increase in App. TbN measures with reduction factor ($7.13 \pm .0004\%$ at R=2, $14.1 \pm 2.7\%$ at R=3 and $19.1 \pm 1.4\%$ at R=4) compared to the longer acquisition (1.75% at R=2, 5% at R=3 and 14% at R=4). The largest change in App. TbN measurements with reduction factor was marked at the site of the hip. The variation in the structural measurement with R at the longer acquisition (6% at R=2, 9 % at R=3 and 34 % at R=4) was less than that at the shorter acquisitions ($7.6 \pm 1.7\%$ at R=2, $14.8 \pm 1.3\%$ at R=3 and $41 \pm 11\%$ at R=4). So, while for the knee, the consistency of structural measurement with R improved considerably from the shorter to the longer acquisition, the improvement was smaller in the case of the hip. These initial studies indicate that the variation of structural measurement with R decreases with increasing image SNR, but a stronger statement regarding their relationship will need collection of more data points.

4.5 Discussion

This work applied PPI to HR-MRI of trabecular bone micro-architecture at 3 T. Initial results showed that depiction of the micro-structures was preserved till a reduction factor of 3 at the ankle and hip and at least till R=4 at the knee. PCA of the covariance matrix of the coil sensitivities indicate that 3-4 of the coil elements mostly contributed to the spatial encoding capability of the receiver system for the ankle and the hip experimental setups. The availability of receiver arrays more optimally customized to our imaging applications and the optimization of the experimental setup will increase the number of uncorrelated components, further improving the quality of the reconstructed images at higher acceleration. Employment of acceleration in both the phase-encoding and partition-encoding direction will allow higher net acceleration with less image degradation. Since HR-MRI of trabecular bone requires depiction of a network of micro-structures with dimension on the order of 100 microns, the application is very sensitive to differences in the PSFs of different reconstruction techniques. Qualitative comparison of the spatial resolution between conventional and accelerated images was performed in terms of edge sharpness and pixel intensity autocorrelation. From plots of the line profile and the periodogram, the spatial resolution seemed to have been closely preserved in these respects in the accelerated images, with only a slight smoothing of edges and slower decaying envelope at R=4. The line profile and periodogram plots also showed exaggerated edges and increased energy at higher frequency respectively, at higher R values, due to elevated noise. Measurement of the trabecular structural parameter, App. TbN showed an increasing trend with the reduction factor. This may be due to multiple reasons. As suggested from the longer and shorter acquisitions at the knee and the hip,

the variation in structural measurement might have a dependence on image SNR. However, it has been shown (4) that the structural measurements have a marked dependence on the SNR only when the image SNR is below a certain lower limit. The other factor to take note of is that the binarizing threshold level is chosen based on the reference intensity levels of the bone and the marrow. Increased bone reference intensity I_B due to local increase in noise will elevate the bone fraction and affect the binarization and the consequent structural measurements. So an image processing technique that is less sensitive to the background intensity (91) might be more appropriate in case of accelerated images. Additionally, because of the presence of data dependent coil weighting factors n in the PSF of the GRAPPA reconstruction, the effective image resolution will also be sensitive to object placement within the coil, relative angulations of the imaging plane etc. So for consistency in structural measurements, standardization of the imaging arrangement is crucial. The higher degree of variability in the structural measurements at the hip might again be due to a combination of factors. The femoral trochanter has the highest degree of trabecular structural anisotropy and heterogeneity among the three skeletal sites, which makes it more sensitive to noise variations in the image. Also, the plots of normalized eigenvalues obtained by PCA of the covariance matrix of coil sensitivities (Fig. 4.7) showed the lowest eignevalues between R=1 and 3 for the case of the hip which implies inferior encoding capability of the receiver setup at the hip at lower reduction factors compared to the ankle and knee setups. More in-depth investigation into accurate quantification of trabecular structural measurements from accelerated images will be conducted in the future for larger sample size and each of the probable causes of the variation in measurement with R will be examined separately.

Previously Weiger et al demonstrated the use of SENSE for enhancing the SNR efficiency of SS-GRE sequences (92). This work demonstrated how the PPI technique can be used to improve the SNR efficiency of multiple acquisition b-SSFP protocols. Employing PPI with R=2, we were able to accommodate 3 phase-cycled acquisitions in shorter scan time than a full FOV N=2 acquisition. Also, with N>2, we were able to avail of the SNR advantage of the SOS combination.

The anomaly in SNR measurements due to spatially varying noise distribution in images obtained from PPI have been discussed in the literature (52). The two repetition method employed for SNR computations in this work is not only time consuming but also error-prone in case of high resolution images. ROI misalignment arising from patient motion even in the order of a pixel in between the two acquisitions can cause gross overestimation of the noise variance. An alternative is to compute the SNR in a PPI image on a pixel-by-pixel basis using a g-factor map.

4.6 Conclusion

This study showed the feasibility of employing PPI to *in vivo* HR-MRI of trabecular bone at 3 T using several evaluation techniques. PPI images showed good structural detail, although strategies for accurate measurement of the trabecular bone structural parameters will have to be further investigated. Currently *in vivo* HR-MRI acquisition of trabecular bone takes around 15-20 minutes. The long acquisition time causes patient discomfort and motion-induced artifacts. By accelerating acquisition, PPI can enhance the clinical feasibility of HR-MRI for monitoring changes in the trabecular micro-architecture *in vivo*. For a given scan time, PPI also allows more flexibility in protocol design. This work

showed one such possibility by designing a more SNR-efficient multiple acquisition b-SSFP protocol. The scan time saved by PPI can also be used to improve through-plane coverage, or if SNR permits, to acquire at isotropic voxel resolution while maintaining through-plane coverage. The synergy between high field and PPI can substantially benefit research applications of trabecular bone MRI. With enough SNR to spare at higher field strengths (> 3 T), it might be possible to employ PPI to image at true microscopic resolution in a reasonable time.

Chapter 5

Adaptation of Parallel imaging for musculoskeletal applications at 7 Tesla

5.1 Introduction

Translation of MRI applications to higher magnetic field strength is primarily motivated by the need to improve signalSNR. We previously observed a significant SNR gain for trabecular bone imaging at 3 T compared to 1.5 T (12). Over the past five years, several musculoskeletal studies ventured to the higher field strength of 3 T from the clinical standard field strength (1.5 T) (93-95). The improved correlation of MR derived structural parameters with micro-CT, a standard of reference was reported for trabecular bone applications at 3 T (91). Higher SNR and CNR allowed imaging at higher spatial resolution and improved lesion detetctibility in cartilage imaging at 3 T compared to 1.5 T (96,97). Imaging at an even higher field can allow improved in-plane resolution, isotropic voxel resolution in 3D imaging, and *in vivo* musculoskeletal MR imaging techniques that have till now been SNR-limited. Ultra high field MRI for humans has gained prevalence in recent years and a whole body 7 Tesla (T) magnet has become available to our research group. Initial research experience in trabecular bone and cartilage imaging has shown potential for MRI of osteoporosis and osteoarthritis at 7 T (14,98,99). However a serious disadvantage of ultra-high field imaging of humans is high radiofrequency (RF) power deposition in the subject. So employment of parallel imaging

at 7 T is crucial not only for reducing scan time but also for reducing total RF power deposition during a scan (100).

The purpose of this work is to implement Generalized Autocalibrating Partially Parallel Acquisition (GRAPPA) (74) pMRI for *in vivo* high resolution (HR) imaging of cartilage and trabecular bone micro-architecture at 7 T and to ascertain whether the parallel imaging (PI) method can be adapted to the high field without any modifications in the calibration or reconstruction strategy. To this end, the performance of the PI technique at 7 T was evaluated by several approaches such as comparison of MR derived bone and cartilage morphology metrics that are considered as biomarkers in osteoporosis and osteoarthritis, between accelerated and R=1 images; and comparison of geometry factor measures between 3 T and 7 T. Trabecular bone micro-architecture at the ankle was imaged employing R=1-6 and 4x2 with an eight channel head array. Due to very limited commercial availability of array coils for musculoskeletal applications at 7 T, we attempted pMRI of cartilage and bone structure at the knee with a two-channel quadrature coil. Hence this paper also evaluates the feasibility of conducting PI with a quadrature coil based on comparison of image quality and morphology measurements between accelerated and R=1 image obtained using this coil. Knee cartilage was imaged with fat saturated spoiled gradient recalled echo (fs-SPGR) and multiple phase-cycled fully balanced steady state free precession (m-bSSFP) (49) sequence, bone was imaged with the latter sequence as well. SSFP sequences are highly SNR efficient and can provide additional contrast between cartilage and muscle, compared to SPGR. However, in this work the m-bSSFP sequence was employed in cartilage imaging primarily to investigate if the incorporation of multiple phase cycled observations of m-bSSFP from

each receiver as additional reconstruction bases (101) improved image reconstruction in case of PI with the quadrature coil.

5.2 Complementary nature of high field and parallel imaging

High-field and parallel MRI have been the two main foci of MR development in recent years. Although these are two independent developments, the two applications are mutually benefiting to each other. Translation to higher magnetic field strength is motivated by increased spin polarization but is also fraught with technical challenges such as higher radiofrequency (RF) power deposition in the subject and larger susceptibility effects, to mention a few. RF energy deposition in tissue is approximately proportional to square of the Larmor frequency, or equivalently, the square of B0 [Ref]. This raises serious safety concerns at high field. Consequently, safety guidelines for specific absorption rate (SAR), which measures RF energy induced heating in the subject, can impose severe restrictions on MR sequence design at field strengths such as 7 T. Susceptibility differences between magnetically heterogeneous environments scale linearly with the field strength. (41). This results in greater static dephasing induced signal loss and shorter T2* decay for gradient echo imaging, larger distortions in EPI and spiral scans and banding artifacts in bSSFP acquisitions at higher field unless very effective higher order shimming routines are employed to minimize B0 inhomogeneity. So high field offers higher intrinsic SNR but suffers from limitations such as higher RF power deposition and B_0 inhomogeneity. In contrast, partially parallel imaging can reduce SAR and B_0 inhomogeneity (incase of EPI sequences) at the expense of SNR. So the strengths and weaknesses of high field and PPI are complementary. But the synergy

between high field and PPI that has been widely discussed in literature arises from more intrinsic changes in RF electrodynamics at higher field.

RF wavelength and skin depth in the object gets shorter with increasing field strength, generating a more spatially complex B_1 field. Although the larger B_1 inhomogeneity poses problems with uniformity of transmit profile and sensitivity calibration, it also results in more distinct coil sensitivities, enhancing the spatial encoding capability of the coil array (100,102). Till date, parallel imaging performance as a function of field strength has been evaluated based on theoretical electrodynamics and experimental studies mainly for brain imaging applications (103,104). But the performance is specific to tissue type and object dimensions. In this work we will evaluate parallel imaging performance at 7 T by comparison with 3 T for small field-of-view trabecular bone and cartilage imaging applications.

5.3 Materials and Methods

5.3.1 MR Experiments

MR experiments were conducted on seven healthy human subjects on a 7 T General Electric (GE) MR scanner (EXCITE, WI, USA) in accordance with the regulations of the Committee of Human Research (CHR) at our institution. Three volunteers were imaged at the knee (distal femur) with the above-mentioned transmit/receive quadrature coil (Nova Medical, MA, USA) with two elements. Since the two elements are connected to two separate receiver chains, parallel imaging could be performed with this coil. Image datasets of knee cartilage comprising of 32 slices were acquired in the sagittal plane with in-plane/through-plane resolution of 0.237 (mm)/1.5 mm. A modified three dimensional (3D) fat suppressed Spoiled Gradient Recalled (fs-SPGR) sequence was employed with TR(ms)/ TE(ms)/ BW(KHz)/ flip(°) = 17.1/ 3.7/ 64 / 18 over a scan time of 6 minutes 45 seconds in the absence of acceleration and 3 minutes 35 seconds with R=2. The knee cartilage in two volunteers was imaged with the m-bSSFP sequence (13,15), 3D cycled Fast Imaging Employing Steady State Acquisition (FIESTA-c) employing two phase cycles, TR(ms)/ TE(ms)/ BW(KHz)/ flip(°) = 7.3/ 2.1/ 42/ 15 and identical imaging resolution as above. Duration of the fully gradient encoded and R=2 acquisitions were 3 minutes 55 seconds and 2 minutes 8 seconds respectively. Phase-encoding lines acquired in different phase-cycles were also offset with respect to each other.

Trabecular bone micro-architecture at the knee (distal femur) was imaged in the axial plane with the m-bSSFP sequence with two phase cycles, partial echo, TR(ms)/ TE(ms)/ BW(KHz) of 13.9/ 2.9/ 32 and a flip angle of 40°. In-plane/ through plane resolution was

0.156/ 0.5 mm. Scan time for R=2 acquisition was 8 minutes 22 seconds for a 52 slice dataset. In the interest of time, the corresponding unaccelerated scan was not performed. Trabecular bone structure at the ankle (calcaneus) was imaged in the sagittal plane in four normal, healthy subjects with an eight channel head array coil (Nova Medical, MA, USA) with a similar m-bSSFP protocol of TR(ms)/ TE(ms)/ BW(KHz)/ flip(°) = 10.7/ 2.6/ 32/ 40. In-plane /through plane resolution was 0.195/ 0.5 mm and duration of the unaccelerated scan was 9:19 minutes for a 32 slice dataset. Scan time for R=2, 3, 4, 5, 6 acquisitions was 4 minutes 51 seconds, 3 minutes 20 seconds, 2 minutes 35 seconds, 2 minutes 4 seconds and 1 minute 52 seconds respectively. A 2D accelerated acquisition of R=4 (phase encode) x 2(partition encode) was also employed. Ankle scans of three normal, healthy subjects acquired for a previous study (16) at 3 T with identical resolution, comparable m-bSSFP protocol (TR(ms)/ TE(ms)/ BW(KHz)/ flip(°) = 10.7/ 2.6/ 32/ 60) and an eight channel head array were also considered for some of the image analyses to be described later. All accelerated acquisitions with SPGR and FIESTA-c sequences were employed with Cartesian variable density acquisition and 12-24 autocalibration (AC) lines. In the 2D accelerated acquisition, 4 AC lines were collected in the partition encode direction.

5.3.2 Image Reconstruction

Datasets from the accelerated acquisitions were reconstructed offline on a Sun Workstation with a customized GRAPPA-based parallel reconstruction algorithm developed in our laboratory (13) in MATLAB (The Mathworks, Inc. Natick, MA, USA). At 3 T, the optimal GRAPPA reconstruction kernel was previously found to be 4x3

(13,85). A kernel size of 4x3 implies that 4 neighboring data points along the axis of acceleration and 3 neighboring data points along the other axis are used to synthesize each missing data point. Since we expect larger inhomogeneity of the B1 field at 7 T compared to 3 T, a smaller kernel might be sufficient for the GRAPPA reconstruction at 7 T, leading to better conditioned matrix inversion and faster reconstruction speed. Therefore we compared reconstruction quality obtained with a 2x3 GRAPPA kernel to the 4x3 kernel in the 4 ankle acquisition datasets for R=2 and 4, on the basis of artifact power. Artifact power for an image was calculated as

$$AP_p = \sqrt{\frac{\sum_{j=1}^{N}(I_{REF}(j) - I_p(j)^2}{\sum_{j=1}^{N} I_{REF}(j)^2}} \qquad [5.1]$$

where I(j) represents intensity in pixel j of image p and I_{REF} represents the intensity in the corresponding R=1 image. In case of the 2D accelerated ankle acquisitions, two successive 1D GRAPPA-based reconstructions were performed along the phase-encoding and partition encoding axes. A homodyne reconstruction was applied along the frequency-encode direction to all partial echo acquisition datasets.

Previously, extending the superresolution principle to the super-FOV (sFOV) method, full FOV images have been reconstructed from undersampled m-bSSFP acquisition, using data from each phase-cycled acquisition as a reconstruction basis. (101). To examine if combining sFOV with GRAPPA method yielded better image reconstruction than GRAPPA alone, sFOV-GRAPPA methods were additionally employed for the cartilage m-bSSFP experiments. Phase-encoding steps were offset between phase-cycles during acquisition and undersampled datasets from different

receivers as well as from different phase-cycled acquisitions were used as reconstruction bases.

5.3.3 Image Analysis

Measurement of g-factor

The relative noise enhancement factor, g-factor, in a pixel of an individual coil image was computed as the square root of the sum of the magnitudes of the Fourier transform of the GRAPPA reconstruction weights for that pixel (76). The composite g-factor was computed by the same weighted sum-of-squares combination used for combining the array images. The net g factor for 2D acceleration can be derived by expressing the 2D GRAPPA reconstruction as 2 successive convolution operations:

$$\begin{aligned} S_j(ky+\Delta ky, kz+\Delta kz) &= \sum_l n_{y_l}(ky,kz) \otimes S_l(ky, kz+\Delta kz) \\ &= \sum_l n_{y_l}(ky,kz) \otimes \sum_{l'} n_{zl'}(ky,kz) \otimes S_{l'}(ky,kz) \end{aligned} \quad [5.2]$$

where n_{y_l} and $n_{z_{l'}}$ are the GRAPPA filters for the 2 1D reconstructions along ky and kz axes respectively and l,l' are coil indices.

On applying Fourier Transform to both sides of the equation,

$$I_{jFULL}(y,z) = \sum_l N_{y_l} \sum_{l'} N_{z_{l'}} I_{l'RED}(y,z) \quad [5.3]$$

I_{jFULL} and I_{jRED} represent the full-field-of-view (FOV) and aliased images from the jth coil. N_{yl} and $N_{zl'}$ are the Fourier Transforms of the GRAPPA reconstruction filters n_{yl} and $n_{zl'}$ respectively. From [5.3], the composite g-factor in a pixel in case of 2D

accelerated acquisition can be computed as the product of the g-factors resulting from the two 1D accelerations.

The mean g-factor map for a dataset was computed by averaging the g-factor values for each pixel over five centrally located slices. Mean g-values computed from ankle datasets at 7 T were compared to those at 3 T and their differences were tested for statistical significance by Mann Whitney Ranksum test.

Since cartilage thickness and trabecular bone structural parameters are morphology metrics, ideally, all acquisitions obtained from the same subject should yield identical measurements of these parameters, irrespective of the imaging technique. However the quantitative analysis is quite sensitive to the imaging method. For this reason, we derived some of these metrics from the images and investigated the deviations in the measurement values between PI and R=1 datasets. The measurement differences were also tested for statistical significance by Mann Whitney Ranksum test.

Cartilage Analysis

The analysis of knee cartilage from SPGR and FIESTA-c images consisted of a semi-automatic segmentation technique based on Bezier splines and edge detection and a distance field based shape interpolation as previously described in (105). Each point on the articular surface was assigned a thickness value equal to its distance from the closest point on the bone-cartilage interface. Mean 3D cartilage thickness and cartilage volume measures from each subject were compared between R=1 and R=2 datasets.

Trabecular Bone structural analysis

Trabecular bone structural measures were derived from the ankle acquisitions. Five slices were considered from each image-set for the quantitative analysis, after demodulating images of coil sensitivity variations (30). Regions of interest (ROIs) were manually placed in the trabecular bone of the posterior calcaneus in an identical location on all corresponding images and binarized into bone and marrow phases by a dual threshold method (32). As in the previous chapter, so we chose to compare the structural measure App. TbN between unaccelerated and PI datasets.

5.4 Results

5.4.1 Image Reconstruction kernel

The 4x3 reconstruction kernel provided better image quality and yielded 217.50 % and 170.47 % lower artifact power for R=2 and R=4 respectively than the 2x3 reconstruction kernel. Therefore we used the 4x3 kernel for reconstruction of all undersampled data.

.

5.4.2 Image quality and morphology measurements

Knee Imaging

Parallel imaging with R=2 could be successfully employed with the quadrature coil. Low resolution, low pass filtered sagittal images of the knee obtained from the two individual channels of the quadrature coil are shown in Figures 5.1a and b. High image intensities indicate regions of high coil sensitivity. Images from m-bSSFP acquisitions at the knee are shown in Figure 5.2. Figure 5.2a shows good visualization of trabecular bone micro-

architecture. m-bSSFP images of the knee cartilage for R=1 (Fig. 5.2b), R=2 GRAPPA (Fig. 5.2c) and R=2 sFOV-GRAPPA (Fig. 5.2d) had comparable tissue contrast and similar edge sharpness. However normalized difference image (NDI) between R=2 sFOV-GRAPPA and R=1 (Fig. 5.2f) appears sparser than the NDI between R=2 GRAPPA and R=1 (Fig. 5.2e).

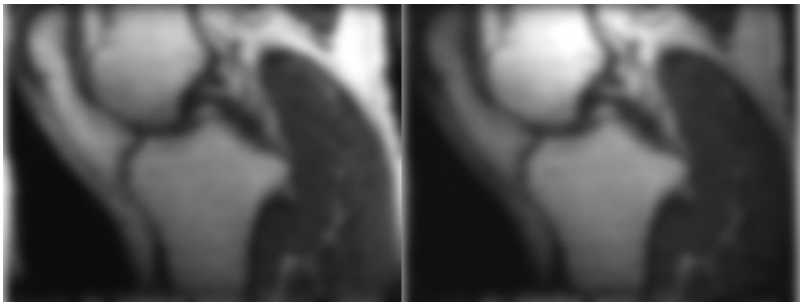

Figure 5.1 Figure 5.1a and b show low resolution images of the knee in the sagittal plane obtained from the two individual channels of the quadrature knee coil. High image intensities indicate regions of high coil sensitivity and it can be seen from Figure 5.1 that sensitivity profiles of the two coil elements have some spatial overlap.

Mean cartilage thickness/volume measures from R=2 sFOV-GRAPPA images also had lower differences (3.98 %/ 8 %) compared to R=2 GRAPPA (10.25 %/ 17 %) from the unaccelerated images. Two fold acceleration with the SPGR sequence (Fig. 5.3b) yielded excellent image quality and comparable femoral and tibial cartilage delineation to the R=1 acquisition (Fig. 5.3a). The 3D thickness maps computed from the R=1 and R=2 datasets had similar patterns (Fig. 5.3c and 5.3d). Mean 3D thickness and volume measures also matched closely between the two groups (Table 5.1) and were not statistically significantly different ($p < .05$).

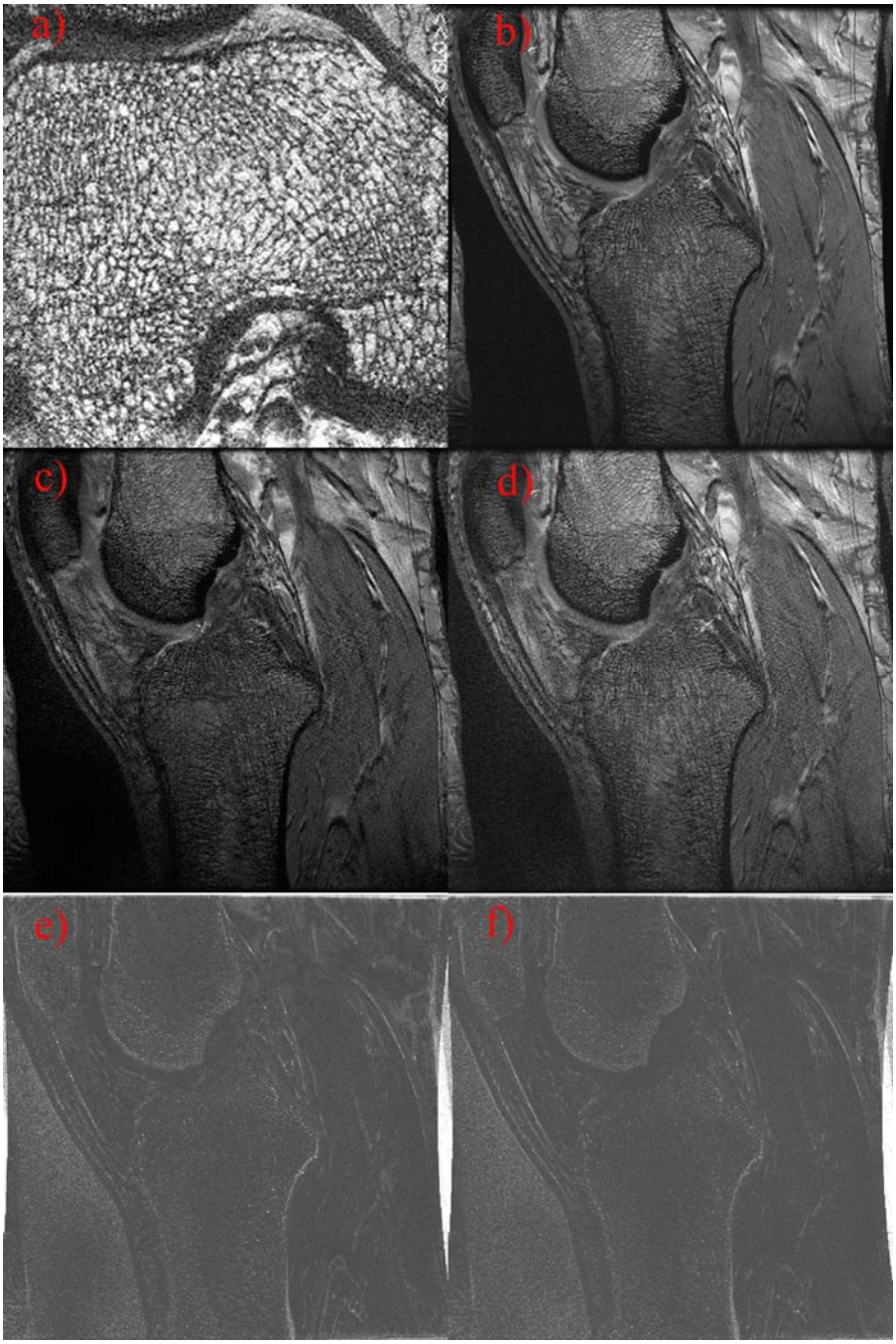

Figure 5.2 shows images from m-bSSFP acquisitions at the knee obtained with the quadrature coil. Fig. a is a two-fold accelerated image of trabecular bone at the knee with in-plane/ through-plane resolution of 156/ 500 μm. Fig. 5.2b,c and d are representative unaccelerated, R=2 GRAPPA, R=2 sFOV-GRAPPA images of the knee cartilage respectively. Normalized difference between R=2 GRAPPA (Fig. c) and R=1 (Fig. 2b) is shown in Fig. e and that between R=2 sFOV-GRAPPA (Fig. d) and R=1 is shown in Fig. f. Visually Fig b-d have similar image contrast and edge sharpness but the

difference image of R=2 sFOV-GRAPPA appears more uniform than that of R=2 GRAPPA.

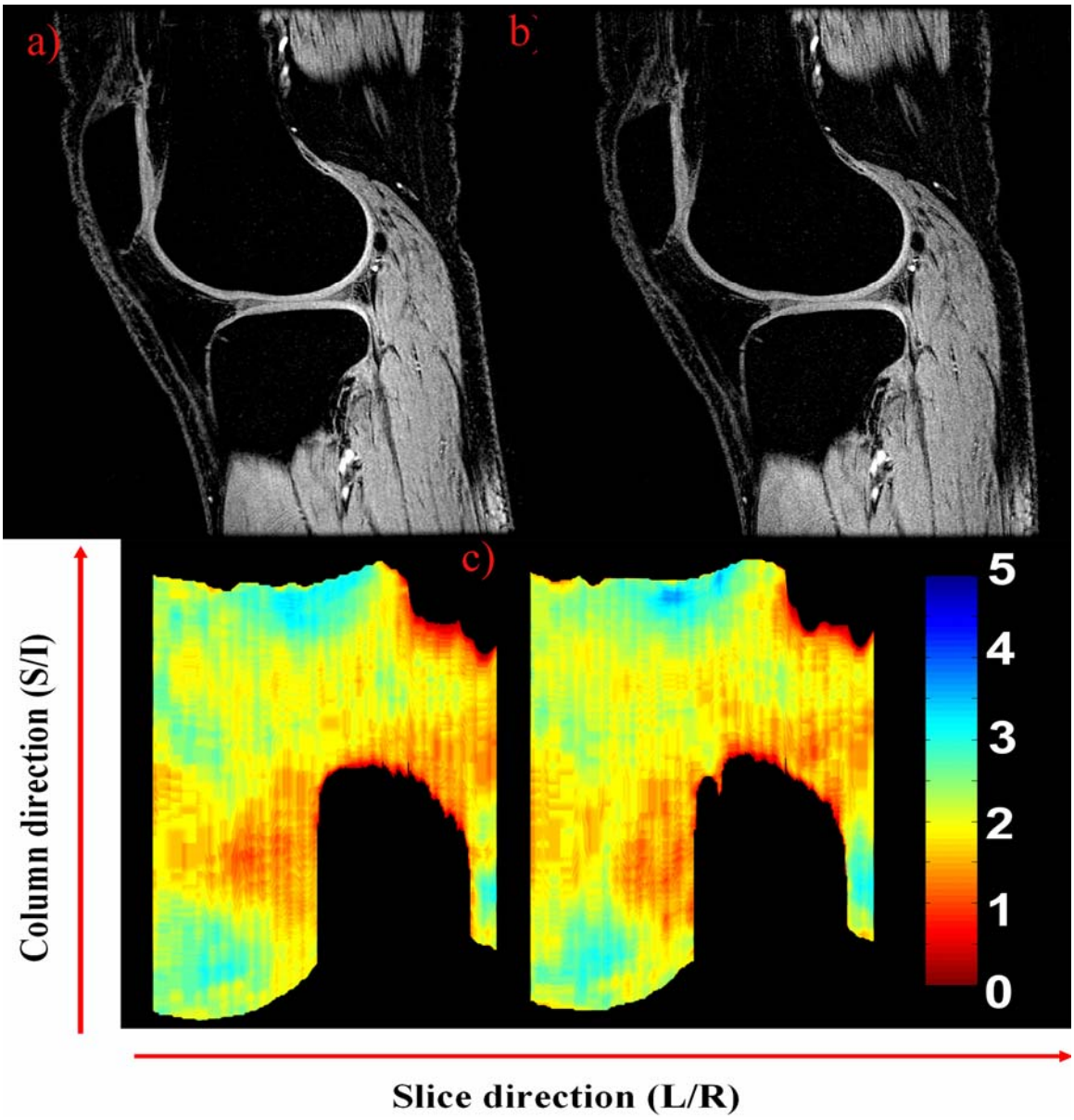

Figure 5.3a and 5.3b are representative SPGR images of the knee cartilage acquired with no acceleration (R=1) and 2 fold acceleration (R=2) respectively. Figures c and d are the 3D thickness maps of these R=1 and R=2 datasets. The R=2 image has excellent image quality and cartilage delineation, comparable to R=1. The thickness maps are also very similar, although there are some local differences.

Table 5.1. Mean 3D cartilage thickness and volume measured from R=1 and R=2 SPGR images of the knee

	Mean Thickness (mm)		*Volume (mm^3)*	
	R=1	**R=2**	**R=1**	**R=2**
S1	*2.01±.60*	*2.04±.64*	*6.08*	*5.65*
S2	*1.96±.54*	*1.95±.54*	*6.25*	*6.24*
S3	*2.11±.72*	*2.14±.71*	*5.75*	*6.09*

Table 1 shows mean ± 1 SD of 3D cartilage thickness and total cartilage volume measures obtained from R=1 and R=2 SPGR datasets. The measurements did not have a statistically significant difference ($p < .05$) between the two groups and agreed closely.
S*: Subject*

Ankle Imaging

HR-MRI of trabecular bone at the calcaneus could be accelerated up to 6 fold, with slight image degradation at R=6. Figure 5.4a shows a representative unaccelerated image of trabecular bone at the calcaneus. As expected, the 2D 4x2 acceleration (Fig. 5.4d) yielded better image quality than the 1D R=6 acceleration (Fig. 5.4c) , although measurement time was nearly equal for the two acquisitions. Image quality and visualization of trabecular bone structure is comparable in the R=4 (Fig. 5.4b) and R=4x2 (Fig. 5.4d) acquisitions although the scan time is much shorter for the latter (1 minute 52 seconds) than the former (2 minutes 35 seconds). App. TbN values showed an increasing trend with R in accelerated images compared to R=1 which is consistent with our observations in a previous study at 3 T (16). The overestimation is probably due to spatially varying noise amplification and changes in histogram characteristics (23). The mean increase in App. TbN value at R=3, 4 and 4x2 compared to the unaccelerated acquisition was 4.48 ± 2.12 %, 6.79 ± 4.6% and 6.98 ± 2.89% respectively. The consistency of measurement at a

high acceleration of R=4x2 again demonstrates the benefits of 2D acceleration. The App. TbN values were not statistically significantly different between accelerated and conventional images for any acceleration factor ($p<.05$).

5.4.3 Measurement of g-factor

Mean g-factors measured from the ankle scans for R=2-6 and 4x2 are shown in Fig. 5.5a. We also measured g-factors from similar MR scans of trabecular bone at the ankle previously acquired at 3 T. The g values measures were similar between the 2 field strengths at R=3, but lower at 7 T for higher accelerations (Fig. 5.5b), although the differences were not statistically significant ($p < .05$).

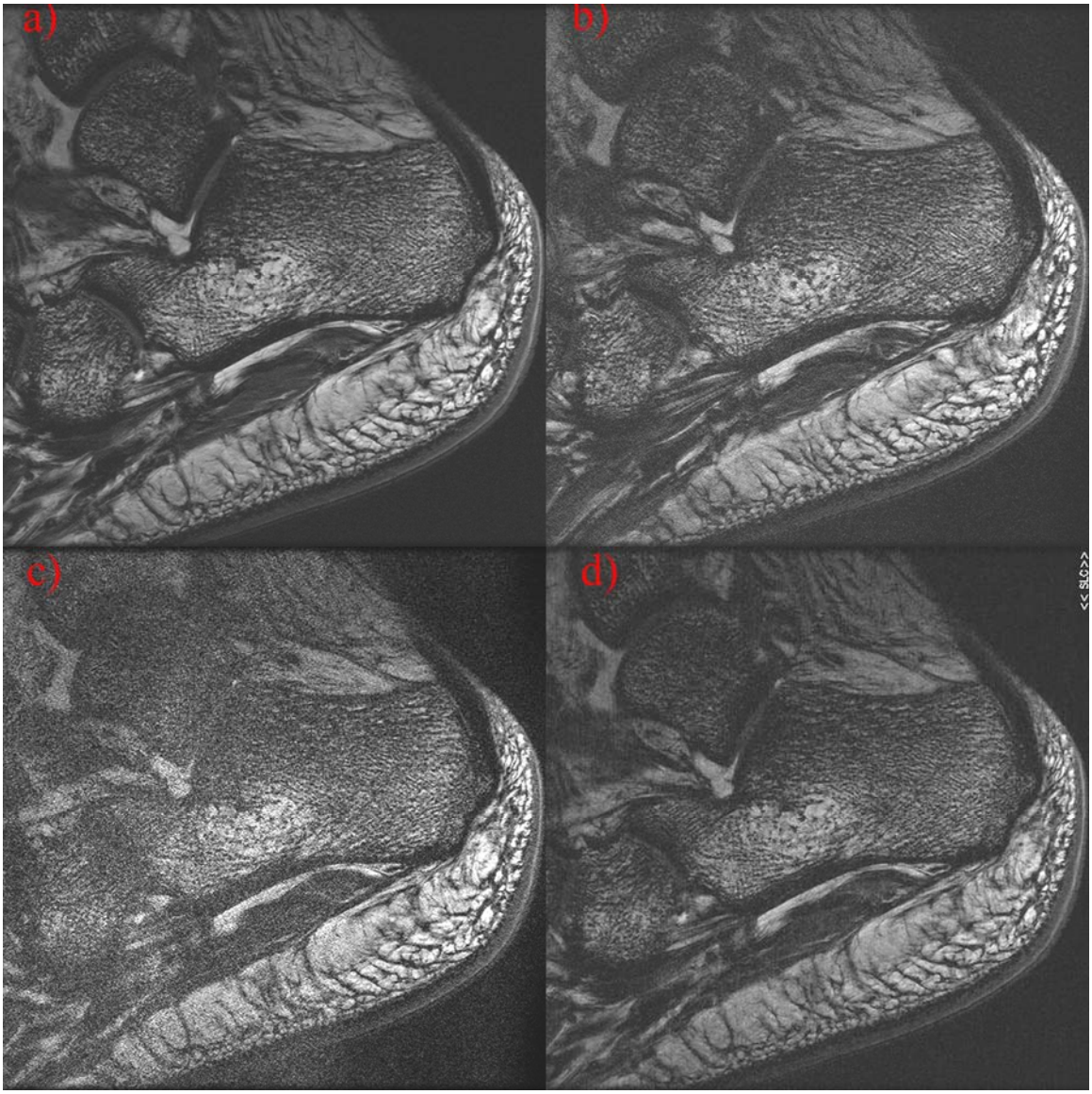

Figures 5.4a, b, c and d are representative R=1, R=4, R=6 and R=4x2 images of the trabecular bone micro-architecture at the ankle acquired with the m-bSSFP sequence and the eight channel head array. Figures 4e, f and g are images of the normalized difference of R=4, R=6 and R=4x2 respectively from R=1. As expected, the 2D 4x2 acceleration (Fig. 4d) yielded better image quality than the 1D R=6 acceleration (Fig. 4c), although they had nearly equal scan times.

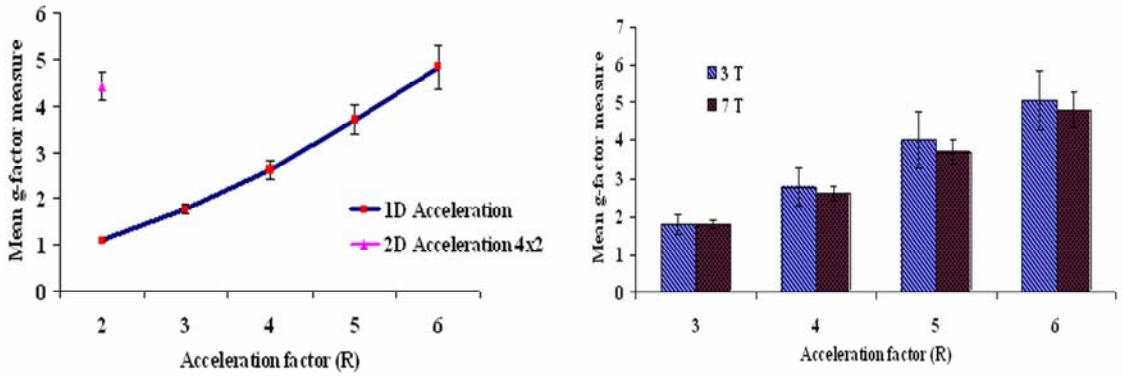

Figure 5.5 shows plots of g-factor measures. Mean g-factors measured from the ankle scans for R=2-6 and 4x2 at 7 T are shown in Fig. a. The standard deviation of the measurement is seen to increase with the acceleration factor. Fig. b is a comparative plot of the g-factor values measured from 3 T and 7 T. The g values are similar at R=3, but considerably lower at 7 T for R>=4. However the measures were not statistically significantly different between the two field strengths.

5.5 Discussion

Differences in the performance of pMRI between two field strengths arise mainly due to variations in RF homogeneity within the imaging volume. Based on its conductivity and permitivitty properties, spatial inhomogeneity of the B_1 field in the bone marrow is expected to increase by a small extent from 3 T to 7 T (3,24). This is in conformance with our observations of the unsuitability of a smaller reconstruction kernel; and lower (but not statistically significantly different) geometry factors, a higher feasible acceleration factor of R=6 and slightly smaller differences in the trabecular bone structural measure, App. TbN between accelerated and R=1 images, at 7 T compared to 3 T (16). However, it should be noted that the head array at 7 T had a smaller diameter compared to 3 T, rendering it less suitable for ankle imaging. Spatial complexity of the B_1 field can be

expected to increase considerably within the imaging FOV at 7 T for the cartilage application (3,24). However, in the absence of a comparable dual channel quadrature coil setup at 3 T, comparisons could not be drawn between the two field strengths for this application.

The imaging protocols used in this work are based on optimization studies for 7 T previously conducted in our lab (10,11). Since this work is primarily a feasibility study, imaging a larger cohort of healthy subjects or patient population was considered to be beyond its scope. The m-bSSFP sequence was employed for cartilage imaging primarily to investigate the benefits of the sFOV-GRAPPA method. Comparison of SPGR and m-bSSFP sequences for morphology measurement and lesion detectibility is the focus of a separate study being conducted in our research group.

5.6 Conclusion

To conclude, we implemented and evaluated PI for in vivo HR-MRI of trabecular bone and cartilage at 7 T. To the best of our knowledge, this was the first time in vivo measurement of g-factors was presented for musculoskeletal tissues at 7 T. The advantage of 2D over 1D acceleration and the feasibility of conducting PI with a dual channel quadrature coil were also demonstrated. The clinical feasibility of in vivo HR musculoskeletal MRI at 7 T can increase considerably with employment of parallel imaging, because of reduced RF power deposition and the potential flexibility in protocol design.

Chapter 6

Robust quantification of bone structural measurements from GRAPPA reconstructed images

---

6.1 Motivation

The end goal of quantitative high resolution MRI of trabecular bone is to be able to evaluate osteoporotic condition by quantifying structural parameters of trabecular bone network. In Chapter 4, it was seen that the bone fraction (App. BV/TV) and bone structural parameters such as App. TbN are overestimated from pMRI images and there is an increasing trend in the measurement with acceleration factor R (13). In this work we will investigate the possible causes of this overestimation and propose image reconstruction and image processing techniques that will improve the accuracy of the bone morphology metrics measurement from images obtained by GRAPPA based parallel imaging methods.

The image processing technique employed to measure trabecular bone structural parameters from MR images involves a dual threshold method. The bone intensity reference or lower threshold I_B is determined by sampling the cortical bone shell in different locations in the image and I_M, the marrow reference intensity level or higher threshold is set to the higher value of the full-width-at half-maximum (FWHM) of the intensity histogram of the region of interest (ROI). Structural analysis is subsequently

performed on binarized bone images by edge based mean intercept length method (32). This has been described in detail in Section 2.2. So the App. TbN measure would increase if more edges are encountered in the MIL method and/ or if the binarized image generated by the dual-threshold has an increased bone fraction (BF).

A factor of $\sqrt{R}$ SNR loss in a pMRI image compared to fully gradient encoded image is due to fewer number of k-space samples acquired in the pMRI acquisition. There is an additional spatially varying SNR degradation factor g in the accelerated image, related to the geometry factor (64,76). So if the accuracy of structural measurements is SNR dependent, it would deteriorate in case of pMRI image-sets. However, it has been seen that for image SNR ~> 10, measurement accuracy is only weakly SNR dependent (4). In this work we hypothesize that elevation of App. TbN measures in accelerated images is caused primarily by the spatially varying amplification of noise in the reconstructed image. There are two main sources of this noise amplification. As already mentioned, the first is related to the geometry factor (64,76). Noise from this source can be minimized by using optimal coil array for signal detection and by optimizing the relative positioning of the imaging volume within the coil array. The g-factor value has also been observed to decrease with increasing static magnetic field strength (Section 5.2) (102-104). The second source is the inverse computation associated with solving for reconstruction filter coefficients. Spatially varying noise amplification caused by the second source can be mitigated to some extent by regularizing the inversion of the signal matrix in the GRAPPA reconstruction (106-108). We also hypothesize that in view of the altered histogram characteristics of a highly accelerated image compared to the conventional R=1 image (Chapter 4) (13), the

empirically set upper threshold might not be appropriate and might yield elevated bone fraction (BF) measures. Since all structural analysis is performed on binarized bone images, the elevation of BF would affect all the structural measurements. The second probable cause of variation in structural measurements might be addressed by a histogram transformation strategy.

6.2 Regularization of Inverse Problems

The basic equation for computation of GRAPPA reconstruction weights, previously presented in Chapter 4 (Equation 4.4) can be written as

$$\mathbf{S}_{\mathbf{src}}.\mathbf{n}_{\mathbf{j,m}} = \mathbf{S}_{\mathbf{tgt}_{\mathbf{j,m}}};\quad \mathbf{S}_{\mathbf{src}} = \left\lfloor \mathbf{S}_{\mathbf{src}_1} \ldots\ldots \mathbf{S}_{\mathbf{src}_K} \right\rfloor \qquad [6.1]$$

where j is the coil index, m is the number of Δky offsets between source and training lines and K is the number of coils. If N_b blocks are used for the reconstruction and N_x is the dimension in k_x, then S_{srci} has a matrix size of (N_x x N_b). For convenience of notation this equation can be written as

$$\mathbf{Ax} = \mathbf{b} \qquad [6.2a]$$

and can be solved for x by computing the pseudoinverse of **A**. A useful numerical tool for analysis of the ill-posedness of inverse problems is the singular value decomposition (107)

If $A \in \Re^{mxn}$ be a rectangular matrix with $m \geq n$ (as in our case), its SVD can be written as

$$\mathbf{A} = \mathbf{U\Sigma V}^T = \sum_{i=1}^{n} u_i \sigma_i v_i^T \qquad [6.2b]$$

such that U and V are matrices with orthonormal columns and $\Sigma=\text{diag}(\sigma_{1,\ldots}\ \sigma_n)$ has non negative diagonal elements appearing in decreasing order.

As σ_i decreases, singular vectors u_i and v_i tend to have more sign changes i.e. they become more oscillatory. From equations [6.2a] and [6.2b], we can write

$$\mathbf{x} = \left(\mathbf{V}\boldsymbol{\Sigma}^{-1}\mathbf{U}^{T}\right)\mathbf{b} \qquad [6.2c]$$

With increasing order i, σ_i decreases and $\frac{1}{\sigma_i}$ increases, amplifying the high frequency oscillations in b. This is the basis of the ill-posedness of inverse problems (107,108) .

In our specific case, the ill-posedness would lead to higher frequency oscillations in the k-space data synthesized by filter coefficients **n** from the acquired data, and more edges in the reconstructed image.

One obvious way of to alleviate the problem is the truncated SVD which discards the nearly singular eigenvalues of the SVD.

$$A = \sum_{i=1}^{p} u_i \sigma_i v_i^{T}; \qquad p \prec n \qquad [6.2d]$$

However the most common and well known form of regularization is the Tikhonov regularization. The idea behind it is to define the regularized solution x_λ as the minimizer of the weighted combination of the residual norm and a constraint (106-108)

$$\mathbf{x}_\lambda = \arg\min\left\{\left\|\mathbf{A}\mathbf{x}-\mathbf{b}\right\|^2{}_2 + \lambda^2\left\|\mathbf{L}(\mathbf{x}-\mathbf{x}^*)\right\|^2{}_2\right\} \qquad [6.3]$$

The regularization parameter λ controls the weight given to minimization of the constraint relative to the minimization of the residual norm. L is usually the identity matrix or a derivative operator, $\mathbf{x}^*$ is an initial estimate of **x** that may be included in the constraint. One graphical tool for choice of the regularization parameter is the L-curve

method. It is a plot of the norm $\|\mathbf{Lx}\|_2$ versus the residual norm $\|\mathbf{Ax}-\mathbf{b}\|_2$ in the log-log scale. Discrete ill posed problems usually have a characteristic L shaped appearance in such a plot-hence the name of the curve. The vertical part of the curve represents the under-regularized regime in which $\|\mathbf{Lx}_{\text{reg}}\|_2$ is very sensitive to changes in the regularization parameter and the horizontal part represents the over-regularized regime in which the residual norm is more sensitive to changes in λ (106-108) (Fig 6.1). The optimal trade-off is given by the point of maximum curvature or the "corner" of the L curve. The Tikhonov regularization is said to be optimal because it produces the least residual and semi norm compared to other SVD methods (108).

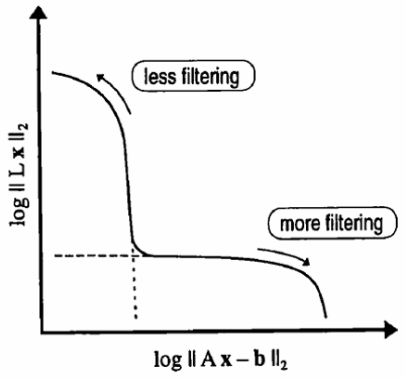

Figure 6.1 shows the characteristic L shape of the plot of side-norm against residual norm

However, Tikhonov and other quadratic L2 norm based regularization methods introduce smoothing to the data reconstruction. So while the computational advantage of such methods is that they are linear problems, they might not be optimal regularization methods for certain applications. Total variation (TV) regularization is a non-quadratic regularization method in which the non quadratic side-constraint is the L1 norm of the differential of the data (106).

$$\mathbf{x}_{\lambda} = \arg\min\left\{\left\|\mathbf{Ax}-\mathbf{b}\right\|^{2}{}_{2} + \lambda^{2}\left\|\mathbf{Dx}\right\|\right\}$$

D is an approximation of the gradient operator. Unlike Tikhonov regularization, TV can contain localized steep gradients and preserve edges in reconstruction, and is hence often known as the right regularizer for signal/image reconstruction (106). But the TV regularization is difficult to formulate as it is a non-linear convex optimization problem.

6.3 Histogram transformation

Since there is lot of variability in the intensity scale of MR images obtained with the same protocol due to experiment variables such as positioning of the coil, amplifier transmit gain etc, Nyul et al (109,110) proposed a strategy for transforming image histograms to a standard template. This would ensure that MR images obtained at the same anatomical site using the same protocol would have same implications for a particular intensity level. The algorithm consists of two stages. In the first or training stage, a training dataset consisting of N image volumes acquired with the same protocol are collected. Inputs to the training algorithm are the training dataset, s_1 and s_2-the minimum and maximum intensities of a chosen standard scale and a landmark feature vector [p_1 p_2 μ]. Among the features, p_1 and p_2 is the chosen lowest and highest percentile of the histogram that will be mapped to s_1 and s_2 respectively and μ is the mode of the foreground object in case of a bimodal histogram, or the point of a curvature of -1 in unimodal histogram and so forth, depending on the application. Let an image volume be denoted by $V = \{v, g\}$ where v is the 3D array of voxels in the image volume V and g is

the image intensity function that assigns an intensity value to each v. The formula for mapping g(v)=x in a training dataset entry V_i to x' is (109,110)

$$x' = s_1 + \frac{x - p_{1j}}{p_{2j} - p_{1j}}(s_2 - s_1) \qquad [6.4a]$$

Consequent to the mapping, the landmark μ_i' is recalculated. The output of the training phase is a rounded mean

$$\mu_s = \frac{1}{N}\sum_{i=1}^{N} \mu_i' \qquad [6.4b]$$

Once a standard histogram template is obtained from the training phase, histogram transformation can be applied to any image volume obtained with the same protocol. Inputs to the transformation phase are an image volume V_i, the histogram feature vector description [p_1 p_2 μ] and the standardized feature value of μ_s. The histogram transformation is performed as follows (109,110):

$$\begin{aligned} \tau v_i(x) &= \left[\mu_s + (x - \mu_i)\frac{s_1 - \mu_s}{p_{1i} - \mu_i} \right], \text{ if } m_{1i} \le x \le \mu_i \\ &= \left[\mu_s + (x - \mu_i)\frac{s_2 - \mu_s}{p_{2i} - \mu_i} \right], \text{if } \mu_i \le x \le m_{2i} \end{aligned} \qquad [6.4c]$$

To address the issue of altered histogram characteristics in accelerated images, we followed this strategy. In our case, the training dataset comprised of conventional fully gradient encoded (R=1) images specific to an anatomic site and imaging protocol. Histograms of accelerated images were transformed to the standard template using the standardized feature values obtained in the training phase. The feature vector was chosen to be [p_1 p_2 μ_i] where p_1, p_2 and μ_i are the 0.5^{th}, 98^{th} and 50^{th} percentiles respectively.

6.4 Methods

6.4.1 MR Dataset

The modified image reconstruction and image processing techniques were applied to MR raw k-space data previously acquired in parallel imaging experiments conducted at 3 T (Chapter 4). Three acquisitions at the knee and three acquisitions at the hip conducted at 3 T were used in this work for investigation into accuracy of bone parameter quantification from accelerated images. For the shorter (longer) acquisition at the knee, a 16 (42) slice dataset had been acquired with the custom built dual phased array coil (111) in the axial plane with an in-plane resolution of 190 μm and slice thickness of 500 μm, TR/TE/BW of 10/2.7/32 ms/ms/KHz using a multiple balanced steady state free precession (m-bSSFP) sequence, for a fully gradient encoded acquisition time of 4 minutes (10 minutes 45 seconds). For the shorter (longer) acquisition at the hip, a 32 (48) slice dataset had been acquired with the same dual phased array coil in the coronal plane with an in-plane resolution of 234 μm and slice thickness of 1000 μm, with TR/TE/BW of 8.2/2.3/42 ms/ms/KHz also using a m-bSSFP sequence, for a fully gradient encoded acquisition time of 7 minutes 26 seconds (11 minutes 10 seconds). Previously it was observed that image quality was preserved till an acceleration factor R=3 for short acquisitions and till R=4 for longer acquisitions at the knee and the hip at 3 T (Chapter 4) (13). So we investigated bone morphology measurements for R=3 and for R=3-4 for the shorter and longer acquisitions respectively.

6.4.2 Image Reconstruction

To eliminate sources of variation in structural measurements other than that caused by the parallel reconstruction, such as motion between scans, accelerated acquisitions (R=3,4) were simulated from the R=1 datasets. The complex full k-space data was decimated to simulate accelerated acquisition and the undersampled datasets were reconstructed once by regularized and once by unregularized GRAPPA based reconstruction. Regularized GRAPPA (rGRAPPA) based reconstruction involved Tikhonov regularized signal matrix inversion for computation of GRAPPA reconstruction weights.

$$\mathbf{n}_{\lambda} = \arg\min_{\lambda} \left\{ \left\| \mathbf{S}_{\mathbf{src}} . \mathbf{n} - \mathbf{S}_{\mathbf{tgt}} \right\|^2_2 + \left\| \mathbf{n} \right\|^2_2 \right\} \qquad [6.5]$$

The regularization was incorporated in our MATLAB reconstruction routine (Chapter 4) using MATLAB's regularization toolbox (108).

For cases where Tikhonov regularization might not achieve desired result, an alternative regularized reconstruction technique based on total variation (TVGRAPPA) was devised. Another point of difference with the rGRAPPA method was that it applied the regularization in the image domain subsequent to the GRAPPA based reconstruction of k-space data. Let the initial estimate of the desired image, x_rec be the image corresponding to the GRAPPA-reconstructed full k-space data. Let x_losamp be the low resolution image corresponding to the calibration/training region of the k-space image (Fig. 4.3). Let R be the resampling matrix that downsamples x_rec to match the resolution of x_losamp. Let D be an approximation of the gradient operator and TV be the desired total variation in the image. If x_rec is resampled to the same resolution as x_losamp, we would want to minimize the residual norm between resampled x_rec and x_losamp. As a side constraint, we would also like the sum of all edge intensities in the

desired image to be < TV. TV was estimated from a set of images obtained with the same protocol but with full gradient encoding. The pseudo-code for the TV regularization can be written as:

minimize $\left\| R * x\_rec - I\_losamp \right\|_2^2$

subject to

$$\left\| D * x\_rec \right\| \leq TV \qquad [6.6]$$

The non-linear convex optimization was incorporated in our MATLAB reconstruction routine using the convex programming toolbox (112).

6.4.3 Image post-processing and analysis

All reconstructed images were demodulated of intensity variations arising from variations in coil sensitivity and binarized by the dual threshold method (30,32). They were then analyzed for measurement of trabecular bone micro-structural parameters. Of the bone structural measures analogous to histomorphometry (Section 2.2), the two independent measures are trabecular number density (App. TbN) and trabecular thickness (App. TbTh). Of these, trabecular thickness measurement has compromised accuracy and limited sensitivity due to the limited spatial resolution regime in MRI. In contrast, App. TbN has been found to be an important indicator of osteoporotic condition (37,38). Moreover, in our previous study, measurement of App. TbTh did not show a trend of variation while App. TbN showed a clear trend of overestimation with acceleration factor. So we chose to investigate the accuracy in measurement of App. TbN as well as BF between unaccelerated and PI datasets.

In the training phase of the histogram transformation (HT), two training datasets were built – one from the R=1 acquisitions at the knee and the other from R=1 acquisitions at the hip. The range of the chosen standard scale was 5000 and the lowest (p_1) and highest percentiles (p_2) were chosen to be the 0.5^{th} and 98^{th}. Once the histograms of the training imagesets were mapped to the standard template [Eq. 6.4a], the standardized value of the 50^{th} percentile (μ), was calculated. In cases where the BF measured from the rGRAPPA images showed more than 5% difference from the corresponding R=1 measure, the rGRAPPA images were subjected to histogram transformation according to Eq [6.4c].

6.5 Results

Representative images of the trabecular bone structure at the proximal femur (hip) for R=1, R=3 GRAPPA and R=3 rGRAPPA are shown in Fig. 6.2. It can be seen that the rGRAPPA image is slightly less noisy than the GRAPPA image.

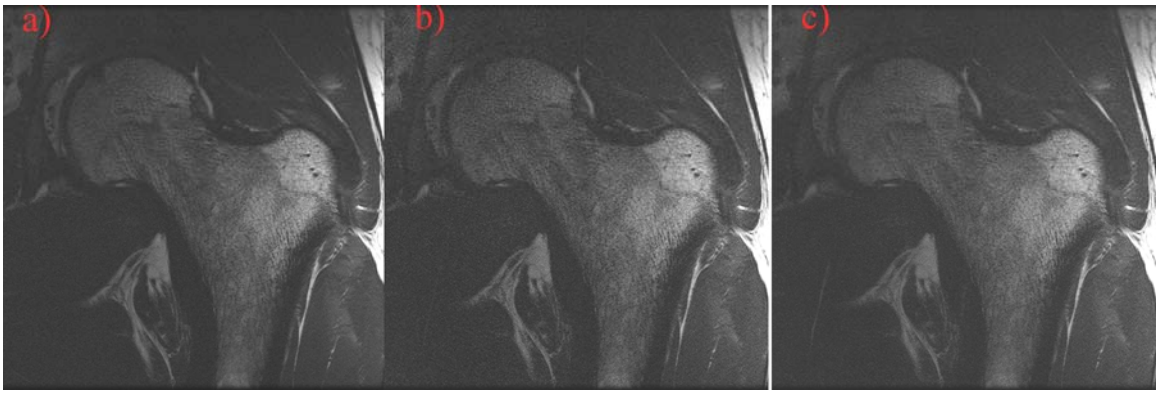

Figure 6.2 shows representative a: R=1 and three fold accelerated images of the bone structure at the hip reconstructed by b: GRAPPA and c: rGRAPPA methods. The rGRAPPA image is slightly less noisy and smoother than the GRAPPA image.

The difference in App. TbN measure between R=1 and accelerated images was considerably reduced in most cases when Tikhonov regularization was incorporated in the GRAPPA reconstruction. In cases where the BF measure differed >= 5% between the R=1 and the rGRAPPA image, a histogram transformation (HT) was applied to the rGRAPPA image and the image intensities were mapped to the standardized histogram. This further lowered the difference in BF and App. TbN measurements from R=1. Percentage difference in BF and App. TbN measures between R=1 and accelerated datasets for the knee and the hip are shown along with the SNR of the corresponding GRAPPA images in Table 6.1 and 6.2 respectively. Image intensity histogram of an accelerated image before and after the HT operation is shown in Figure 6.3.

Table 6.1 Percentage differences in BF and App. TbN measures between R=1 and R=3 images of the knee for different reconstruction methods

	SNR of R=3 GRAPPA	***R=3 GRAPPA***		***R=3 rGRAPPA***	
		BF	*App. TbN*	*BF*	*App. TbN*
Sub1	*12.12*	*0.6*	*7*	*2*	*5.6*
Sub2	*9.42*	*8.68*	*14*	*0.5*	*8.5*
Sub3[*]	*17.65*	*2.69*	*3.27*	*3*	*0.93*

Table 6.2 Percentage differences in BF and App. TbN measures between R=1 and R=3 images of the hip for different reconstruction and post-processing methods

	SNR of R=3 GRAPPA	***R=3 GRAPPA***		***R=3 rGRAPPA***		***R=3 rGRAPPA+HT***	
		BF	*App. TbN*	*BF*	*App. TbN*	*BF*	*App. TbN*
Sub1	*14.53*	*15.12*	*13.7*	*9.5*	*5.18*	*-0.47*	*-0.91*
Sub2	*10.8*	*16.01*	*16.45*	*11.5*	*10.54*	*4.14*	*7.19*
Sub3[*]	*15.22*	*8.302*	*4.35*	*6.98*	*3.98*	*4.43*	*-0.36*

* Long acquisition

In the long acquisition at the knee, difference in App. TbN and BF measure between R=1 and R=4 rGRAPPA knee images was 3.6% and 2.7% respectively. SNR of the corresponding R=4 GRAPPA image was 13.24. In the long acquisition at the hip, difference in App. TbN and BF measure between R=1 and R=4 rGRAPPA+HT images was 8 % and 4.3% respectively. SNR of the corresponding R=4 GRAPPA image was 8.6.

Since the App. TbN measurement difference was relatively high for both the 2nd knee (8.5%) and hip (7.19 %) acquisitions with the rGRAPPA method, the datasets were re-reconstructed using the TVGRAPPA method. Using this reconstruction and the HT post processing operation, the measurement differences in BF and App. TbN between R=1 and R=3 for the second hip acquisition were reduced to 0.4% and 4.22% respectively while the measurements remained unchanged for the other case. However, image blurring was avoided in both cases.

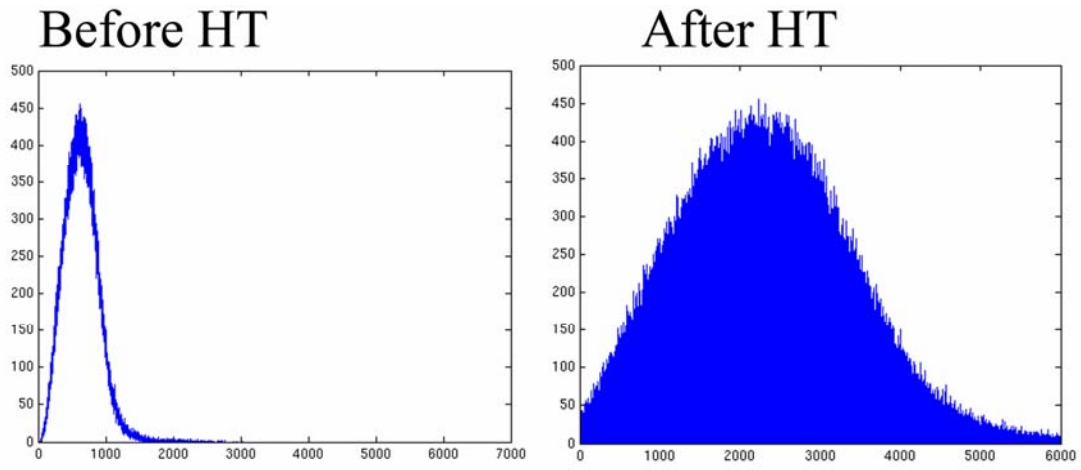

Figure 6.3 shows the representative image intensity histogram of an R=3 rGRAPPA image before and after HT operation.

6.6 Discussion and Conclusion

Measurement differences between R=1 and accelerated datasets was high when the SNR in the image was <~ 10. SNR can decrease steeply from one acceleration to the next, when the spatial encoding capability of the coil array is exceeded as was the case for the long hip acquisition at R=4 (Fig. 4.7). In most other cases, measurement accuracy was improved using Tikhonov regularization with the reconstruction and the histogram-based post-processing.

Regularization offers a trade-off between reconstruction error and noise smoothing, so aliasing artifacts increase in regularized parallel reconstruction. Additionally, choice of regularization parameter λ by the L curve method might not be appropriate when the plot of residual norm against side norm (Figure 6.1) does not lend itself to the characteristic L shape. One such example (for the 2^{nd} hip acquisition) is shown in Figure 6.4.

Other disadvantages of the rGRAPPA method proposed here is that the quadratic regularization has a smoothing effect which might manifest as slight image blurring. To avoid image smoothing and the aliasing artifacts, the TVGRAPPA method was also proposed in which the side constraint involves L1 norm of image gradients and the regularization is performed in the image domain. Using this method for the two cases where measurement differences from R=1 were considerable even when images were reconstructed by the rGRAPPA method, quantification accuracy improved in one but was unchanged in the other. The major disadvantage of the TVGRAPPA method is its computational complexity.

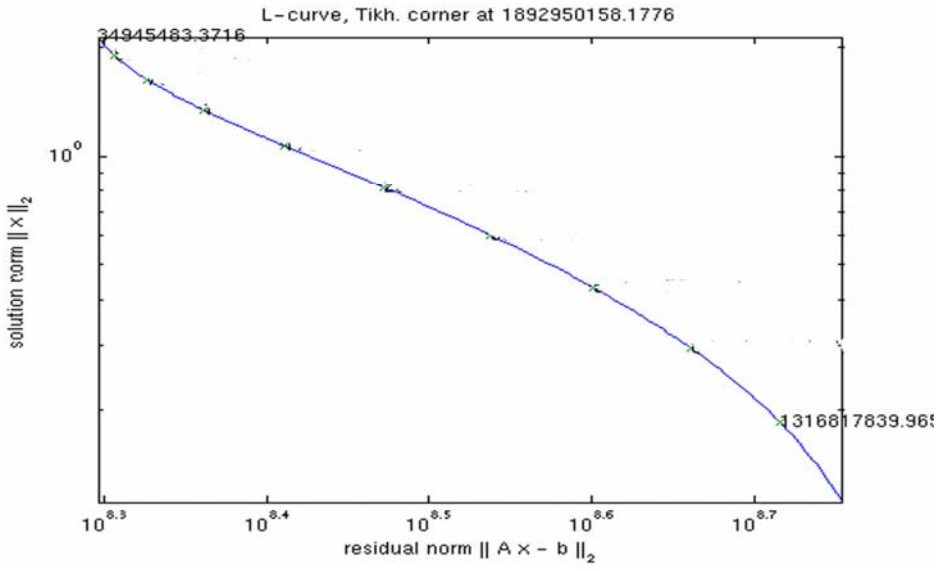

Figure 6.4 shows the plot between the residual and L2 side-norm for a three-fold accelerated dataset at the knee. This is an example case where the plot does not have a characteristic L shape.

The training dataset used in this work for the histogram transformation consisted of only 4 datasets. Robustness of this image processing technique can be improved by inclusion of more training data. Efficacy of this method using standardizing features other than the median of the histogram should also be investigated.

As seen from the results, pMRI images cannot be analyzed for bone structure if the image SNR is below a certain limit. So a sufficiently high baseline SNR is crucial for this application. Adverse effects of g-factor induced noise amplification on the image analysis can be minimized by using coil arrays and experimental set-ups optimized for this pMRI application and by not exceeding the encoding capability of the array. Values of the g-factor have also been seen to decrease with increasing field strength. This is probably why the accuracy of bone structural measurements from accelerated images improved from 3 T to 7 T (Chapter 5). Analyses of images acquired at the calcaneus of 3

healthy subjects at 7 T showed as low as 4.4% and 6.79% mean difference in App. TbN measure for R=3 and R=4 respectively from R=1.

In conclusion, this work has proposed image regularization and histogram based processing methods that can facilitate robust quantification of morphology metrics from accelerated HR-MR images of trabecular bone micro-architecture, provided there is sufficient image SNR and the MR detector array is optimized for the pMRI application.

Chapter 7

Parallel imaging applications beyond osteoporosis

7.1 Motivation

The implementation of a GRAPPA based parallel imaging technique and its optimization for high resolution imaging of trabecular bone micro-architecture was previously described in Chapters 4, 5 and 6. In this section the robustness and flexibility of the technique will be tested for two neurological applications- MR spectroscopic imaging of brain metabolites and susceptibility weighted imaging (SWI) of brain vasculature. Spectroscopic methods provide biochemical information by mapping the metabolite concentrations in localized voxels. In clinical settings, the combination of magnetic resonance imaging (MRI) and magnetic resonance spectroscopy (MRS) is a powerful tool for detecting anatomical and biochemical changes in disease conditions such as brain tumors and other neurological diseases, stroke, prostatic tumors to name a few. The disadvantage of spectroscopic imaging is that it typically requires long acquisition times in the order of 20-40 minutes (113). Susceptibility weighted imaging (SWI) in an emergent technique for high resolution, distortion-free imaging of brain vasculature that has recently been shown to improve the diagnosis of brain neoplasms, neurological trauma, and vascular malformations, in addition to a variety of cerebrovascular and neurodegenerative diseases (114). The susceptibility weighting relies on changes in phase that result from signal loss due to partial volume effects near venous vessels, typically requiring long echo times to obtain sufficient weighting (115). This prolongs the

acquisition times. So the above two imaging methods are good candidates for acceleration. Since both these methods are phase-sensitive, they are also a good test for the robustness of our reconstruction technique. Moreover spectroscopic acquisition yields 4 dimensional data compared to the 3 dimensional data generally obtained from MRI. So our GRAPPA based reconstruction technique had to be extended to be able to process the 4D data. This also tested the flexibility of our reconstruction method.

A 7.2 Magnetic Resonance Spectroscopic imaging of brain metabolites

MR spectroscopy (MRS), like MRI is based on the principle of nuclear magnetic resonance. In MRS however, the signal coming from protons is further resolved into a resonant frequency spectrum. The phenomenon due to which protons have different resonant frequency in different molecular configuration is chemical shift.

Chemical Shift

In the presence of an external magnetic field, the electrons surrounding an atom generate a magnetic field opposing the external field. This has a shielding effect on the nucleus, the effect of shielding depending on the local electron density and the atoms the nucleus is bonded to. So the net magnetic field (B_i) experienced by a nucleus also depends on the molecular structure, and can be written as

$$B_i = B_0(1-\sigma_i) \qquad [7.1a]$$

where σ_i is the shielding for nucleus i. The Larmor frequency of the nucleus is also modified as:

$$\omega_i = \gamma B_i (1 - \sigma_i) \qquad [7.1b]$$

The chemical shift of a spectral component is defined as the normalized difference of the resonant frequency from a reference frequency and is displayed on a scale of parts per million (ppm).

$$\delta_i = \frac{\omega_i - \omega_{ref}}{\omega_{ref}} x10^6 \qquad [7.1c]$$

The normalization removes the B_0 dependence of the chemical shift.

So in contrast to MRI which mainly provides anatomical information, MRS is a method for imaging the biochemical composition of tissues. Chemical compounds/metabolites are identified by their chemical shift in the spectrum and their concentration is assessed from the height and area under the peak (19).

At a long echo time of 144 ms, the peaks of five metabolic compounds can be identified in brain tissue: choline (Cho), creatine (Cre), N-acetyl aspartate (NAA), lactate (Lac), and lipid (Lip). In normal brain, levels of Cho and Cre are similar and the NAA peak is 1.5-2 times larger. MR spectra from brain tumors can be distinguished by elevated Cho, reduced NAA, and in some cases elevated lipid levels. Increase in Cho is thought to be due to increased cell density and membrane turnover. The reduction of NAA in growing gliomas is attributed to displacement and damage of surrounding neurons. Elevated lipid levels denote the cellular membrane breakdown associated with cell death and are often observed in spectra from necrotic tissue, where all other metabolic activity is suppressed (113). Brain cancer is a debilitating disease with median survival of about 1 year for the highest grade lesions (116). Ninety percent of primary

brain tumors in adults older than 45 are gliomas, which originate from the glial cells that are the support cells for neurons. Accurate localization and spatial characterization of gliomas is crucial for planning effective treatments including surgical resection, radiation therapy and chemotherapy. Although pre and post contrast T1 weighted imaging and T2 weighted inversion recovery methods are sensitive to tumor detection, demarcation, spatial characterization and staging of tumors can be made more accurately by combining the diagnostic capabilities of MRI and MRS.

Early MRS acquisitions were mainly single voxel spectroscopy (SVS). Since then, 2 dimensional (D) and 3D MR spectroscopic imaging (MRSI) methods have evolved. Magnetic resonance spectroscopic imaging (MRSI) combines the features of both imaging and spectroscopy, by collecting spectral data from multiple voxels that have been spatially encoded by phase-encoding gradients, after the image volume has been localized. Point resolved Spectroscopy (PRESS) is a volume localization method which applies 90°-180°-180° RF pulses (117). Each RF pulse selects an orthogonal plane so that the localized volume is defined as their intersection. In 3D MRSI, phase encoding gradients are applied similar to MRI, in x, y and z directions subsequent to localization (19).

The obvious advantages of MRSI over single voxel spectroscopy are finer spatial resolution and the provision of overlaying spectral maps on anatomical images. However, MRSI involves long acquisition times, in the order of 20-40 minutes which can cause patient discomfort and motion induced artifacts. Several pulse sequences such as spiral and echo-planar methods were developed to accelerate MRSI by collecting more data points per excitation (118). In elliptical MRSI scan time is reduced by acquiring signal

from the central ellipsoidal portion of k-space (119). Employment of parallel imaging techniques allows a more generalized approach to scan time reduction since they can be combined with any MR sequence. Using the SENSE algorithm, Dydak et al presented a sensitivity encoded 2D spectroscopic imaging technique, with undersampling in 2 phase-encoding directions resulting in net four folds reduction of scan time (120). Ozturk-Isik et al applied the SENSE-MRSI to imaging of gliomas at 3 T (16). However, SENSE reconstruction has certain limitations when there is slight aliasing in the FOV even in the fully encoded acquisition (67). Furthermore, at high fields > 3 T, estimation of coil sensitivity can be technically challenging. In this work we present a fast MRSI method using a GRAPPA based autocalibrating parallel technique and apply it to 3D MRSI with Cartesian as well as elliptical sampling trajectories at 3 Tesla (T) with two-fold acceleration in two phase-encoding directions, k_x and k_y.

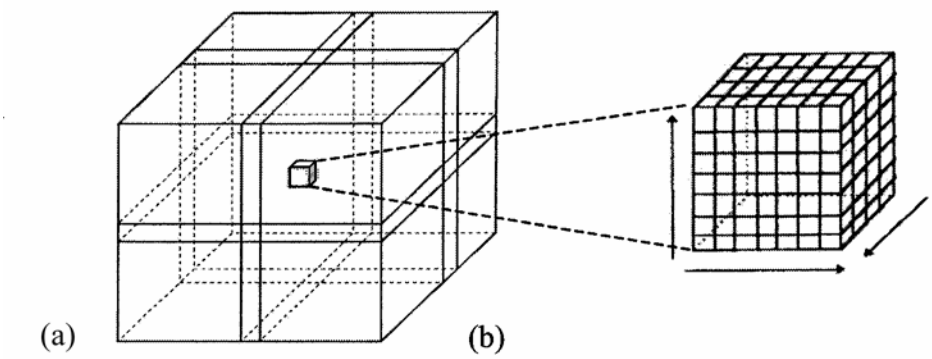

PRESS Localization Spatial Encoding for SI

Figure 7.1 shows schematic representation of PRESS localization and spatial encoding by phase encoding gradients in 3D MRSI

A 7.3 Methods

A 7.3.1 Data Acquisition

The sampling scheme for 3D PRESS MRSI sequence was modified for autocalibrating parallel acquisition. The sampling scheme in cases of elliptical, Cartesian GRAPPA and elliptical GRAPPA acquisition for a 16x16x8 spectral array is shown in Fig 7.2. For the GRAPPA acquisitions, an acceleration factor of 2 and 2 AC lines were used in each of k_x and k_y directions.

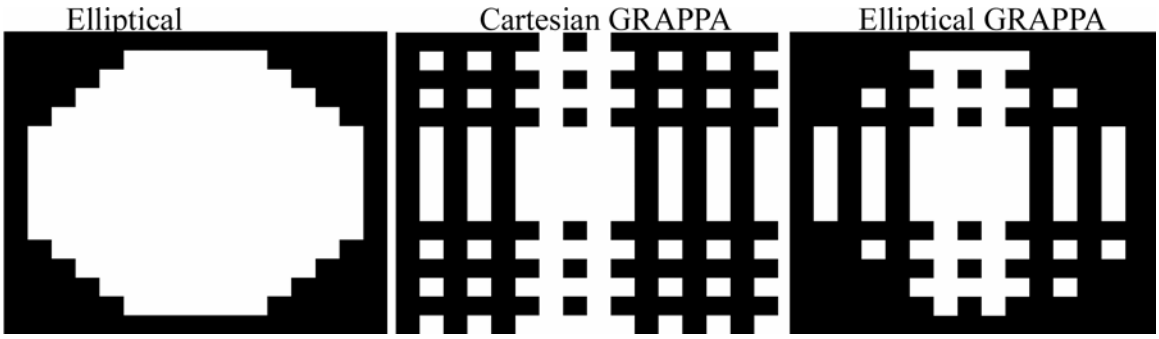

Fig 7.2 shows the sampling schemes in kx-ky plane for 16x16 Elliptical, Cartesian GRAPPA and Elliptical GRAPPA methods

MR exams were conducted on a 3 T clinical MR scanner (GE Healthcare, Milwaukee, WI) using an eight channel RF coil (MRI Devices Inc, Gainesville, FL). 3D Cartesian GRAPPA spectroscopic data with two fold acceleration and 2 AC lines in k_x and k_y directions of a 12x12x8 spectral array (time:10:06 min) were acquired from 2 volunteers and 3 patients. Full 12x12x8 spectral datasets (time: 21:12 min) were acquired from volunteers and elliptical 12x12x8 spectral datasets (time: 9:28 min) were acquired from patients because of time constraints, for comparison with the partially parallel datasets. 16x16x8 3D elliptical GRAPPA spectroscopic data was acquired from 3 volunteers and 6 glioma patients with R=2x2 and 2 AC lines in a scan time of 9:25 minutes. For

comparison, full elliptical 16x16x8 spectral array (time: 17:32 min) was acquired from the volunteers and elliptical 12x12x8 spectral array (time: 9:28 min) was acquired from patients because of scan time limitations. All the spectroscopic acquisitions were conducted with PRESS localization in conjunction with CHESS (121) water and VSS outer volume suppression (122) (TR/TE=1.1s/144 ms). The imaging protocol also acquired T1-weighted SPGR (TR=26 ms, TE=3 ms, 3 mm slice thickness, 256x256 matrix, FOV=240x240 mm, flip angle = 40°), T2-weighted FLAIR (TR=10002 ms, TE=127 ms, TI=2200 ms, 3 mm slice thickness, 256x256 matrix, FOV=240x240 mm, flip angle=90°) and proton-density weighted fast gradient echo coil sensitivity images (TR=150 ms, TE=2.1 ms, 3 mm slice thickness, 64x64 matrix, FOV=300x300 mm, flip angle=20°).

A 7.3.2 Spectral Data Reconstruction

Undersampled spectral data was reconstructed by a GRAPPA based algorithm developed in MATLAB (The Mathworks Inc., Natick, MA) on a Sun workstation. The data from 3D MRSI acquisition has 3 spatial frequency dimensions – k_x, k_y, k_z and a time dimension for the free induction decay. After an inverse Fourier Transform in the z direction the spectral data was processed by two-dimensional GRAPPA reconstruction slice by slice. Griswold et al showed that multi-dimensional GRAPPA reconstruction can be split into multiple one-dimensional GRAPPA reconstructions (123). In our case, we split the 2D GRAPPA reconstruction into two consecutive 1D GRAPPA reconstructions G_{ky} and G_{kx} along k_x and k_y respectively. The basic GRAPPA equation (Eq. 4.4) for spectroscopic imaging can be written in matrix format as,

$$\mathbf{S}_j(k_y - m\Delta k_y, \mathbf{k}) = \mathbf{n}^T\mathbf{S} \qquad [7.2a]$$

$$\mathbf{n}^T = [\mathbf{n}_1^{(m)T} \ldots . \mathbf{n}_L^{(m)T}]$$

$$\mathbf{S} = \begin{bmatrix} \mathbf{S}_1(ky - \mathbf{b}R\Delta ky, \mathbf{k}) \\ . \\ . \\ \mathbf{S}_L(ky - \mathbf{b}R\Delta ky, \mathbf{k}) \end{bmatrix}$$

For the GRAPPA reconstruction along k_y direction, **S** has a matrix size of LN_b x (N_{kx} x $N_{spectra}$), where N_{kx} and $N_{spectra}$ are the sizes of the k_x and the spectral dimensions respectively, N_b is the block-size and L is the number of coils. The vector **k** of length (N_{kx} x $N_{spectra}$) specifies the two-dimensional position in (k_x, t) space, $\mathbf{n_i^{(m)}}$ is the vector of interpolation weights of length N_b for coil i. Floating node fitting (FNF) was used for computation of GRAPPA reconstruction weights and multi-column-multi-line interpolation (MCMLI) was used for synthesis of missing data .

In elliptical sampling, signal is not acquired from the outer k-space positions. This might bias the GRAPPA based filtering operation for synthesis of missing data in case of undersampled elliptical datasets. So a linear extrapolation operation was employed to extrapolate the elliptical undersampled data onto a Cartesian grid (Figure 7.3).

Figure 7.3 is a schematic diagram of the linear extrapolation operation

This was followed by synthesis of the full k-space data by GRAPPA reconstruction and subsequent multiplication by an elliptical mask. The flow diagram of the reconstruction is shown below in Figure 7.4.

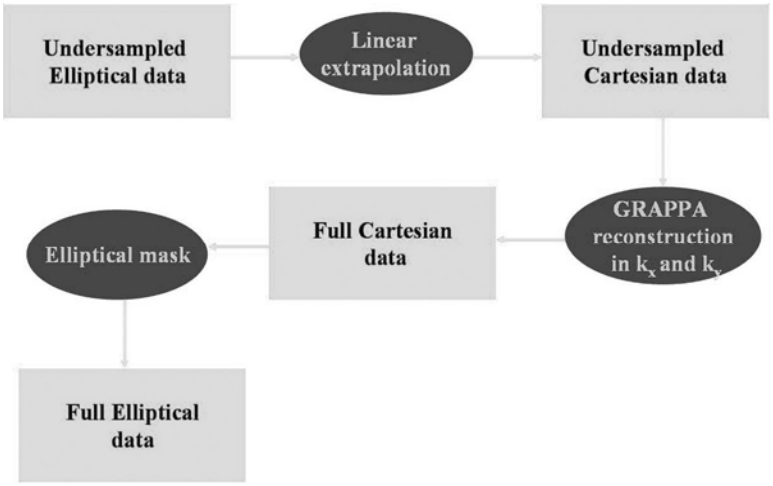

Figure 7.4 is a flow diagram of the linear extrapolation and GRAPPA reconstruction of full elliptical data from undersampled elliptical dataset.

A 7.3.4 Data Processing

The GRAPPA reconstructed data of each individual coil element was subsequently processed identically as the full dataset, on a Linux cluster. Regions of hyper-intensity on T2-FLAIR images were segmented using an in-house region growing algorithm to differentiate tumor areas (55). Voxels in the PRESS box outside of the T2 hyper-intensity were assumed to represent normal brain. Individual proton density images from coils were normalized and processed for estimation of individual coil sensitivities. The spectral data from each coil was apodized by a 4 Hz Lorentzian filter, and Fourier transformed from (k_x, k_y, k_z, t) to the (x, y, z, f) domain. After this pre-processing, each voxel was analyzed separately, and the spectra were phased, frequency shifted to match a template

peak file, and water baseline was removed using in-house developed software (113). The spectra from all the coils were then combined as a weighted sum using the smoothed coil sensitivity maps (124).

A 7.3.5 Data Analysis

Choline, Creatine, and NAA peak heights were estimated in the frequency domain from the real spectra (113). Lipid peaks might have a different phase due to aliasing. So NAA and lipid heights were also separately estimated from the absolute spectra, and voxels within the normal regions for the volunteer and patient data were classified as lipid contaminated if the absolute peak height of Lipid was higher than NAA. The SNR of Cho, Cr and NAA, were estimated by normalizing their heights with the standard deviation of the spectral noise calculated from the right end of the spectrum. SNR efficiency was calculated by normalizing SNR by square root of the scan time. Median Cho/NAA ratios were measured in the normal and tumor regions. Spearman rank correlation coefficients (r) were computed to assess how well the Cho/NAA ratio in all the voxels in normal and tumor regions correlated between the full and corresponding GRAPPA spectra. A Mann-Whitney rank sum test was conducted on all spectral acquisitions from patients to determine if a statistically significant difference was detected in the Cho/NAA ratio measure between tumor and normal regions.

A 7. 4 Results

Although a 2x2 acceleration factor (R_x=2, R_y=2) was employed, scan time reduction was only 2.12 folds with Cartesian GRAPPA compared to full Cartesian spectral acquisition,

and 1.87 folds in case of elliptical GRAPPA compared to full elliptical spectral acquisition. This is because the number of autocalibrating lines (=2) is a considerable percentage of the spectral dimension. Median SNR decrease in GRAPPA datasets was 1.91±0.9 for the Cartesian case and 1.27±0.9 in the elliptical case. The SNR efficiency decrease was 1.3 folds for Cartesian and 0.93 folds for elliptical sampling between full and GRAPPA datasets. So, there was a slight increase in SNR efficiency for the elliptical case. Median Cho/NAA measured from the whole PRESS region for the full and Cartesian GRAPPA sampling are shown in Table 7.1 and those for the elliptical and elliptical GRAPPA case are shown in Table 7.2. Cho/NAA ratio measures were significantly ($p<0.001$) correlated between GRAPPA and unaccelerated acquisition for all the subjects for both Cartesian and elliptical sampling. An increase in lipid contamination was observed in the GRAPPA method compared to the conventional method (Table 7.3 and 7.4).

The Cho/NAA ratio was not significantly different ($p>0.05$) between the tumor and normal regions for either the full or the GRAPPA method in the first patient while only the full method was able to detect a significantly ($p<0.05$) higher Cho/NAA ratio in the tumor region for the second patient in the Cartesian sampling case. For the elliptical case, the tumor region was distinguished from the normal region by both methods in 3 patients ($p<0.05$) and undetected by both methods in 1 patient ($p>0.05$). Figure 7.5 shows representative spectral data from a volunteer for fully sampled elliptical and elliptical GRAPPA acquisition. Figure 7.6 shows a representative glioblastoma multiforme case, where the abnormal characteristics can be observed in the tumor region from both elliptical and elliptical GRAPPA spectra.

Table 7.1: Median Cho/NAA values for full and Cartesian GRAPPA acquisitions

	Full	GRAPPA	Correlation coefficient (r)
Volt1	.46	.49	0.69
Volt2	.49	.52	0.78
Pat1	.51	.63	0.69
Pat2	.64	.63	0.43

Median Cho/NAA values computed from the whole PRESS box for the fully sampled and Cartesian GRAPPA acquisitions and the Spearman's rank correlation coefficient (r) between the acquisition pairs is shown in Table 7.1. The correlations were significant for all the cases.

Table 7.2: Median Cho/ NAA values for full and Elliptical GRAPPA acquisitions

	Full	GRAPPA	Correlation coefficient (r)
Volt1	0.46	0.47	0.78
Volt2	0.53	0.55	0.77
Volt3	0.45	0.45	0.71
Pat1	0.55	0.58	0.37
Pat2	0.68	0.69	0.65
Pat3	0.68	0.68	0.43
Pat4	0.87	0.88	0.65
Pat5	0.79	0.83	0.62
Pat6	0.8	0.76	0.47

Median Cho/NAA values computed from the whole PRESS box for the fully sampled and Elliptical GRAPPA acquisitions and the Spearman's rank correlation coefficient (r) between the acquisition pairs is shown in Table 7.2. The correlations were significant for all the cases.

Table 7.3 Lipid contaminated voxels (NAA>Lipid) in full and Cartesian GRAPPA acquisitions

	Volt1	**Volt2**	**Pat1**	**Pat2**
Full	0	0	2	0
GRAPPA	0	5	4	24

Table 7.4 Lipid contaminated voxels (NAA>Lipid) in full and Elliptical GRAPPA acquisitions

	Volt1	Volt2	Volt3	Pat1	Pat2	Pat3	Pat4	Pat5	Pat6
Full	0	0	0	1	26	1	1	13	24
GRAPPA	0	0	0	3	17	1	13	3	32

In GRAPPA based reconstruction of spectral data from volunteers, an additional variation in image intensity compared to conventional acquisition was observed towards the edges of the PRESS box (Fig. 7.5). On the other hand, in GRAPPA based reconstruction of spectral data from patients, a poor cavity definition was observed. This was also apparent from smaller variance of NAA, Cho and Cr peak heights across the whole PRESS box for the GRAPPA reconstructed data compared to full data. Smoothing and edge effects in the data might occur due to comparable dimensions of the kernel and the spectral data in k_x and k_y directions. So a smaller kernel size (2x2) might be more appropriate for GRAPPA based reconstruction of spectral data. The time efficiency of this parallel imaging technique might be improved by using a low resolution external calibration scan or by collecting fewer autocalibration lines (1 in k_y, 1 in k_x).

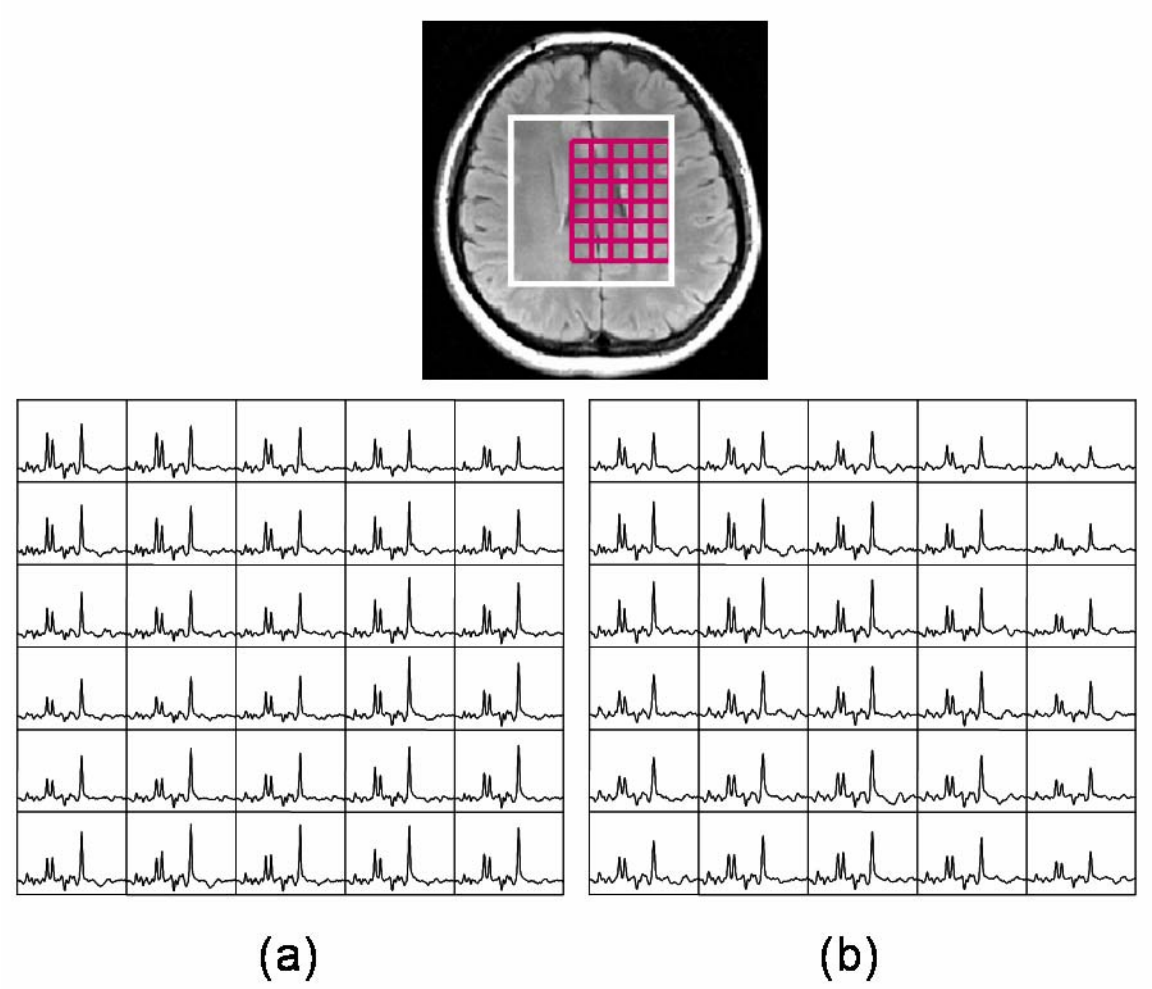

Figure 7.5 shows spectral data from a volunteer acquired a) with fully sampled Elliptical acquisition and b) Elliptical GRAPPA acquisition. The location of the PRESS box is also shown on an anatomical brain image in the figure. As it can be seen the spectral patterns are similar for the two cases though there is slightly more variation in spectral intensity across the PRESS box in the GRAPPA dataset.

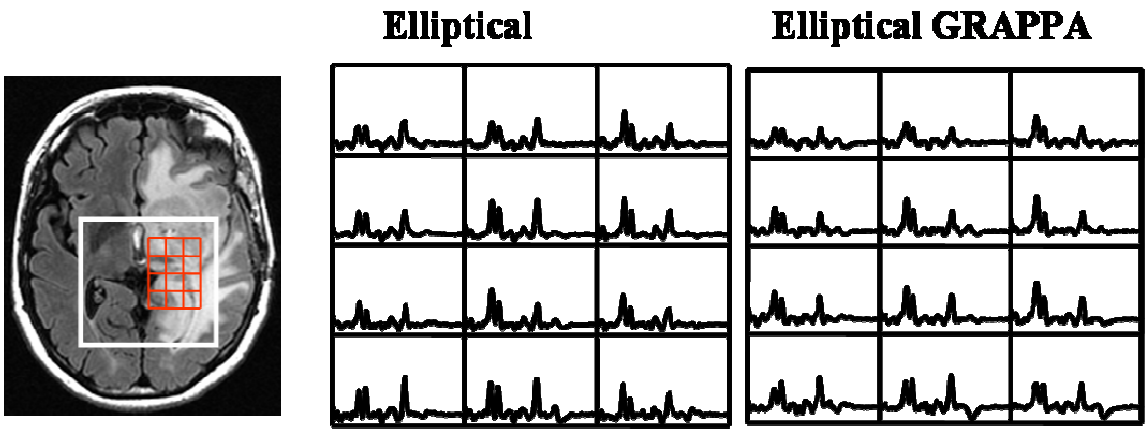

Figure 7.6 shows spectral data from glioma patient acquired a) with 12x12x8 fully sampled Elliptical acquisition and b) 16x16x8 Elliptical GRAPPA acquisition from the tumor region of the PRESS box.

B 7.2 Susceptibility weighted imaging

The traditional technique for measuring relative cerebral blood volume in brain tumors is dynamic susceptibility-contrast perfusion MRI using an echo-planar sequence (125). With the availability of high field magnets, traditional methods becomes a challenge due to increased B_0 inhomogeneity and magnetic susceptibility differences at air-tissue interfaces that lead to signal drop out and large geometric distortions in echo planar imaging. Fortunately, the higher susceptibility differences at high field can also be beneficial. The heightened susceptibility-contrast inherent with increased field strength can be exploited using the phase information contained in conventional gradient-echo sequences to create high resolution susceptibility-weighted venograms (115).

In order to achieve sufficient susceptibility contrast from vessels, while simultaneously minimizing contrast among gray matter, white matter, and ventricles, long echo and repetition times are required. The possibility of using PPI techniques for

accelerating SWI acquisitions at 1.5 T has been proposed previously in the literature. Sedlacik et al. simulated elliptical and GRAPPA k-space undersampling and reconstruction regimes with factor of two reductions for SWI and found reduced contrast of small vessels compared the fully sampled case (126). Although the echo time needed to visualize the large phase changes in venous vessels due to the magnetic susceptibility differences between oxygenated and deoxygenated blood is reduced with increasing field strength, long repetition times are still compulsory to avoid T1-weighting. As a result, the total acquisition time for SWI remains long at higher field strengths (>10 minutes for only a 2 cm slab of tissue at 7 T), which can result in patient discomfort and low scanner throughput. Thus, the need for faster acquisition times and efficient ways of combining multi-channel coil data without losing the phase information as a result of the reconstruction becomes apparent.

B 7.3.1 Data Acquisition

High resolution T2*-weighted brain MR imaging was performed on 6 healthy volunteers using a 7 T whole body MR scanner (GE Healthcare Technologies, Milwaukee, WI) with a volume transmitter and an eight channel phased-array head coil as receiver(Nova Medical, Wilmington, MA). The susceptibility weighted imaging employed a 3D flow compensated, SPGR sequence with TE/TR=16/80ms, flip angle=20°, BW=62.5 kHz, and 24x24x2.8 cm^3 FOV. For GRAPPA acquisitions, variable density acquisition for autocalibration was incorporated in the pulse sequence. The full FOV volunteer scans utilized a 512x256x28 image matrix, while the GRAPPA-based acquisitions employed either a 512x144x28 image matrix (for R=2) or 512x102x28 image matrix (for R=3),

including 16 autocalibrating lines. The imaging protocol also included the acquisition of a low resolution, proton-density weighted, fast gradient echo sequence (TE/TR=2.1/150 ms, flip angle=20°, a 30 x 30 cm^2 FOV, 64 x 64 image matrix, and 3 mm slice thickness) for coil sensitivity estimation.

B 7.3.2 Image reconstruction and post processing

The raw complex k-space data from all coils was transferred off-line to a SunBlade 2000 Workstation (Sun Microsystems, Santa Clara, CA). The previously developed GRAPPA-based reconstruction algorithm (Chapter 4) (13) was used to reconstruct full-FOV images from the undersampled data. SWI post-processing was performed on both GRAPPA-reconstructed and R=1 images on a coil-by-coil basis using in house routines developed with Matlab 6.5 software. SWI utilizes phase contrast to attenuate the signal intensity from venous vessels in the magnitude images. Phase masks were constructed from the full complex image data of each individual coil element through complex division by a low-pass filtered image and scaling the resulting negative phase values between zero and one (115). The phase masks were then multiplied into the magnitude image from each coil 4 times and the resulting susceptibility-weighted images from each individual coil were combined by square root of weighted sum of squares method, the weighting being inversely proportional to the noise variation in each coil (17).

B 7.3.3. Data Analysis

Minimum intensity projections (mIPs) of the susceptibility weighted images were analyzed to determine four main regions from which to calculate vessel contrast, as

demonstrated in Figure 7.7. The mIP images were thresholded to generate brain parenchyma and large vessel masks, while small vessel and adjacent white matter regions were manually identified. Contrast ratios were defined as the mean signal intensity within the background tissue region divided by that within the vessel. The brain parenchyma region was used as the background tissue for the contrast ratio calculation of large vessels, while the sensitivity of detecting small vessels was evaluated using adjacent white matter as the background tissue. The performance of the GRAPPA based reconstructions were evaluated by comparison of contrast ratios to that of R=1 acquisitions. Statistical significance of differences was determined through the use of a Wilcoxon signed rank test.

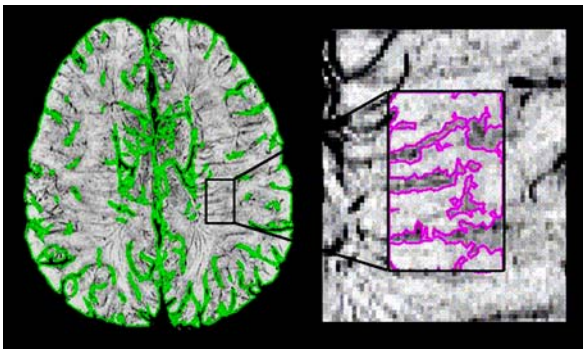

Figure 7.7 shows large vessel mask used to measure the contrast between large blood vessels and the brain parenchyma [Courtesy Lupo, JM et al submitted to Magnetic Resonance in Medicine]

B 7.4 Results

SWI images comparing two and three fold accelerations to the full FOV dataset for a representative volunteer are shown in Figure 7.8. Visual inspection of these images

demonstrates the similar vessel contrast between the full FOV and R=2 acquisitions. For the R=3 acquisition, there was no visible disparity in large vessel contrast compared to the full FOV and R=2 scans, however the visibility of small vessels was slightly hindered. However, small vessel contrast ratios for the R=3 acquired datasets were similar to those from the R=2 scans. Keeping in mind the spatially varying noise amplification associated with parallel reconstruction, SNR measurement was performed by two-repetition method as described by Dietrich O et al. (22), where the average SNR in a given ROI is determined as the ratio of average signal in the ROI of the mean image and the standard deviation of the signal in the difference image. SNR measurements revealed a 37.6% decrease in SNR for the R=2 acquisition, with a 43.1% reduction in total scan time. The R=3 scan showed a 49.3% decline in SNR, but allowed the scan time to be accelerated by 60%. Therefore SNR efficiency of the scan improved with PPI technique.

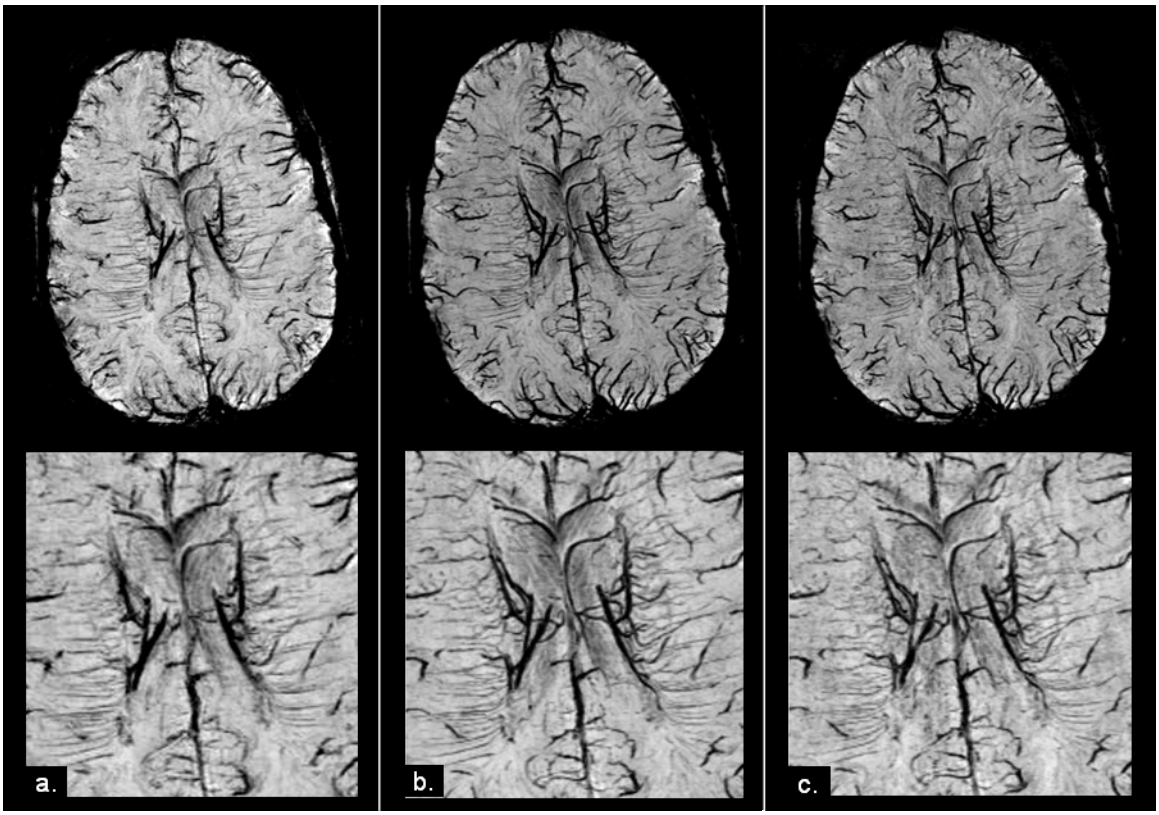

Figure 7.8 shows representative SWI images for R=1, 2 and 3 acquisitions and the magnified view of the small vessels are shown in Figures 7.8a, 7.8b and 7.8c respectively. [Courtesy Lupo JM et al, submitted to Magnetic Resonance in Medicine]

7.5 Discussion

In this work, we tested the robustness of the GRAPPA based technique previously implemented for high resolution imaging of trabecular bone micro-architecture for two different neurological applications- MRSI of brain metabolites and SWI of brain vasculature. The superior quality of image reconstruction and preservation of vessel contrast for R=2 and R=3 compared to R=1 in the SWI application indicates that image phase is accurately reconstructed by GRAPPA based reconstruction. The image reconstruction method was also flexible enough to be extended to process 4 dimensional

spectroscopic data and to be combined with Cartesian as well as elliptical sampling schemes. Cho/NAA measures derived from GRAPPA reconstructed spectral data correlated significantly with the R=1 acquisition and showed significant difference between tumor and normal regions in glioma patients. 16x16x8 elliptical GRAPPA based MRSI can potentially allow for larger spatial coverage compared to regular elliptical 12x12x8 acquisition within the same scan time. The autocalibrating parallel imaging technique might be more time efficient in larger spectral array acquisitions. Alternatively the GRAPPA reconstruction weights might be computed from an external calibration scan.

Chapter 8

Conclusion

8.1 Summary

This thesis developed SNR efficient, fast MR methods primarily to address existing technical limitations in *in vivo* high resolution imaging of trabecular bone micro-architecture for assessment of osteoporosis. High field strength, phased array coils and high magnetization yielding pulse sequence were employed to improve image SNR. Computer simulations were programmed to estimate effects of different protocols and static field strength on image SNR. Using these approaches, previously existing SNR deficiency in imaging trabecular bone micro-structure at the proximal femur (hip) was overcome. This was of considerable clinical significance, since the proximal femur and vertebrae are the two major sites of osteoporotic fractures in the axial skeleton. Next, parallel imaging methods were developed to reduce long scan times (16-20 minutes) associated with HR-MRI of trabecular bone. This allowed up to 2-4 folds reduction in scan time and also added more flexibility to the protocol design. Additionally, image analysis methods were proposed for rigorous characterization of images (resolution, autocorrelation etc) obtained by the pMRI technique and strategies were devised to ensure accuracy of bone structural measurements derived from the accelerated images. The parallel imaging methods were extended to several other imaging applications, namely morphological cartilage imaging for detecting osteoarthritis, spectroscopic imaging and susceptibility weighted imaging for detecting brain tumor.

The major contributions of this thesis can be summarized as follows:

- A framework for estimating signal response in trabecular bone marrow to various pulse sequences was developed by programming a computer simulation of the magnetostatic environment in the bone marrow and of the magnetization response to pulse sequences such as fast gradient echo and balanced steady state free precession using steady state analysis. Using this simulation model:
    - An optimized protocol employing SNR efficient bSSFP pulse sequence was developed for imaging trabecular bone.
    - Increase in signal-to-noise ratio from 1.5 T to 3 T was estimated.
- With the SNR leverage from the bSSFP imaging sequence, the higher field strength of 3 Tesla and phased array coils, it was possible to analyze trabecular bone structure from *in vivo* MR images at the proximal femur for the first time.
- A parallel imaging technique (k-space sampling and reconstruction algorithm) based on GRAPPA was implemented at 3 T to reduce acquisition time of HR-MRI of trabecular bone. Using this technique and an eight channel array for MR signal detection scan time could be reduced up to four folds for trabecular bone MRI. Image resolution and edge sharpness was seen to be preserved to a large extent but structural measurements such as App. TbN were overestimated in accelerated images compared to R=1.
- Using acceleration factor and number of phase-cycles as imaging variables, the additional flexibility in protocol design and potential for SNR improvement was demonstrated for an m-bSSFP protocol.

- Potential and pitfalls of imaging at high field was assessed and the previously developed pMRI technique was adapted to 7 T. Expected improvement in parallel imaging performance from 3 T to 7 T was experimentally verified by comparison of geometry factor and bone structural measurements derived from accelerated trabecular bone images between 3 T and 7 T.
- Using pMRI to reduce scan time and RF power deposition per scan, feasibility of *in vivo* trabecular bone MRI for monitoring osteoporosis and *in vivo* cartilage morphology imaging for monitoring osteoarthritis was established at 7 T.
- The causes of differences in bone structural measures between R=1 and unaccelerated images were analyzed. Regularized reconstruction algorithms and histogram based post-processing techniques were developed to improve the accuracy of bone quantification from accelerated images.
- The pMRI technique was extended to susceptibility weighted imaging of brain vasculature.
- A GRAPPA based pMRI technique was developed to accelerate 3D spectroscopic imaging for 2 k-space sampling cases- Cartesian and elliptical. The parallel imaging method was then used to image brain metabolites in glioma patients.

8.2 Future Directions

8.2.1 Extension of the bone simulation model

The bone model assumed in our computer simulations consisted of spherical trabecular elements immersed in fatty marrow. The bone model could be improved by a more

realistic assumption of interconnected plate and rod like structures and the chemical heterogeneity of the marrow could also be accounted for. Combining the simulations of the magnetostatic environment and response to pulse sequences with that of imaging gradients would allow estimation of the impact of other imaging factors such as spatial resolution, gradient linearity on images as well.

8.2.2 Extension of parallel imaging reconstruction algorithms

Since most of our MR acquisitions involve partial Fourier imaging in the frequency direction, the partial Fourier and parallel imaging reconstruction algorithm could be combined as a projection onto Convex sets (POCS) problem and image constraints specific to the application such as smoothness or steepness of local gradients could be additionally incorporated.

8.2.3 In vivo HR-MRI of trabecular bone structure at the vertebral bodies

While our MR developments have made *in vivo* imaging and analysis of trabecular bone structure at the proximal femur feasible, imaging of the vertebral bodies is still technology limited. The caveats include the small dimensions of the vertebral bodies, their non-peripheral location as well as heterogeneity in the vertebral bone marrow. Using the additional SNR at 7 Tesla, specialized spatial localization pulses and coil arrays, MR methods for imaging the vertebral bodies could be developed. This would have tremendous clinical significance given the high incidence of vertebral fractures and its debilitating impact in osteoporotic patients.

Appendix A

GRAPPA-based reconstruction of large image volumes from data measured from 8 or more channels is computationally intensive, taking several hours on a single desktop Sun (Solaris, USA) workstation. To expedite reconstruction, a parallel computational strategy was devised to distribute the reconstruction of individual image slices to separate CPUs on a Linux cluster. The components of the parallel implementation of the reconstruction software were written in MATLAB and compiled to run on a computational cluster. Reconstructed image slices are output as DICOM format files. As reconstruction of individual slices are independent tasks, distributing each slice to a separate CPU results in nearly a 1/(number of slices) reduction in processing time which makes it sufficiently fast to potentially provide reconstructed images for viewing during an MR exam. A schematic diagram of the parallel processing is shown in Figure A.1.

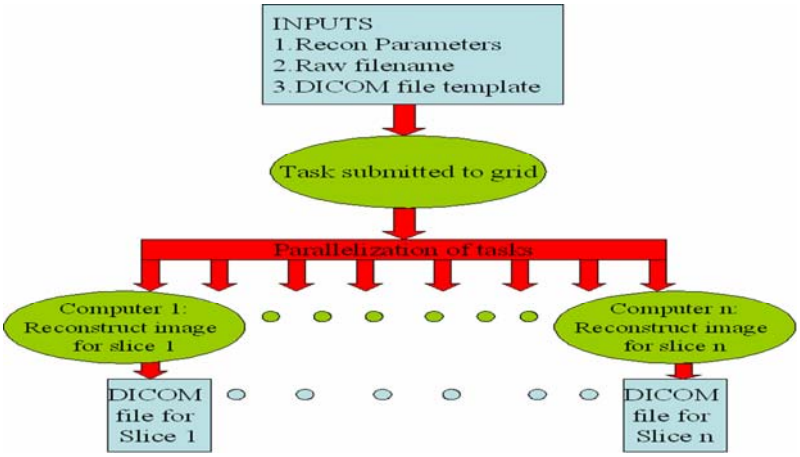

Figure A.1 shows a schematic flow diagram of the GRAPPA based reconstruction of an image volume on a computational cluster

References

1. Foundation NO. Fast facts on Osteoporosis.
2. de Vernejoul MC. Dynamics of bone remodelling: biochemical and pathophysiological basis. Eur J Clin Chem Clin Biochem 1996;34(9):729-734.
3. Majumdar S. Magnetic resonance imaging of trabecular bone structure. Top Magn Reson Imaging 2002;13(5):323-334.
4. B. Vasilic GAL, P.K.Saha, F.W.Wehrli. Micro-MRI based image acquisition and processing system for assessing the response to therapeutic intervention. 2006 11-16 Feb,2006; San Diego. The International Society for Optical Engineering.
5. Siffert RS, Luo GM, Cowin SC, Kaufman JJ. Dynamic relationships of trabecular bone density, architecture, and strength in a computational model of osteopenia. Bone 1996;18(2):197-206.
6. Boutroy S, Bouxsein ML, Munoz F, Delmas PD. In vivo assessment of trabecular bone microarchitecture by high-resolution peripheral quantitative computed tomography. J Clin Endocrinol Metab 2005;90(12):6508-6515.
7. Herlidou S, Grebe R, Grados F, Leuyer N, Fardellone P, Meyer ME. Influence of age and osteoporosis on calcaneus trabecular bone structure: a preliminary in vivo MRI study by quantitative texture analysis. Magn Reson Imaging 2004;22(2):237-243.
8. Majumdar S, Genant HK, Grampp S, Newitt DC, Truong VH, Lin JC, Mathur A. Correlation of trabecular bone structure with age, bone mineral density, and osteoporotic status: in vivo studies in the distal radius using high resolution magnetic resonance imaging. J Bone Miner Res 1997;12(1):111-118.
9. Sodickson DK, Hardy CJ, Zhu Y, Giaquinto RO, Gross P, Kenwood G, Niendorf T, Lejay H, McKenzie CA, Ohliger MA, Grant AK, Rofsky NM. Rapid volumetric MRI using parallel imaging with order-of-magnitude accelerations and a 32-element RF coil array: feasibility and implications. Acad Radiol 2005;12(5):626-635.
10. Sodickson DK, McKenzie CA, Ohliger MA, Yeh EN, Price MD. Recent advances in image reconstruction, coil sensitivity calibration, and coil array design for SMASH and generalized parallel MRI. Magma 2002;13(3):158-163.
11. Blumenkrantz G, Majumdar S. Quantitative magnetic resonance imaging of articular cartilage in osteoarthritis. Eur Cell Mater 2007;13:76-86.
12. Banerjee S, Han ET, Krug R, Newitt DC, Majumdar S. Application of refocused steady-state free-precession methods at 1.5 and 3 T to in vivo high-resolution MRI of trabecular bone: simulations and experiments. J Magn Reson Imaging 2005;21(6):818-825.
13. Banerjee S, Choudhury S, Han ET, Brau AC, Morze CV, Vigneron DB, Majumdar S. Autocalibrating parallel imaging of in vivo trabecular bone microarchitecture at 3 Tesla. Magn Reson Med 2006;56(5):1075-1084.
14. Banerjee S, Krug R, Gamio J, Kelley DAC, Xu D, Vigneron DB, Majumdar S. Rapid in vivo musculoskeletal MR with parallel imaging at 7 Tesla Magnetic Resonance in Medicine 2007;in press.
15. Banerjee S, Majumdar S. Methods for robust quantification of trabecular bone parameters from highly accelerated in vivo MR images obtained by GRAPPA

based techniques at 3 Tesla and 7 Tesla. 2007; Berlin, Germany, Europe. International Society for Magnetic Resonance in Medicine.
16. Banerjee S, Ozturk-Isik E, Nelson SJ, Majumdar S. Fast magnetic resonance spectroscopic imaging at 3 Tesla using autocalibrating parallel technique. 2006 Aug,2006; New York, USA. IEEE. p 1866-1869.
17. Lupo JM, Banerjee S, Kelley DAC, Xu D, Vigneron DB, Majumdar S, Nelson SJ. Partially-parallel, susceptibility-weighted MR imaging of brain vasculature at 7 Tesla using sensitivity encoding and an autocalibrating parallel technique. 2006 Aug,2006; New York,USA. IEEE. p 747-750.
18. Nishimura DG. Principles of Magnetic Resonance Imaging. Stanford; 1996.
19. Salibi N, Brown MA. Clinical MR Spectroscopy. New York: John Wiley & Sons; 1998.
20. Zhou XJ. Echo Planar Imaging. Handbook of MRI Pulse Sequences. San Diego: Elsevier Academic Press; 2004. p 702-740.
21. King KF. Spiral. Handbook of MRI Pulse Seuences. San Diego: Elsevier Academic Press; 2004. p 928-954.
22. Haacke EM, Brown RW, Thompson MR, Venkatesan R. Magnetic Resonance Imaging Physical principles and Sequence Design: John Wiley & Sons; 1999.
23. Yablonskiy DA, Haacke EM. Theory of NMR signal behavior in magnetically inhomogeneous tissues: the static dephasing regime. Magn Reson Med 1994;32(6):749-763.
24. Hipp JA, Jansujwicz A, Simmons CA, Snyder BD. Trabecular bone morphology from micro-magnetic resonance imaging. J Bone Miner Res 1996;11(2):286-297.
25. Majumdar S, Kothari M, Augat P, Newitt DC, Link TM, Lin JC, Lang T, Lu Y, Genant HK. High-resolution magnetic resonance imaging: three-dimensional trabecular bone architecture and biomechanical properties. Bone 1998;22(5):445-454.
26. Parfitt AM, Mathews CH, Villanueva AR, Kleerekoper M, Frame B, Rao DS. Relationships between surface, volume, and thickness of iliac trabecular bone in aging and in osteoporosis. Implications for the microanatomic and cellular mechanisms of bone loss. J Clin Invest 1983;72(4):1396-1409.
27. Parfitt AM. Assessment of trabecular bone status. Henry Ford Hosp Med J 1983;31(4):196-198.
28. Majumdar S, Lin J, Link T, Millard J, Augat P, Ouyang X, Newitt D, Gould R, Kothari M, Genant H. Fractal analysis of radiographs: assessment of trabecular bone structure and prediction of elastic modulus and strength. Med Phys 1999;26(7):1330-1340.
29. Gomberg BR, Saha PK, Song HK, Hwang SN, Wehrli FW. Topological analysis of trabecular bone MR images. IEEE Trans Med Imaging 2000;19(3):166-174.
30. Newitt DC, van Rietbergen B, Majumdar S. Processing and analysis of in vivo high-resolution MR images of trabecular bone for longitudinal studies: reproducibility of structural measures and micro-finite element analysis derived mechanical properties. Osteoporos Int 2002;13(4):278-287.
31. Majumdar S, Newitt D, Jergas M, Gies A, Chiu E, Osman D, Keltner J, Keyak J, Genant H. Evaluation of technical factors affecting the quantification of

trabecular bone structure using magnetic resonance imaging. Bone 1995;17(4):417-430.
32. Majumdar S, Genant HK. Assessment of trabecular structure using high resolution magnetic resonance imaging. Stud Health Technol Inform 1997;40:81-96.
33. Majumdar S, Newitt D, Mathur A, Osman D, Gies A, Chiu E, Lotz J, Kinney J, Genant H. Magnetic resonance imaging of trabecular bone structure in the distal radius: relationship with X-ray tomographic microscopy and biomechanics. Osteoporos Int 1996;6(5):376-385.
34. Issever AS, Vieth V, Lotter A, Meier N, Laib A, Newitt D, Majumdar S, Link TM. Local differences in the trabecular bone structure of the proximal femur depicted with high-spatial-resolution MR imaging and multisection CT. Acad Radiol 2002;9(12):1395-1406.
35. Wald M, Vasilic B, Saha PK, Wehrli FW. Study of Trabecular Bone Microstructure using Spatial Autocorrelation Analysis. In: Amini AA MA, editor; 2005; San Diego. SPIE. p 291-302.
36. Carballido-Gamio J, Phan C, Link TM, Majumdar S. Characterization of trabecular bone structure from high-resolution magnetic resonance images using fuzzy logic. Magn Reson Imaging 2006;24(8):1023-1029.
37. Majumdar S, Link TM, Augat P, Lin JC, Newitt D, Lane NE, Genant HK. Trabecular bone architecture in the distal radius using magnetic resonance imaging in subjects with fractures of the proximal femur. Magnetic Resonance Science Center and Osteoporosis and Arthritis Research Group. Osteoporos Int 1999;10(3):231-239.
38. Chesnut CH, 3rd, Majumdar S, Newitt DC, Shields A, Van Pelt J, Laschansky E, Azria M, Kriegman A, Olson M, Eriksen EF, Mindeholm L. Effects of salmon calcitonin on trabecular microarchitecture as determined by magnetic resonance imaging: results from the QUEST study. J Bone Miner Res 2005;20(9):1548-1561.
39. Link TM, Majumdar S, Augat P, Lin JC, Newitt D, Lu Y, Lane NE, Genant HK. In vivo high resolution MRI of the calcaneus: differences in trabecular structure in osteoporosis patients. J Bone Miner Res 1998;13(7):1175-1182.
40. Majumdar S, Link TM, Millard J, Lin JC, Augat P, Newitt D, Lane N, Genant HK. In vivo assessment of trabecular bone structure using fractal analysis of distal radius radiographs. Med Phys 2000;27(11):2594-2599.
41. Weisskoff RM, Zuo CS, Boxerman JL, Rosen BR. Microscopic susceptibility variation and transverse relaxation: theory and experiment. Magn Reson Med 1994;31(6):601-610.
42. Majumdar S. Quantitative study of the susceptibility difference between trabecular bone and bone marrow: computer simulations. Magn Reson Med 1991;22(1):101-110.
43. Constable RT, Gore JC. The loss of small objects in variable TE imaging: implications for FSE, RARE, and EPI. Magn Reson Med 1992;28(1):9-24.
44. Bogdan AR, Joseph PM. RASEE: a rapid spin-echo pulse sequence. Magn Reson Imaging 1990;8(1):13-19.

45. Jara H, Wehrli FW, Chung H, Ford JC. High-resolution variable flip angle 3D MR imaging of trabecular microstructure in vivo. Magn Reson Med 1993;29(4):528-539.
46. Ma J, Wehrli FW, Song HK. Fast 3D large-angle spin-echo imaging (3D FLASE). Magn Reson Med 1996;35(6):903-910.
47. Zur Y, Stokar S, Bendel P. An analysis of fast imaging sequences with steady-state transverse magnetization refocusing. Magn Reson Med 1988;6(2):175-193.
48. Scheffler K, Hennig J. Is TrueFISP a gradient-echo or a spin-echo sequence? Magn Reson Med 2003;49(2):395-397.
49. Bangerter NK, Hargreaves BA, Vasanawala SS, Pauly JM, Gold GE, Nishimura DG. Analysis of multiple-acquisition SSFP. Magn Reson Med 2004;51(5):1038-1047.
50. Casselman JW, Kuhweide R, Deimling M, Ampe W, Dehaene I, Meeus L. Constructive interference in steady state-3DFT MR imaging of the inner ear and cerebellopontine angle. AJNR Am J Neuroradiol 1993;14(1):47-57.
51. Hargreaves BA, Vasanawala SS, Pauly JM, Nishimura DG. Characterization and reduction of the transient response in steady-state MR imaging. Magn Reson Med 2001;46(1):149-158.
52. O. Dietrich SBR, M.F. Reiser, S.O. Schoenberg. Influence of parallel imaging and other reconstruction techniques on the measurement of signal-to-noise ratios. 2005; Miami. Intl. Soc.Mag.Reson.Med. p 158.
53. Han E, Gold,G, Stainsby,J, Wright,G, Beaulieu,J, Brittain,J. In vivo T1 and T2 Measurements of Muscoskeletal Tissue at 3T and 1.5T. 2003; Toronto,Canada.
54. Hargreaves BA, Gold GE, Beaulieu CF, Vasanawala SS, Nishimura DG, Pauly JM. Comparison of new sequences for high-resolution cartilage imaging. Magn Reson Med 2003;49(4):700-709.
55. Saraswathy S, Crawford F, Nelson SJ. Semi-automated segmentation of brain tumor lesions in MR Images.; 2006; Seattle, USA. International Society for Magnetic Resonance in Medicine.
56. Link TM, Vieth V, Stehling C, Lotter A, Beer A, Newitt D, Majumdar S. High-resolution MRI vs multislice spiral CT: which technique depicts the trabecular bone structure best? Eur Radiol 2003;13(4):663-671.
57. Henkelman RM. Measurement of signal intensities in the presence of noise in MR images. Med Phys 1985;12(2):232-233.
58. Techawiboonwong A, Song,H, Wehrli,FW, Saha,PK. Relative performance of FLASE,TrueFISP and Gradient Echo in micro-MRI of Trabecular Bone. 2004; Kyoto.
59. Meyer CH, Hu BS, Nishimura DG, Macovski A. Fast spiral coronary artery imaging. Magn Reson Med 1992;28(2):202-213.
60. Pruessmann KP. Encoding and reconstruction in parallel MRI. NMR Biomed 2006;19(3):288-299.
61. Kyriakos WE, Panych LP, Kacher DF, Westin CF, Bao SM, Mulkern RV, Jolesz FA. Sensitivity profiles from an array of coils for encoding and reconstruction in parallel (SPACE RIP). Magn Reson Med 2000;44(2):301-308.
62. Samsonov AA, Block WF, Arunachalam A, Field AS. Advances in locally constrained k-space-based parallel MRI. Magn Reson Med 2005.

63. Roemer PB, Edelstein WA, Hayes CE, Souza SP, Mueller OM. The NMR phased array. Magn Reson Med 1990;16(2):192-225.
64. Pruessmann KP, Weiger M, Scheidegger MB, Boesiger P. SENSE: sensitivity encoding for fast MRI. Magn Reson Med 1999;42(5):952-962.
65. Sodickson DK, Manning WJ. Simultaneous acquisition of spatial harmonics (SMASH): fast imaging with radiofrequency coil arrays. Magn Reson Med 1997;38(4):591-603.
66. Sodickson DK, McKenzie CA. A generalized approach to parallel magnetic resonance imaging. Med Phys 2001;28(8):1629-1643.
67. Griswold MA, Kannengiesser S, Heidemann RM, Wang J, Jakob PM. Field-of-view limitations in parallel imaging. Magn Reson Med 2004;52(5):1118-1126.
68. Bydder M, Larkman DJ, Hajnal JV. Generalized SMASH imaging. Magn Reson Med 2002;47(1):160-170.
69. Wang J KT, Nittika M, Jellus V,Kuehn B, Kiefer B. Parallel acquisition techniques with modified SENSE reconstruction (mSENSE). 2001; Wurzburg. p 92.
70. Wald LL, Carvajal L, Moyher SE, Nelson SJ, Grant PE, Barkovich AJ, Vigneron DB. Phased array detectors and an automated intensity-correction algorithm for high-resolution MR imaging of the human brain. Magn Reson Med 1995;34(3):433-439.
71. Griswold MA, Breuer F, Blaimer M, Kannengiesser S, Heidemann RM, Mueller M, Nittka M, Jellus V, Kiefer B, Jakob PM. Autocalibrated coil sensitivity estimation for parallel imaging. NMR Biomed 2006;19(3):316-324.
72. Jakob PM, Griswold MA, Edelman RR, Sodickson DK. AUTO-SMASH: a self-calibrating technique for SMASH imaging. SiMultaneous Acquisition of Spatial Harmonics. Magma 1998;7(1):42-54.
73. Heidemann RM, Griswold MA, Haase A, Jakob PM. VD-AUTO-SMASH imaging. Magn Reson Med 2001;45(6):1066-1074.
74. Griswold MA, Jakob PM, Heidemann RM, Jellus VN, M., Wang J, Kiefer B, Haase A. Generalized autocalibrating partially parallel acquisitions (GRAPPA). Magn Reson Med 2002;47(6):1202-1210.
75. Sodickson DK, Griswold MA, Jakob PM, Edelman RR, Manning WJ. Signal-to-noise ratio and signal-to-noise efficiency in SMASH imaging. Magn Reson Med 1999;41(5):1009-1022.
76. Griswold MA. Advanced K-space Techniques. 2004; Zurich.
77. Weiger M, Pruessmann KP, Boesiger P. Cardiac real-time imaging using SENSE. SENSitivity Encoding scheme. Magn Reson Med 2000;43(2):177-184.
78. Weiger M, Pruessmann KP, Leussler C, Roschmann P, Boesiger P. Specific coil design for SENSE: a six-element cardiac array. Magn Reson Med 2001;45(3):495-504.
79. Tsao J, Boesiger P, Pruessmann KP. k-t BLAST and k-t SENSE: dynamic MRI with high frame rate exploiting spatiotemporal correlations. Magn Reson Med 2003;50(5):1031-1042.
80. Wintersperger BJ, Nikolaou K, Dietrich O, Rieber J, Nittka M, Reiser MF, Schoenberg SO. Single breath-hold real-time cine MR imaging: improved

temporal resolution using generalized autocalibrating partially parallel acquisition (GRAPPA) algorithm. Eur Radiol 2003;13(8):1931-1936.
81. Bammer R, Auer M, Keeling SL, Augustin M, Stables LA, Prokesch RW, Stollberger R, Moseley ME, Fazekas F. Diffusion tensor imaging using single-shot SENSE-EPI. Magn Reson Med 2002;48(1):128-136.
82. Kholmovski EG, Samsonov AA. GARSE: Generalized Autocalibrating Reconstruction for Sensitivity Encoded MRI. 2005. Intl. Soc.Mag.Reson.Med. p 2672.
83. Skare S, Bammer R. Spatial modeling of the GRAPPA weights. 2005; Miami. Intl. Soc.Mag.Reson.Med
p2422.
84. Park J, Zhang Q, Jellus V, Simonetti O, Li D. Artifact and noise suppression in GRAPPA imaging using improved k-space coil calibration and variable density sampling. Magn Reson Med 2005;53(1):186-193.
85. Wang Z, Wang J, Detre JA. Improved data reconstruction method for GRAPPA. Magn Reson Med 2005;54(3):738-742.
86. Morze C, Banerjee, S., Tropp, J., Karponidis, K. , Carvajal, L., Vigneron, DB., Majumdar, S. A Non-Overlapping Phased Array Coil for Parallel Imaging of the Hip at 3.0 T. 2006 6-12 May; Seattle. Intl.Soc.Mag.Reson.Med.
87. F.A.Breuer MB, M.F. Muller, R.M.Heidemann, M.A.Griswold, P.A.Jakob. The use of principal component analysis (PCA) for estimation of the maximum reduction factor in 2D parallel imaging. 2005; Miami. Intl.Soc.Mag.Reson.Med. p 2668.
88. Galatsanos NP, Wernick MN. Multichannel Image Recovery. In: Bovik A, editor. Handbook of Image and Video Processing. San Diego: Academic Press; 1999. p 161-174.
89. Hayes MH. Discrete-Time Random Processes. Statistical Digital Signal Processing and Modeling: John Wiley and Sons, Inc.; 1996. p 81-85.
90. Hayes MH. Spectrum Estimation. Statistical Digital Signal Processing and Modeling: John Wiley and Sons, Inc.; 1996. p 393-426.
91. J. Carballido Gamio CP, S. Majumdar. Fuzzy Logic applied to MRI trabecular bone analysis. 2005; Miami. Intl. Soc. Mag. Reson. Med. p 1988.
92. Weiger M, Boesiger P, Hilfiker PR, Weishaupt D, Pruessmann KP. Sensitivity encoding as a means of enhancing the SNR efficiency in steady-state MRI. Magn Reson Med 2005;53(1):177-185.
93. Link TM, Bauer J, Kollstedt A, Stumpf I, Hudelmaier M, Settles M, Majumdar S, Lochmuller EM, Eckstein F. Trabecular Bone Structure of the Distal Radius, the Calcaneus, and the Spine: Which Site Predicts Fracture Status of the Spine Best? Invest Radiol 2004;39(8):487-497.
94. Griswold MA, Jakob PM, Chen Q, Goldfarb JW, Manning WJ, Edelman RR, Sodickson DK. Resolution enhancement in single-shot imaging using simultaneous acquisition of spatial harmonics (SMASH). Magn Reson Med 1999;41(6):1236-1245.
95. Krug R, Banerjee S, Han ET, Newitt DC, Link TM, Majumdar S. Feasibility of in vivo structural analysis of high-resolution magnetic resonance images of the proximal femur. Osteoporos Int 2005;16(11):1307-1314.

96. Link TM, Sell CA, Masi JN, Phan C, Newitt D, Lu Y, Steinbach L, Majumdar S. 3.0 vs 1.5 T MRI in the detection of focal cartilage pathology--ROC analysis in an experimental model. Osteoarthritis Cartilage 2006;14(1):63-70.
97. Sell CA, Masi JN, Burghardt A, Newitt D, Link TM, Majumdar S. Quantification of trabecular bone structure using magnetic resonance imaging at 3 Tesla--calibration studies using microcomputed tomography as a standard of reference. Calcif Tissue Int 2005;76(5):355-364.
98. Pakin SK, Cavalcanti C, La Rocca R, Schweitzer ME, Regatte RR. Ultra-high-field MRI of knee joint at 7.0T: preliminary experience. Acad Radiol 2006;13(9):1135-1142.
99. Banerjee S, Krug R, Xu D, Carvajal L, Kelley DAC, Vigneron DB, Link TM, Majumdar S. In vivo high resolution imaging of the knee at 7T-potential for MRI of Osteoarthritis. In: ISMRM, editor; 2007; Berlin, Germany, Europe. Proceedings of the 15th Annual Meeting of ISMRM.
100. Wiesinger F, Van de Moortele PF, Adriany G, De Zanche N, Ugurbil K, Pruessmann KP. Potential and feasibility of parallel MRI at high field. NMR Biomed 2006;19(3):368-378.
101. Lustig M, Santos J, Pauly JM. A Super-FOV method for rapid SSFP banding artifact reduction. 2005; Miami, USA. Proceedings of the 13th Annual Meeting of ISMRM. p 504.
102. Kelley DAC. Measuring the effect of field strength on noise amplification factor Concepts in Magnetic Resonance Part B: Magnetic Resonance Engineering 2007;31 B(1):51-59.
103. Wiesinger F, Boesiger P, Pruessmann KP. Electrodynamics and ultimate SNR in parallel MR imaging. Magn Reson Med 2004;52(2):376-390.
104. Ohliger MA, Grant AK, Sodickson DK. Ultimate intrinsic signal-to-noise ratio for parallel MRI: electromagnetic field considerations. Magn Reson Med 2003;50(5):1018-1030.
105. Krug R, Carballido-Gamio J, Burghardt AJ, Haase S, Sedat JW, Moss WC, Majumdar S. Wavelet based characterization of vertebral trabecular bone structure from specimens at 3 Tesla compared to MicroCT 2005; Sanghai.
106. Karl WC. Regularization in Image Restoration and Reconstruction. In: Bovik A, editor. Handbook of Image and Video Processing. San Diego: Academic Press; 2000. p 141-160.
107. Heinz WE, Hanke M, Neubauer A. Regularization of Inverse Problems: Kluwer Academic Publishers; 1996.
108. Hansen P. Regularization Tools: A Matlab package for analysis and solution of discrete ill-posed problems. Numerical Algorithms 1994;6(1):1-35.
109. Nyul LG, Udupa JK. On standardizing the MR image intensity scale. Magn Reson Med 1999;42(6):1072-1081.
110. Nyul LG, Udupa JK, Zhang X. New variants of a method of MRI scale standardization. IEEE Trans Med Imaging 2000;19(2):143-150.
111. Morze CV, Tropp J, Banerjee S, Xu D, Karpodinis K, Carvajal L, Hess CP, Mukherjee P, Majumdar S, Vigneron DB. An eight channel, non-overlapping phased array coil with capacitative decoupling for parallel MRI at 3 T. Concepts

in Magnetic Resonance Part B: Magnetic Resonance Engineering 2007;31B(1):37-43.
112. Grant M, Boyd S, Ye Y. cvx: Matlab Software for Disciplined Convex Programming. 1.1. Stanford: GNU General Public License 2.0; 2007.
113. Nelson SJ. Analysis of volume MRI and MR spectroscopic imaging data for the evaluation of patients with brain tumors. Magn Reson Med 2001;46(2):228-239.
114. Sehgal V, Delproposto Z, Haacke EM, Tong KA, Wycliffe N, Kido DK, Xu Y, Neelavalli J, Haddar D, Reichenbach JR. Clinical applications of neuroimaging with susceptibility-weighted imaging. J Magn Reson Imaging 2005;22(4):439-450.
115. Haacke EM, Xu Y, Cheng YC, Reichenbach JR. Susceptibility weighted imaging (SWI). Magn Reson Med 2004;52(3):612-618.
116. ACS. Cancer Facts and Figures 2007. Volume 2007: American Cancer Society; 2007.
117. Bottomley PA. Spatial localization in NMR spectroscopy in vivo. Ann N Y Acad Sci 1987;508:333-348.
118. Posse S, Tedeschi G, Risinger R, Ogg R, Le Bihan D. High speed 1H spectroscopic imaging in human brain by echo planar spatial-spectral encoding. Magn Reson Med 1995;33(1):34-40.
119. Li X, Vigneron DB, Cha S, Graves EE, Crawford F, Chang SM, Nelson SJ. Relationship of MR-derived lactate, mobile lipids, and relative blood volume for gliomas in vivo. AJNR Am J Neuroradiol 2005;26(4):760-769.
120. Dydak U, Weiger M, Pruessmann KP, Meier D, Boesiger P. Sensitivity-encoded spectroscopic imaging. Magn Reson Med 2001;46(4):713-722.
121. Haase A, Frahm J, Hanicke W, Matthaei D. 1H NMR chemical shift selective (CHESS) imaging. Phys Med Biol 1985;30(4):341-344.
122. Tran TK, Vigneron DB, Sailasuta N, Tropp J, Le Roux P, Kurhanewicz J, Nelson S, Hurd R. Very selective suppression pulses for clinical MRSI studies of brain and prostate cancer. Magn Reson Med 2000;43(1):23-33.
123. Griswold MA, Blaimer M, Breuer F, Heidemann RM, Mueller M, Jakob PM. Parallel magnetic resonance imaging using the GRAPPA operator formalism. Magn Reson Med 2005;54(6):1553-1556.
124. Osorio JA, Ozturk-Isik E, Xu D, Cha S, Chang S, Berger MS, Vigneron DB, Nelson SJ. 3D (1)H MRSI of brain tumors at 3.0 tesla using an eight-channel phased-array head coil. J Magn Reson Imaging 2007;26(1):23-30.
125. Lupo JM, Cha S, Chang SM, Nelson SJ. Dynamic susceptibility-weighted perfusion imaging of high-grade gliomas: characterization of spatial heterogeneity. AJNR Am J Neuroradiol 2005;26(6):1446-1454.
126. Sedlacik J, Herrmann KH, Rauscher A, Reichenbach JR. SWI using different k-space undersampling mechanisms. 2005; Miami, USA. International Society for Magnetic Resonance in Medicine.

Publishing Agreement

It is the policy of the University to encourage the distribution of all theses and dissertations. Copies of all UCSF theses and dissertations will be routed to the library via the Graduate Division. The library will make all theses and dissertations accessible to the public and will preserve these to the best of their abilities, in perpetuity.

Please sign the following statement:

I hereby grant permission to the Graduate Division of the University of California, San Francisco to release copies of my thesis or dissertation to the Campus Library to provide access and preservation, in whole or in part, in perpetuity.

Author Signature

09/04/07

Date